Síntesis y procesado de materiales carbonosos para la fabricación de sistemas fotónicos
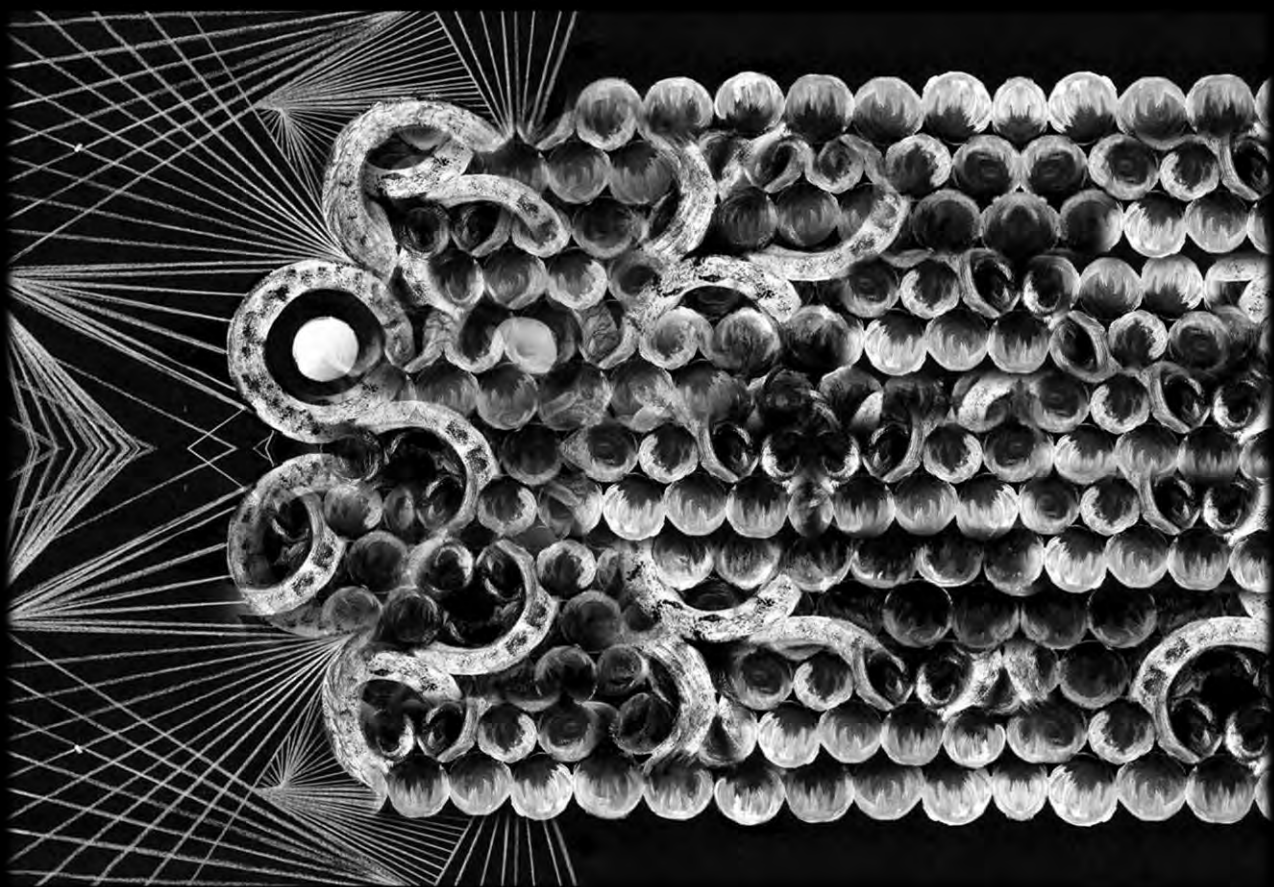
Luz Carime Gil Herrera
Tesis Doctoral

UNIVERSIDAD AUTONÓMA DE MADRID
Facultad de Ciencias

Síntesis y procesado de materiales carbonosos para la fabricación de sistemas fotónicos

Luz Carime Gil Herrera

Memoria presentada para optar al grado de Doctora
en Materiales Avanzados y Nanotecnología

Directores:
Prof. Ceferino López Fernández
Dr. Álvaro Blanco Montes

Tutora:
Prof. Luisa E. Bausa López

Consejo Superior de Investigaciones Científicas
Instituto de Ciencia de Materiales de Madrid

Diciembre 2019

Para Mamá y Papá

Para todas ellas…

*Necesitamos especialmente de la
imaginación en las ciencias.
No todo es matemáticas
y no todo es simple lógica,
también se trata de un poco
de belleza y poesía.*
                María Montessori

*Si no puedo bailar,
no es mi revolución.*
                Emma Goldman

Agradecimientos

Son muchas las personas que han pasado por mi vida durante todos estos años e hicieron posible que esta tesis se escribiera. Algunas, me han dejado grandes enseñanzas, reflexiones, posibilidades de reafirmarme o reformularme, otras me han dado su apoyo, cuidados, tiempo, alegrías, cariño y hasta unos buenos bailes. Infinitas gracias por hacer de esta época algo más llevadero. Espero poder nombrar a todas y que no se me pase ninguna.

Primero quiero agradecer a mis directores Cefe y Álvaro por aceptarme en el grupo, por facilitar todos los recursos para que esta tesis se llevara a cabo. Pero sobre todo por permitirme trabajar y expresarme con total libertad, he crecido mucho en estos años. Álvaro, además gracias por tu optimismo y buen humor. También quiero mencionar a la profesora Beatriz Hernández, que ha sido fundamental durante todo este recorrido, gracias por tus valiosos aportes, consejos y por tu tiempo, los cuales le dieron luz a este trabajo. Eres una de mis referentes como científica. También, a la Profesora Luisa Bausa, mi tutora en la Universidad Autónoma de Madrid.

A las personas que han colaborado con sus aportes científicos en cada uno de los resultados. A los técnicos y técnicas del SEM, los cuales pasamos muchas horas dejándonos los ojos, pero siempre pasando buenos ratos. A Andrés (IMDEA), Ismael (ICMM), Lorena y Raquel (IMN). También al doctor Miguel A. Rodríguez en el ICV, no solo por su ayuda con el SEM sino por tan interesantes discusiones para comprender mi sistema. A las técnicas de análisis térmico, al doctor José

Robertito, me volviste una aficionada a esos mates y abrazos en las mañanas, los llevaré siempre. Cris, por tu dulzura, cuidados y esas palabras, siempre tan apropiadas. Carlos, por colorear todo, por la lente con que ves la vida, por tu risa y alegría. Jon, mi vasco preferido, por tu autenticidad, Gabriel por enseñarme algo de la cultura japonesa y por ser tan buenos compis.

A la demás gente en el ICMM (extensivo al ICMAT) por regalarme momentos tan agradables en tiempos difíciles. Alejandro, David G. y Adolfo, compis de juegos y quedadas. Esther, Sonja, Eider y Jone por dejarme fascinada con vuestro manejo del balón y otros deportes, Lina y Sandra por vuestro apoyo incondicional en tiempos difíciles. Gracias a todas por vuestra sororidad y romper esquemas. A la gente del futbol. A Manu por tu amistad, escucha y disposición, sobre todo para mis ocurrentes preguntas sobre Sevilla y alguna que otra mudanza. A Bernd, compi de arte e interesantes tertulias, por tus consejos y apoyo. Al grupo de materiales porosos y al de magnéticos, por acogerme y hacerme sentir una más.

A la familia OCSI, que me ha dado tanta conciencia política y social, cuidados de familia, habéis hecho cambiar todos mis esquemas de este mundo y de cómo relacionarnos, de una forma más humana. A los buenos momentos con la variopinta Chupipandi, Madridonfire y al espacio Fosforita, que tanto habéis contribuido a descubrirme. A la Morada por tan bonito anticapitalista proyecto, a la gente del swing y del blues, que tanto habéis aportado a mi felicidad. A los de la tierra,

Fredy y Felipe, con vosotros descubrí Madrid en los primeros años y seguís estando.

A todas mis amigas, esa familia escogida, me habéis llenado de plenitud y sororidad. Habéis aportado tantas cosas durante este tiempo, mi admiración a cada una de ellas. Con vosotras hasta el infinito.

Finalmente, a mi madre y a mi padre, a quienes dedico esta tesis. Porque sin vosotras esto no hubiera sido posible. Por creer en mí. Gracias por enseñarme todas mis bases y sobre todo rebeldía en este mundo de conformismos.

Luz Karime

De acuerdo a la decisión de la comisión de doctorado, esta tesis se presenta como un compendio de publicaciones.

Contenido

Introducción

En la naturaleza se pueden encontrar numerosas fuentes de inspiración para desarrollar tecnología. Un ejemplo, es la interacción de la luz con ciertas especies biológicas generando fenómenos ópticos, tales como la difracción, causante de los colores presentes en las alas de ciertas mariposas, plumas de aves, caparazones de invertebrados, en plantas o en minerales. Estos colores, denominados estructurales, tienen la ventaja de no depender de pigmentos que se degradan con el tiempo y por ello despiertan un gran interés en numerosas áreas de la investigación.[1-4] El ejemplo más estudiado es probablemente el ópalo, que pese a estar compuesto de esferas de sílice (ópticamente transparente), despliega un amplio rango de colores causados por la difracción de la luz debido a su estructura periódica asociada a regiones de alta y baja constante dieléctrica dentro del material.[5,6] Estas estructuras se enmarcan dentro de todo un campo de investigación que desde hace más de tres décadas se dedica a estudiar los cristales fotónicos.[7] Así, al

igual que en la naturaleza, los cristales fotónicos son estructuras con una modulación periódica del índice de refracción en una, dos o tres dimensiones del espacio, siendo esta periodicidad del mismo orden que la longitud de onda con la que se desea interactuar. Tal fenómeno, puede dar lugar a la supresión total o parcial de la luz dentro del material, según las características de este, esto se explicará mejor más adelante.

Por tal razón, estas estructuras, son excelentes candidatas para fabricar componentes ópticos capaces de reflejar, confinar o guiar la luz del mismo modo que lo haría un metal, pero sin las pérdidas debidas a la absorción en el espectro visible. Una forma de entender los materiales fotónicos es establecer una analogía con los materiales semiconductores. Los cristales fotónicos representan para la luz o en general para las ondas electromagnéticas, lo que los semiconductores representan para los electrones. Al igual que los semiconductores presentan un rango de energías prohibido para los electrones (*gap*), los cristales fotónicos lo hacen para los fotones. Por otro lado, en el contexto de las telecomunicaciones, la transmisión y procesado de información por medio de impulsos de luz en lugar de impulsos eléctricos son mucho más eficientes debido a que la luz viaja a mayor velocidad y sin resistencia en materiales fotónicos.

Los cristales fotónicos han incursionado en el campo de la investigación desde hace más de tres décadas, resolviendo variadas preguntas en cuanto a la interacción luz-materia se refiere; así mismo,

su fabricación y caracterización ha generado innumerables avances en ciencia de materiales y en el desarrollo de nuevas tecnologías en campos muy diversos, tales como, telecomunicaciones, transporte, energía, medicina, ciencias de la vida, entre otros.[8-12] Sin embargo, la tecnología basada netamente en la fotónica y/o en la integración con la electrónica para fabricar dispositivos que sean capaces de mejorar la eficiencia energética y rapidez de respuesta, sigue siendo uno de los principales objetivos. Por lo tanto, en referencia a la fabricación de materiales fotónicos, sigue siendo primordial que los esfuerzos estén dirigidos hacia el control sobre el tamaño, su ordenamiento y la arquitectura del material.

La forma de producir materiales fotónicos es variada y requiere de varias tecnologías, las cuales pueden ser enmarcadas dentro de estrategias tipo *top-down* o *bottom-up*, cada una de ellas involucran una tecnología característica. En el grupo de investigación donde se desarrolla esta tesis, han apostado por técnicas *bottom-up*. Esto quiere decir que la construcción del material ocurre por el autoensamblado de partículas, de manera que el proceso estará dominado por las leyes que rigen los sistemas coloidales y, por lo tanto, la naturaleza de los bloques de construcción será crucial.

Contextualización de la tesis

La aportación de esta tesis bajo el paraguas de la fabricación de cristales fotónicos, tiene la intención de proporcionar nuevos avances

y mejoras en los materiales existentes, pero además pretende dar luces en otros campos de investigación en donde las arquitecturas generadas puedan ser puntos de partida o de inspiración. Por ejemplo, la síntesis de esferas carbonosas monodispersas y con porosidad jerarquizada, es clave en diversas áreas, tales como baterías, materiales adsorbentes o liberación controlada de fármacos, entre otras, siendo el control sobre el tamaño y la porosidad esencial. Por otro lado, la fabricación de materiales híbridos involucra el uso de múltiples técnicas de procesado dando lugar a un sinfín de combinaciones en cuanto a condiciones experimentales se refiere. Así, numerosas combinaciones como estructuras posibles producen todo un ramillete de arquitecturas porosas de silicio, las cuales son interesantes en aplicaciones tales como baterías, fotocatálisis o celdas solares. Por último, un material fotónico que se fabrique a partir de materiales más sostenibles evitando el uso de procesos agresivos con el medio ambiente genera beneficios no solo para el avance de la ciencia, sino que también para el avance de la sociedad y del planeta.

Estructura de la tesis

Esta tesis, presentada como un compendio de publicaciones, está organizada en cuatro partes. La primera parte consiste en una breve introducción a algunos conceptos, los cuales son claves para el entendimiento de este trabajo; seguido por una segunda parte que plantea los objetivos perseguidos. La tercera parte comprende un resumen de

los resultados obtenidos agrupados en tres publicaciones, que también son anexadas en su formato original. Finalmente, la cuarta parte comprende las conclusiones y perspectivas de este trabajo.

Los estudios presentados en los resultados están dirigidos, específicamente, a la fabricación de un cristal fotónico de silicio tomando como punto de partida una plantilla fabricada con materiales carbonosos. Cada etapa de la fabricación está resumida en una publicación. Tanto los tres artículos publicados, como mi aportación en cada uno de ellos, se describen de forma resumida a continuación:

- <u>Publicación 1.</u>

  Seeded Synthesis of Monodisperse Core-Shell and Hollow Carbon Spheres.
  <u>Gil-Herrera, L. K.</u>, Blanco, Á., Juárez, B. H., & López, C.
  Small, (2016), *12*(32), 4357–4362.

  Síntesis de esferas hibridas carbonosas coloidales y de esferas huecas con polidispersidades por debajo del 5%. Estudio sistemático de los factores que afectan la síntesis de esferas carbonosas a partir de la nucleación y crecimiento heterogéneo vía tratamiento hidrotermal.

- <u>Publicación 2.</u>

  Hierarchically Porous Carbon Photonic Structures.

Gil-Herrera, L. K., Pariente, J. A., Gallego-Gómez, F., Gándara, F., Juárez, B. H., Blanco, Á., & López, C.
Advanced Functional Materials, (2018), *28*(27), 1703885.

Ordenamiento tridimensional de las esferas previamente obtenidas para la fabricación de un ópalo de carbono con porosidad jerárquica. Estudio de la respuesta óptica como función de la naturaleza *core-shell* y *hollow-shell* de las esferas y de su porosidad.

- **Publicación 3.**

Silicon-Based Photonic Architectures from Hierarchically Porous Carbon Opals.
Gil-Herrera, L. K., Gallego-Gómez, F., Torres-Pardo, A., González-Calbet, J. M., Palomares, F. J., Blanco, A., Juárez, B. H., López, C.
Particle & Particle Systems Characterization, (2019), *1900396*, 1900396.

Fabricación de diversas arquitecturas fotónicas basadas en silicio sobre estructuras ordenadas de esferas de carbono. Estudio de la influencia de las condiciones de procesado (infiltración-calcinación-ataque) así como también, la apropiada combinación de estas.

1. Algunos Conceptos

1.1 Cristales fotónicos (CFs)

En 1987, Eli Yablonovitch[7] y Sajeev John[13] introdujeron el concepto de cristales fotónicos en dos investigaciones simultaneas e independientes. Los dos trabajos plantearon un material capaz de inhibir la emisión espontanea de una fuente de luz en su interior [7] y de localizarla.[13]

Los CFs, son materiales que presentan una modulación periódica de la constante dieléctrica (o índice de refracción) a lo largo de una, dos o las tres direcciones del espacio (Figura 1). La unidad básica que se repite en el espacio está constituida por componentes organizados de manera análoga a como lo hacen los átomos en un sólido cristalino. Asimismo, la interacción de la luz con estos sistemas presenta numerosas semejanzas a la propagación de electrones en un cristal de estado
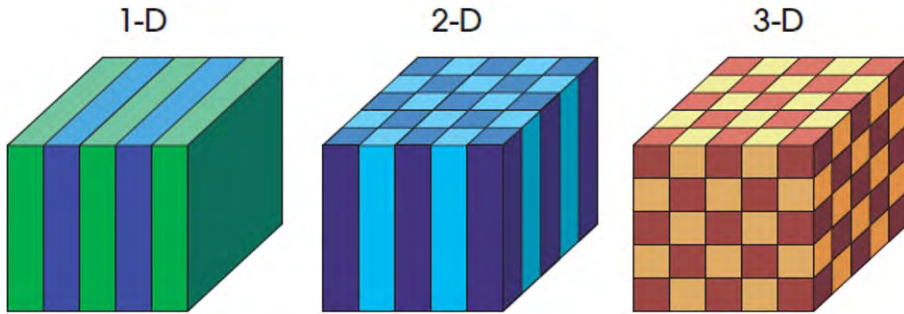
Figura 1. Clasificación de cristales fotónicos, dependiendo de la periodicidad en la constante dieléctrica en una, dos y tres dimensiones. Los diferentes colores representan materiales con diferentes constantes dieléctricas. Tomado de la referencia [6].

sólido. De este modo, muchos de los conceptos desarrollados en estado sólido pueden extenderse a este campo.

La periodicidad en el índice de refracción provoca que la interferencia de las distintas ondas difractadas por los planos cristalinos sea constructiva o destructiva en algunas direcciones y para algunas energías, dando lugar a la existencia de bandas permitidas y prohibidas para la propagación de los fotones. Al igual que en estado sólido, de la estructura de bandas (es decir, la relación entre los estados energéticos permitidos en el cristal y el vector de ondas de la red reciproca del cristal) se puede derivar la propagación de la radiación en estas estructuras periódicas. Por lo tanto, un CF con una banda prohibida (*gap* fotónico) reflejará la luz por completo, consecuencia de la anulación completa de densidad de estados para el rango de frecuencias correspondientes.

Los *gaps* pueden o no depender de la dirección de propagación de la onda en el cristal fotónico. *Gaps* que se generan solamente en determinadas direcciones se definen como *pseudogaps* o *gaps* direccionales. Por el contrario, una región de energía prohibida independiente de la dirección de propagación de la luz, será un gap fotónico completo (Figura 2). Las bandas fotónicas representan los estados permitidos para los fotones dentro del cristal dependiendo de su energía (ω) y la dirección cristalina (**k**). Así, estas funciones ω(**k**) se obtienen de la relación entre la frecuencia de los fotones propagantes ω que, debido a la escalabilidad del sistema, puede ser expresada en unidades reducidas a/λ, (donde a es el parámetro de red, y λ la longitud de onda de la radiación) y el vector de onda **k**, expresado en función de las direcciones de alta simetría de la celda unidad en el espacio recíproco. La figura 2 muestra una estructura de bandas con un *pseudogap* (izquierda) y con un *gap* completo (derecha). El *pseudogap* se forma, por ejemplo, en estructuras de esferas de sílice (*n* = 1.45) en aire ordenadas en una configuración fcc, mientras que la for-
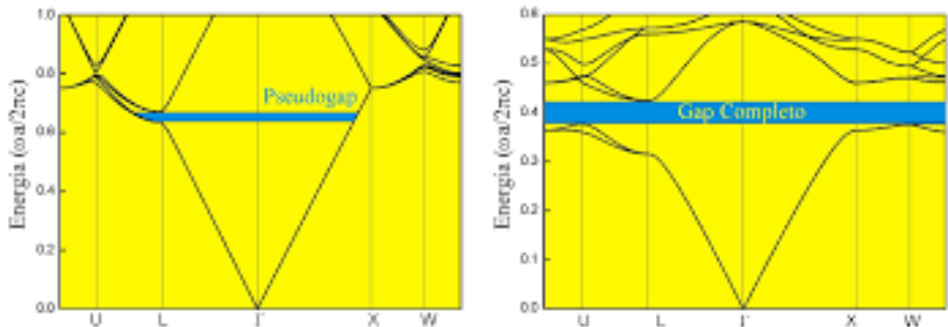
Figura 2. Estructura de bandas fotónicas con un *pseudogap* (izquierda) y con un *gap* completo (derecho). Tomado de la referencia [14].

mación del gap completo se obtiene, por ejemplo, a partir de esferas de aire ($n = 1$) en silicio ($n = 3.5$) formando una estructura diamante.[15]

Existen varios parámetros que definen las propiedades fotónicas e influyen en la existencia de pseudogaps o de un gap completo:

- *Simetría o estructura cristalina:* disposición geométrica que presentan las unidades que lo componen (centros dispersores) formando la red de Bravais. La simetría podrá ser, según al grupo espacial al que pertenezca el cristal, de tipo hexagonal (hcp), cúbica centrada en las caras (fcc), tetragonal (tg), etc.

- *Topología:* forma en que se organizan los centros dispersores atendiendo a su conectividad. Determina la interconexión entre los centros dispersores (zonas de alto índice de refracción) y así, la modulación periódica. Si estos se encuentran interconectados, formando una red, será una tipología tipo "*network*". Si, por el contrario, se encuentran embebidos en un material de bajo índice de refracción y aislados entre sí, serán de tipo "*cermet*".

- *Contraste de índices:* es la razón entre los índices de refracción de los dos medios existentes. Cuanto mayor sea el contraste, más eficiente será la difracción de la luz. Según el tipo de estructura, puede existir un valor mínimo en el cual se abra un *gap*.

- *Factor de llenado:* es la relación entre el volumen del material de alto índice y el volumen total.

- *Parámetro o constante de red:* determinará el rango de longitudes de onda donde la estructura desarrollará un *gap* y da cuenta de la escalabilidad de estos sistemas.

Diferentes combinaciones de estos parámetros dan lugar a una multitud de estructuras con diferentes propiedades fotónicas. Esto da una idea de la potencialidad de estos materiales tanto en su fabricación como en sus aplicaciones.

1.2 Ópalos artificiales

Los ópalos artificiales o cristales fotónicos son estructuras 3D que resultan del ordenamiento espontaneo de esferas coloidales monodispersas en un arreglo cúbico centrado en las caras (fcc).[16] Por otro lado, un coloide es una suspensión en la que, la fase dispersa es tan pequeña (1-1000 nm) que la acción de la fuerza de gravedad es menor o comparable a las fuerzas hidrodinámicas y las interacciones dominantes son fuerzas de corto alcance como las fuerzas atractivas (van der Waals) y las fuerzas debido a las cargas superficiales (electroestáticas). Los ópalos artificiales son fabricados ya sea con esferas inorgánicas, por ejemplo, sílice (SiO_2); o con esferas poliméricas como poliestireno (PS) o polimetilmetacrilato (PMMA).

Las propiedades fotónicas de los ópalos artificiales han sido estudiadas con detalle. [17-19] Un ópalo formado por esferas de SiO_2 (o de polímero) y aire no tiene la topología, no importa el contraste de índi-

ces, para la apertura de un gap completo.[20] Sin embargo, un ópalo puede ser usado como molde para la infiltración de sus intersticios por un material con alto índice de refracción ($n \geq 2.9$). Posteriormente, con la eliminación del molde, se obtiene la estructura inversa del ópalo —esferas de aire en un arreglo fcc embebidas en una matriz— y si el contraste de índices es el adecuado, dará lugar a la apertura de un gap fotónico completo entre las bandas octava y novena.[21-23] El primer ópalo inverso con un gap completo fue conseguido a partir de un ópalo de esferas de aire embebidas en una matriz de Si.[23]

1.3 Fabricación de cristales coloidales autoensamblados

El procedimiento para la fabricación de cristales coloidales por el método de autoensamblado consiste, principalmente en: i) síntesis de esferas; ii) ordenamiento (fabricación del ópalo); iii) infiltración con un material de mayor índice; iv) inversión del ópalo.

Esferas coloidales monodispersas

Para la síntesis de esferas coloidales monodispersas, puede utilizarse una amplia gama de materiales orgánicos e inorgánicos como metales, dieléctricos o materiales híbridos de diferentes configuraciones.[24-26] Las esferas poliméricas son relativamente fáciles de preparar (en un solo paso) con un amplio rango de tamaños y tienden a ordenarse mejor al tener una menor densidad, construyendo ópalos que

pueden considerarse infinitos a la hora de comparar con las predicciones teóricas (>35 capas). Sin embargo, poseen una baja estabilidad térmica, necesaria para diferentes procesamientos involucrados en la fabricación de estructuras fotónicas. Por el contrario, las esferas inorgánicas, que presentan gran estabilidad química y térmica, requieren largos tiempos de preparación y estrategias más elaboradas. Su reología, fuertemente influenciada por el tamaño, dificulta el ordenamiento y, por ende, da lugar a cristales con muchos defectos.[19]

Por otro lado, esferas híbridas, compuestas de diferentes materiales y morfologías, brindan todo un abanico de funcionalidades y versatilidades en su fabricación, por lo que son, a día de hoy, más invocadas en la fabricación de nuevos materiales. Entre este tipo de estructuras se encuentran morfologías del tipo núcleo-corteza (*core-shell, hollow@shell, yolk@shell*), entre otras.

En este trabajo se han sintetizado esferas híbridas del tipo *core-shell* y *hollow@shell* compuestas de un núcleo de poliestireno (PS) y una corteza carbonosa (C), para formar esferas PS@C. La elección de materiales carbonosos se debe, principalmente, a sus propiedades fisicoquímicas, su fácil acceso y bajo coste. Además de poseer una gran estabilidad térmica y química, las esferas carbonosas coloidales pueden ser sintetizadas con relativa facilidad.

Síntesis de esferas: reacción de carbonización hidrotermal (HTC)

El HTC (de sus siglas en inglés, *HydroThermal Carbonization*) es un proceso de carbonización artificial que ocurre en un medio acuoso a temperaturas entre 160 y 220 °C y a presiones de saturación entre (20-60 bar). Estos sistemas permiten procesar una amplia gama de tipos de biomasa y/o polisacáridos transformándolos en productos con mayor contenido de carbono. Las esferas carbonosas obtenidas son bastante versátiles en cuanto a las posibilidades estructurales y funcionales, lo que despierta un gran interés en diferentes campos tales como almacenamiento de energía, electrodos, catálisis, sensores, o en tecnologías cromatografías, farmacéutica, entre otros.

Algunas de las ventajas de esta técnica son:

- Temperaturas de carbonización bajas (160 - 220 °C), en comparación con otros métodos de carbonización tradicional como la pirólisis.
- La reacción tiene lugar en medio acuoso, bajo presiones autogeneradas por el sistema, lo que evita costes por secado de los precursores. El hecho de que sea en un medio acuoso permite compatibilizarlo con innumerables estrategias que usan plantillas, siendo una ventaja frente a la pirólisis.
- Se obtienen generalmente partículas esféricas de tamaño micro y submicrométrico.

- El desarrollo y control de la porosidad es posible mediante técnicas de moldeo en la nanoescala (*nanocasting*), plantillas o procedimientos de activación química o térmica.[27,28]

- Pueden dar lugar a materiales multifuncionales híbridos combinándolos, por ejemplo, con nanopartículas inorgánicas, metales, monómeros poliméricos, entre otros.[29,30]

- La superficie es de carácter polar y contiene grupos oxigenados C(O), siendo importantes en estrategias de post-funcionalización.[31,32]

- Tanto la química superficial como las propiedades electrónicas pueden ser modificadas mediante tratamiento térmico, a la vez que son conservadas su morfología y porosidad.[33,34]

Mecanismos de formación

Dependiendo de la fuente carbonosa (monosacáridos, polisacáridos o biomasa), son muchas las reacciones que tienen lugar en las condiciones HTC lo que da lugar a una compleja mezcla de compuestos que hace difícil su estudio.[35-37] Una de las más estudiadas por su simplicidad, es la reacción de glucosa vía HTC, la cual produce un residuo insoluble (esferas carbonosas), compuestos orgánicos solubles y productos gaseosos. Los productos gaseosos contienen principalmente CO_2 (70-90%) y otros gases como CO y H_2.[38] El mecanismo por el cual ocurre la formación de esferas carbonosas a partir de la glucosa se puede resumir en dos etapas, esquematizadas en la figura 3. La primera es
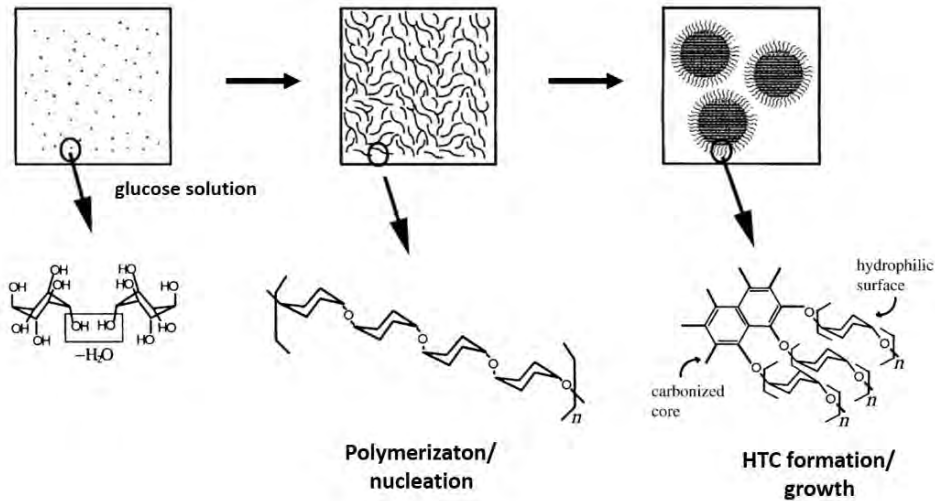
Figura 3. Esquema del modelo de crecimiento de las CSs. Primera etapa: deshidratación de la glucosa, segunda etapa: policondensación/aromatización de pequeñas unidades y tercera etapa: crecimiento en la superficie hidrofílica de las esferas. Adaptado de la referencia [39].

la deshidratación de la glucosa que da lugar a la fragmentación del anillo generando diferentes especies solubles, todos ellos derivados del hidroximetilfurfural (HMF) y desencadenando una variedad de compuestos orgánicos. La segunda etapa ocurre con el entrelazamiento de derivados de HMF y reacciones de policondensación intermoleculares o de polimerización, dando lugar a *clusters* aromáticos y complejos oxigenados, es decir, a la formación de enlaces tipo C-C y C=O, respectivamente. Al aumentar la concentración de *clusters* aromáticos, el sistema alcanza el punto crítico de sobresaturación, dando lugar a la nucleación. La superficie de los núcleos se encuentra hidrofilizada con grupos C(O) reactivos (hidroxilo, carbonilo, carboxílico, etc.) lo que

permite que el crecimiento ocurra de adentro hacia afuera, por la unión de estos grupos con las partículas presentes en el medio de reacción.

De otro lado, las CSs producidas por HTC, resultado del crecimiento de una corteza carbonosa sobre el núcleo de PS, dan lugar a esferas hibridas del tipo *core-shell*, PS@C, donde tal capa carbonosa es altamente amorfas e hidrofílica.

Esferas huecas: hollow@C

La pirólisis de las esferas PS@C en atmosfera inerte y a temperaturas mayores de 350 °C (temperatura de descomposición del PS), ocasiona la eliminación del núcleo y produce esferas carbonosas huecas.

En los últimos años, se ha incrementado el interés por las esferas hollow@C, traduciéndose en grandes avances tanto en la síntesis como en sus aplicaciones en muchas ramas de la investigación, algunas de estas son catálisis, almacenamiento y conversión de energía, fotónica y aplicaciones biomédicas.[40,41] Su gran atractivo radica en su gran área superficial, baja densidad, alta capacidad de descarga, control sobre su estructura, estabilidad química y térmica, desarrollo de la porosidad en la corteza y control sobre el tamaño de poros, entre otros. Son muchas las estrategias adoptadas para la fabricación de esferas carbonosas entre las que se encuentran, el uso de plantillas - "*hard*-templating" o "*soft*-templating"- o sin plantilla. Posteriormente, ya sea por un tratamiento

térmico o químico, la plantilla es eliminada dando lugar a una estructura hueca. Si, además, la morfología y la monodispersidad son reproducidas, estamos en el caso de "*hard templating*".

Para el caso de las esferas sintetizadas en este trabajo, las partículas de PS actúan como un "*hard templating*" y así, son usadas como semillas, mientras que la integración de la glucosa se lleva a cabo gracias a la carga superficial del PS comercial vía HTC. Por otro lado, la pirólisis no solo ocasiona la descomposición del PS, sino que también, en función de la temperatura, produce el encogimiento de las CSs entre un 10-15% de su diámetro, y el desarrollo de porosidad en la corteza.

Autoensamblamiento de esferas coloidales

Existen muchas estrategias para ordenar esferas coloidales.[42-46] Una de ellas es el método de deposición vertical (Figura 4) o deposición por convección, que es el más empleado para el crecimiento de ópalos, debido a su preciso control sobre el grosor (número de capas de esferas), uniformidad y alta calidad de los cristales en grandes áreas.[47] La deposición vertical está basada en la evaporación del líquido (generalmente etanol o agua) forzando a las esferas a ordenarse en un estructura fcc cuyos planos [111] están dispuestos paralelamente a la superficie del substrato.[48]
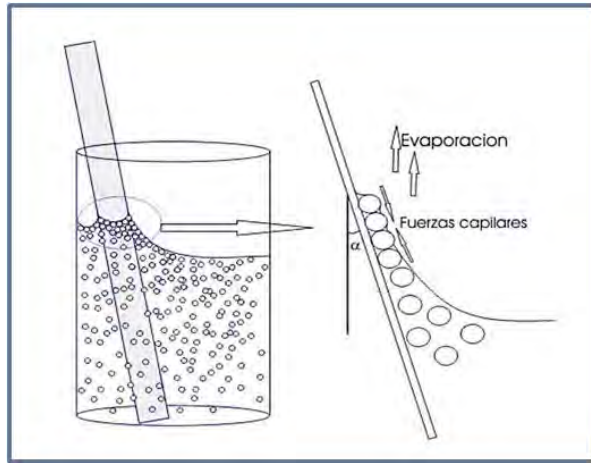
Figura 4. Esquema del método de autoensam-
blado por deposición vertical.

De manera breve, cuando el sustrato es sumergido en la suspen-
sión coloidal, el cristal comienza a crecer en el punto donde el grosor
del menisco del líquido es más pequeño que el tamaño de las esferas.
Asimismo, la formación de un menisco entre esferas y la existencia de
fuerzas capilares da lugar a la atracción de las esferas por el sustrato y
entre sí, lo que produce su ordenamiento en un arreglo compacto.

El crecimiento se desarrolla por el transporte de convección de
las partículas en la interface solido/liquido/vapor incrementando el
espesor hasta alcanzar el equilibrio. Parámetros como la temperatura o
la humedad afectan directamente la velocidad de evaporación lo que
determina el transporte de la solución y consecuentemente mueve las
partículas hacia el menisco. Si la evaporación es muy lenta, una canti-
dad significativa de esferas sedimentarán antes de ensamblarse. Por
ejemplo, partículas muy densas precipitan más rápido y, por tanto, su

ordenamiento será más difícil. Otro importante parámetro que influye en la cristalización es la concentración del coloide. En general, un incremento de concentración produce un incremento en el grosor del ópalo y un empeoramiento de su calidad.

Obtención del ópalo inverso

Para lograr un gap fotónico completo es necesario obtener la estructura inversa del ópalo, es decir, los huecos del ópalo deben estar rellenos con un material que presente un alto de índice de refracción, para luego eliminar el ópalo.

Infiltración

La infiltración puede llevarse a cabo mediante diferentes procesos, tales como deposición química en fase de vapor (CVD), deposición por capa atómica (ALD), reacciones de sol-gel o electroquímicas, entre otras. La infiltración mediante CVD acontece cuando el precursor, en estado gaseoso, viaja por la red porosa del ópalo accediendo a toda la estructura. Posteriormente, ya sea mediante reacciones químicas con otro reactivo o mediante descomposición térmica, se forma una capa del material deseado sobre la superficie de las esferas. Este procedimiento da lugar a recubrimientos muy uniformes y permite un elevado control sobre el espesor de los mismos, ya que, debido a los reactivos en fase gaseosa, estos pueden viajar con gran facilidad a través de los poros.

Por ejemplo, el silicio ($n = 3.5 - 3.9$) no solo permite conseguir estructuras con gran contraste dieléctrico, sino que también es ópticamente transparente en las regiones del infrarrojo (IR) y del IR-cercano, lo que lo hace muy apropiado en aplicaciones de telecomunicaciones. Por lo general, la infiltración de Si se realiza mediante la descomposición térmica del disilano (Si_2H_6) y requiere de temperaturas por arriba de 300 °C, siendo indispensable un ópalo-plantilla que resista tales temperaturas. Típicamente, la infiltración de Si-CVD sobre cristales de esferas coloidales poliméricas requiere del uso de estrategias más complejas, como es el uso de una doble-plantilla de sílice que proteja al polímero volviéndolo más resistente.[49,50] Por lo tanto, es un reto conseguir sistemas coloidales más compatibles con el proceso de infiltración.

Inversión

Por último, una vez infiltrados los ópalos con Si se elimina selectivamente el ópalo carbonoso mediante una calcinación en aire, resultando una estructura porosa de silicio. El material carbonoso es quemado a 500 °C, generando especies gaseosas como CO_x, CH_x, H_2O. La difusión de las especies de descomposición del esqueleto carbonoso viaja por la estructura porosa del Si, por lo tanto, la accesibilidad de poros es fundamental para una eliminación completa. Por tal motivo, en muchos casos, es necesario abrir la estructura, es decir, eliminar la capa superior de silicio, para dar accesibilidad a los gases. Esto se hace,

mediante un ataque de iones reactivos, en donde de forma selectiva se ataca al silicio, dejando al descubierto el ópalo carbonoso.

Ataque por iones reactivos: RIE

El RIE (por sus siglas en inglés, *reactive ion etching*) es un proceso de ataque selectivo. Una descarga producida por un campo electromagnético genera un plasma, que está formado por átomos y/o radicales libres de los gases que se encuentran en la cámara. Las reacciones químicas que ocurren entre los elementos de la muestra atacada y las especies reactivas generadas por el plasma producen especies volátiles que eliminarán total o parcialmente el material reactivo de la muestra. El proceso se lleva a cabo en una cámara de vacío y da lugar a un grabado vertical anisotrópico.

Específicamente, para el ataque de Si se utiliza un plasma de SF_6 o una mezcla de SF_6/O_2. Además, las condiciones de flujo, presión del plasma en la cámara, potencia de la radiofrecuencia y el tiempo de ataque, son fundamentales para sintonizar el nivel de profundidad del grabado. La generación del plasma a partir del SF_6 genera principalmente átomos fluoruros (F^-), los cuales tienen una alta afinidad con el Si y forman compuestos volátiles del tipo SiF_x ($x = 1/4, 2, 4$). Por otro lado, la combinación SF_6/O_2 produce además de átomos F, especies SiO_xF_y que tendrán un efecto pasivante sobre la muestra, modificando el ataque.[51]

2. Objetivos

El principal objetivo de este trabajo es demostrar la viabilidad y utilidad de los materiales carbonosos para la fabricación de estructuras ordenadas híbridas con aplicaciones en fotónica, específicamente en el rango visible e IR cercano. Por lo tanto, ha sido necesario el desarrollo y optimización de cada etapa dentro del marco de la fabricación de cristales fotónicos coloidales:

Síntesis de esferas coloidales carbonosas (CCS) monodispersas: Se usa como estrategia de síntesis la carbonización hidrotermal (HTC) donde la glucosa y el poliestireno son el precursor carbonoso y la semilla de crecimiento, respectivamente, dando lugar a estructuras hibridas, tipo *core-shell*. Puesto que los cristales fotónicos deben ser sintonizados a longitudes de onda determinadas, es preciso sintetizar partículas con el tamaño preciso y con polidispersidades menores al 5% para lograr su ordenamiento. Por consiguiente, es necesario opti-

mizar las condiciones del HTC, tales como temperatura, tiempo, concentración de la glucosa y del PS para la producción de esferas monodispersas con tamaños entre 200 y 1500 nm.

Fabricación de ópalos carbonosos: el ordenamiento en 3D de las CCS se realiza mediante el autoensamblado utilizando el método de deposición vertical. La calidad del arreglo cristalino y por ende las propiedades ópticas, requiere que el ópalo tenga la mínima cantidad de defectos y fracturas en su estructura fcc. Factores tales como la carga superficial, las fuerzas de atracción y repulsión, y de van der Waals entre las CCS, así como también la interacción con el solvente, deben ser tenidos en cuenta. Por lo tanto, se optimiza las condiciones idóneas para el crecimiento de ópalos carbonosos.

Por otro lado, la pirólisis del ópalo carbonoso deja un sistema poroso jerárquico, dependiente de la temperatura. Así, es necesario hallar toda una serie de condiciones (temperatura, tiempo y atmosfera de pirólisis) con el fin de conservar la calidad tanto en el ordenamiento como en la respuesta óptica.

Arquitecturas fotónicas basadas en silicio: la obtención de un *gap* fotónico completo requiere la infiltración de los poros del HCO con silicio, y posteriormente, la eliminación de la plantilla carbonosa mediante calcinación; este último paso involucra un paso intermedio mediante el ataque de iones reactivos (RIE), dejando una estructura de silicio altamente porosa. Así pues, el uso de HCO como plantilla requiere de una compatibilidad no solo a la hora de su procesado, sino

también de su eliminación, buscando el mínimo daño estructural. Para esto es necesario estudiar tanto las condiciones experimentales de deposición del Si vía CVD como las condiciones de eliminación (tratamiento térmico y de ataque RIE). Teniendo en cuenta la naturaleza química del esqueleto carbonoso y/o su porosidad, podemos explorar todo un abanico de posibilidades para la obtención de diversas arquitecturas porosas de Si y de C-Si.

Finalmente, para el seguimiento en todo el proceso, es necesario caracterizar morfológica y ópticamente cada estructura.

3. Resumen de resultados y publicaciones

Publicación 1.
Seeded Synthesis of Monodisperse Core-Shell and Hollow Carbon Spheres.
Small, (**2016**), *12*(32), 4357–4362.

Publicación 2.
Hierarchically Porous Carbon Photonic Structures.
Advanced Functional Materials, (**2018**),
28(27), 1703885.

Publicación 3.
*Silicon-Based Photonic Architectures
from Hierarchically Porous Carbon Opals.*
Particle & Particle Systems Characterization, (**2019**),
1900396, 1900396.

Síntesis de esferas carbonosas

La fabricación de esferas coloidales monodispersas de materiales carbonosos se lleva a cabo mediante la reacción de HTC usando la glucosa y el PS (Figura 5). El crecimiento de las esferas PS@C ocurre mediante una serie de reacciones heterogéneas. No obstante, reacciones homogéneas dan lugar a nucleaciones, lo que genera una indeseada segunda población de esferas.[52,53] En consecuencia, y con el fin de favorecer el proceso de crecimiento más que el de nucleación, se optimizan las condiciones de síntesis, tales como temperatura, tiempo y concentración de la glucosa, para cada semilla.

En este trabajo se obtiene un amplio abanico de tamaños de esferas carbonosas hibridas no agregadas y homogéneas con tamaños entre 500-900 nm. Se encuentra que para cada tamaño de PS (200-600 nm)
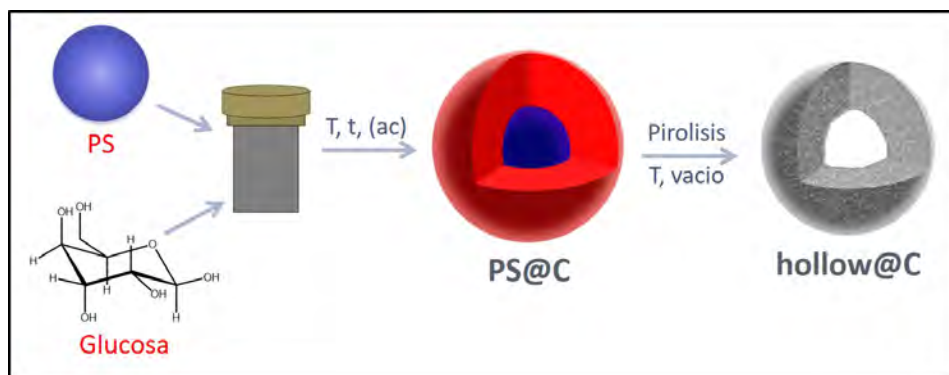
Figura 5. Esquema de la formación de esferas PS@C mediante la reacción de HTC y de esferas hollow@C con porosidad jerárquica después de la pirólisis.

empleado hay una serie de condiciones que favorecen el crecimiento carbonoso. Cuanto más pequeño es el tamaño de semilla mayor será la superficie disponible para el crecimiento y, por tanto, el sistema podrá tolerar un mayor rango de concentraciones de glucosa y de temperatura. El uso de semillas de PS para asistir al proceso queda patente en la figura 6, donde se observa que la formación de CS en ausencia de PS produce esferas no uniformes y aglomeradas, acorde con lo reportado en la literatura.[35,54,55] En este sentido, es importante recalcar que la fabricación de CS con tamaños mayores de 500 nm y monodispersidades <5% sin la adición de surfactantes o aditivos no ha sido reportada antes de este trabajo.

La naturaleza hibrida de las CS permite, mediante una pirólisis, la obtención de estructuras carbonosas huecas, así como también, el desarrollo de microporosidad en la corteza. Cabe destacar que tanto la homogeneidad como la monodispersidad del sistema original son conservadas pese al encogimiento sufrido por las CS (10-15 %) como consecuencia de los procesos de gasificación/carbonización. Por otro lado, el desarrollo de porosidad es función de la temperatura y de la naturaleza química de la estructura carbonosa. Así pues, esferas fabricadas por HTC —amorfas, con carbonos sp^2, sp^3 y grupos superficiales C(O), del tipo -OH y -COOH en su mayoría— sometidas a 500 °C desarrollan un área superficial de hasta 540 m^2/g, y hasta 860 m^2/g a 800 °C. Estos valores, pese a no ser significativos en aplicaciones como almacenamiento de energía o supercapacitores, serán de gran ayuda en

este trabajo a la hora de diseñar arquitecturas basadas en silicio y sistemas tridimensionales con porosidad jerarquizada.

Finalmente, tanto la fabricación de esferas carbonosas como de esferas huecas monodispersas por este método es bastante común en ciencia de materiales, dadas las posibilidades de síntesis. En este caso, las diferentes condiciones de síntesis permiten tener control sobre el tamaño final, la capa carbonosa y el tamaño del hueco, mientras que el uso de semillas favorece el crecimiento homogéneo. De igual forma, el uso de semillas contribuye al control de la dispersión en el tamaño final, lo que es un factor indispensable para la fabricación de cristales fotónicos coloidales.
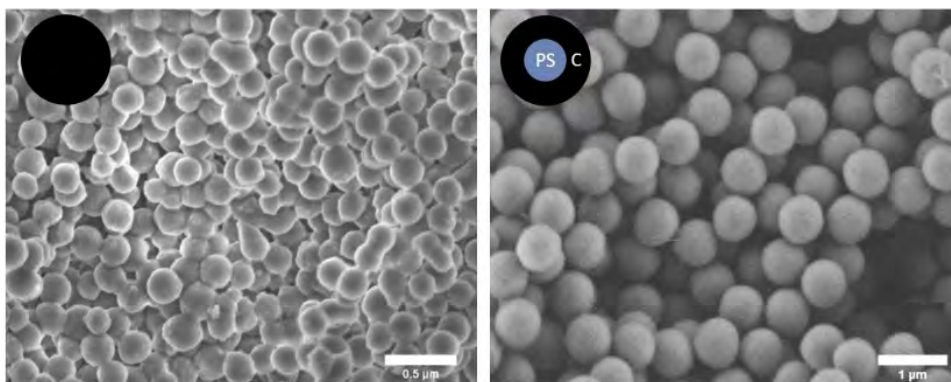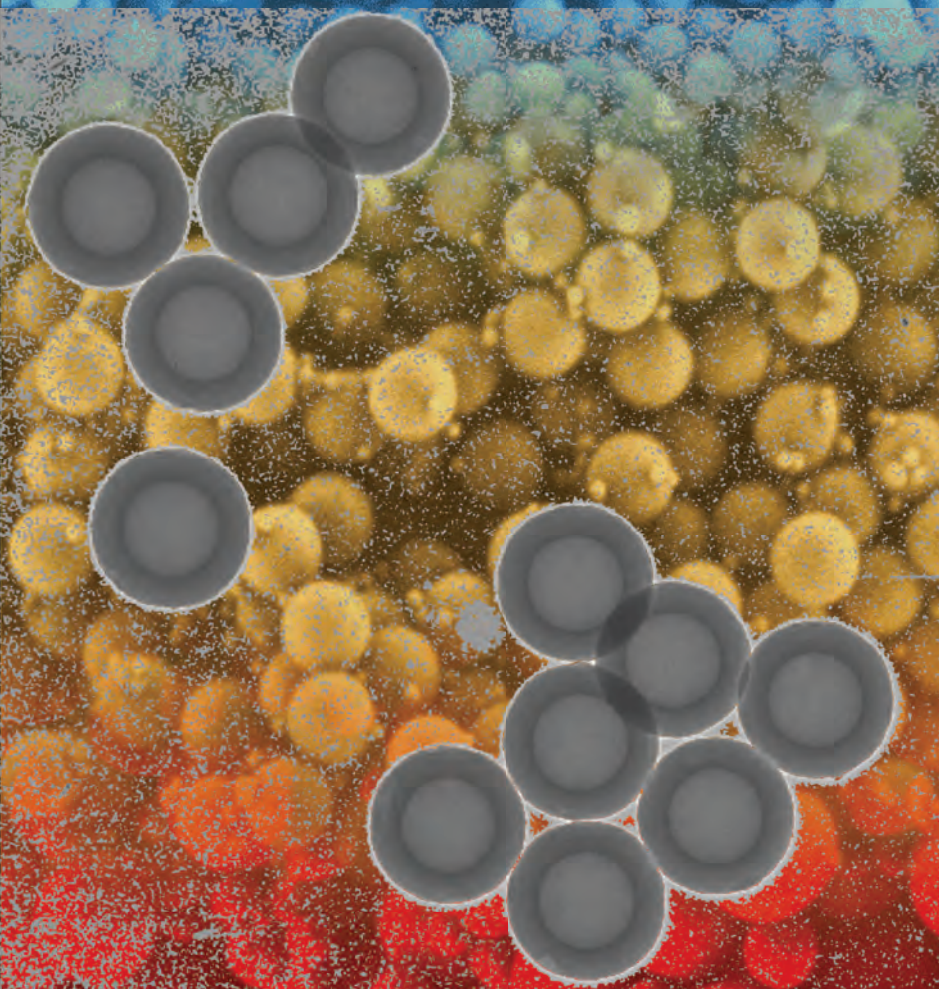

Figura 6. Imágenes SEM de CS producidas por HTC, comparación entre la síntesis de esferas que tienen PS (260 nm) como plantilla (derecha) con las que no (izquierda). Condiciones de síntesis para los dos casos: 160 °C, 10 horas y 1.9 M de glucosa.

NANO MICRO

small

32/2016

WILEY-VCH

Seeded Synthesis of Monodisperse Core–Shell and Hollow Carbon Spheres

C. López and co-workers

Seeded Synthesis of Monodisperse Core–Shell and Hollow Carbon Spheres

Luz Karime Gil-Herrera, Álvaro Blanco, Beatriz H. Juárez, and Cefe López*

The production of high-quality, monodisperse, non-agglomerated carbon spheres above 500 nm by colloidal means remains challenging. In this work, a detailed study of the parameters affecting the heterogeneous growth of carbon by hydrothermal carbonization has been performed. Polystyrene (PS) submicrometer spheres were used as seeds allowing to control the production of high-quality polystyrene-in-carbon hybrid spheres up to 900 nm with a relative standard deviation below 5%. Furthermore, the removal of the polymeric seeds by pyrolysis yields hollow carbon spheres keeping the narrow size distribution constant. These results may open new paths for the rational design of highly porous and well-defined tailored carbon materials for applications in key areas such as energy and photonics.

Monodisperse colloidal spheres either acting as a template or as a direct material are demanded in numerous applications such as sensors, batteries, supercapacitors, fuel cells, colloidal catalysis, sorption, drug delivery, or photonic crystals, among others.[1–4] Control over shape, size, surface functionality, porosity, and colloidal stability are essential properties for their successful integration in a wide range of applications. Depending on the functionality intended different materials are best suited. Recently, carbon spheres (CSs) of sizes ranging from nano- to micro-scale have drawn attention not only for their versatile properties, including high thermal stability and controlled reactivity by proper surface functionalization, but also for the sustainable synthesis, which can be carried out with the use of renewable carbon precursors.[5] Numerous methods have been developed for the fabrication of CSs including chemical vapor deposition (CVD),[6] pyrolysis of organic compounds,[7] arc-discharge,[8] nanocasting processes,[9] and hydrothermal carbonization (HTC),[10,11] which is based on the polymerization of carbon sources (e.g., monosaccharides[8] and polysaccharides[9])

L. K. Gil-Herrera, Dr. Á. Blanco, Prof. C. López
Instituto de Ciencia de Materiales de Madrid (ICMM)
Consejo Superior de Investigaciones Científicas (CSIC)
Calle Sor Juana Inés de la Cruz 3, 28049 Madrid, Spain
E-mail: c.lopez@csic.es
Dr. B. H. Juárez
Departamento de Química-Física Aplicada
Universidad Autónoma de Madrid
Av. Francisco Tomás y Valiente 7, 28049 Madrid, Spain
Dr. B. H. Juárez
Imdea Nanoscience
Faraday 9, 28049 Madrid, Spain
DOI: 10.1002/smll.201600902

initiated by the formation of C—O—C bonds.[12] These methods have been gathered in recent reviews.[13,14] Lately, HTC has been gaining ground because of the mild synthesis conditions required, giving high-purity products and its potential usage to produce hybrid materials including multifunctional core–shell,[15] hollow-shell,[16] or hard structure spheres.[10] Due to their facile removal, silica or polymeric spheres[17,18] (mainly PS) have been used as hard templates to fabricate hollow CSs.[13] The formation mechanism of carbon nanospheres by homogeneous nucleation and growth reaction, studied by Fourier Transform Infrared (FTIR) and X-ray Photoelectron Spectroscopy (XPS) has been previously proposed.[12] Since the first hard CSs fabricated via HTC, several modifications of the synthetic approach have been developed to produce a broad palette of multifunctional hybrid spheres, which can accommodate metals in the core[15] or produce metal oxide hollow spheres in post-thermal treatments.,[13,19] CSs can develop hierarchical porosity[20] or be organized into 3D structures.[21]

In general, the use of hollow CSs,[21–23] have special interest for energy production.[24] Likewise, assisting in the fabrication of photonic crystals,[2,25] CSs may play as building blocks not only because they can be assembled into a 3D structure with high packing efficiency, but also because they can be removed under orthogonal conditions.[26]

Despite recent progress in the synthesis of colloidal CSs by heterogeneous nucleation and growth,[9,27,28] the resultant CSs show relatively broad (above 5%) size distribution for spheres above 500 nm or yield irregular, non-spherical shapes. Thus, to fabricate high-quality monodisperse CSs ranging from 400 to 900 nm (the range of interest for optical applications) with very narrow size distribution (<5%) is still a great challenge.

Here, we present the synthesis of monodisperse CSs via HTC assisted by PS latex as seeds, which can be transformed into hollow CS by a simple thermal treatment. We take advantage of the PS features related to good colloidal stability and sphericity to better control the final morphology.[29] The use of PS spheres as template has recently been reported to produce high-quality hollow carbon spheres with sizes below 150 nm,[21] or larger ones in multistep synthetic approaches.[20] Our goal is, however, to achieve CSs ranging from 500 to 900 nm with size distribution below 5% by simple means. Our approach is based on a heterogeneous growth over PS seeds to produce PS@C hybrid spheres due to the adsorption of HTC glucose decomposition products over the PS surface without applying tedious synthetic

procedures. Special emphasis is given to optimize the experimental conditions in order to obtain high-quality spheres gaining control over parameters well described by the heterogeneous nucleation and growth principles.[30] Furthermore, the versatile PS@C hybrid spheres can also be used as templates to fabricate monodisperse, high-quality hollow CSs by pyrolysis. The resultant spheres show 10% shrinkage in diameter and preserve the initial size distribution. Furthermore, although pyrolysis is known to yield agglomerated products,[31] the hollow CSs reported here are non-aggregated. Other methods previously reported to avoid aggregation include multi-step methodologies such as the growth of intermediate SiO_2 layers,[20] the use of additional surfactants,[18] or even hypercrosslinking strategies.[32,33] To the best of the authors' knowledge, spherical, non-aggregated PS@C spheres and hollow CSs have never been reported with such control over size range and distribution by means of such simple, green, and straightforward methodology. Thus, broad interest is envisioned for both hybrid and hollow systems in the development of electrode materials in fuel cells, batteries, supercapacitors, supports in catalysis, or building blocks for the assembly of hierarchically complex structures such as opal-like ones working as photonic crystals in the IR.

Scanning electron microscopy (SEM) images in **Figure 1** show representative examples of PS_{490}@C hybrid spheres grown at different temperatures (160, 170, and 180 °C) and for three different glucose concentrations, namely, 0.35, 0.42, and 0.56 M after 8 h of reaction. Further information with data obtained for PS_{260}, PS_{330}, and PS_{549} including PS@C hybrid sizes, size distribution, shell thickness information, temperature, and employed glucose concentrations (including different values than those reported in Figure 1) can be found in Table S1 (Supporting Information). As can be seen in Figure 1, the HTC reaction of glucose in the presence of PS seeds at temperatures above 160 °C generates PS@C with diameters ranging from 550 to 1340 nm. Besides, the HTC treatment does not alter the spherical morphology of the initial PS seeds. The diameter of the PS@C spheres changes by modifying the operational conditions, according to the well-established factors affecting heterogeneous nucleation and growth. Images provided in Figure 1 illustrate the fact that certain reaction conditions lead to secondary populations of spheres. While selective precipitation methods can be employed to separate these populations the goal of this work is the direct production of non-aggregated, high-quality PS@C hybrid spheres in a wide size range of sizes, with very low polydispersity and avoiding the presence of secondary populations. To do so, several parameters have to be optimized including glucose concentration, temperature, and reaction time for different PS seed sizes. The concomitant relationship between temperature and glucose
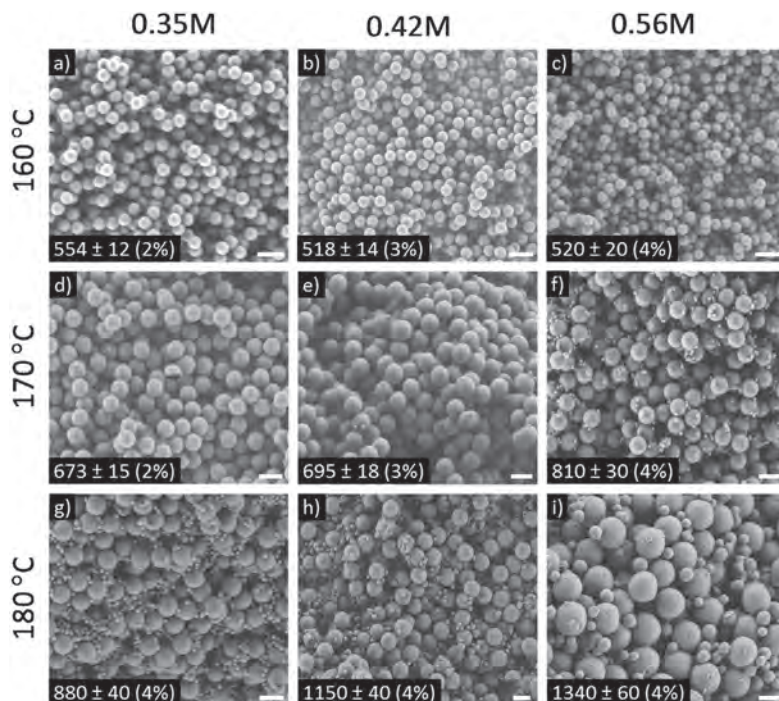

Figure 1. SEM images of PS_{490}@C hybrid spheres obtained at different HTC temperatures (160–180 °C) and glucose concentration after 8 h of reaction. Size of the main population of spheres ± standard deviation (in nm) and relative standard deviation (RSD) are also included. Scale bar, 1 µm.

concentration for a given reaction time (8 h in all cases) subject to the restriction of formation of PS@C spheres without secondary nucleation imposes limits on the ranges of glucose concentration and reaction temperature. In this particular case, these limits are 0.42 M and 170 °C. Higher concentration or higher temperature ends up in the appearance of a second population of small CSs as shown in Figure 1f–i. The upper temperature is limited to 180 °C where for different PS seeds, non-spherical and agglomerated products are observed (not shown).

These results are in good agreement with previous reports about CSs formation,[5,34] in the presence or absence of templates. Additionally, it is remarkable that the resulting PS@C hybrid spheres are not agglomerated in all cases. We believe this is the result of the use of glucose (which provides this advantage over other polysaccharides),[35] and the combination of the experimental conditions here reported, including the absence of additives or surfactants.[29] Table S1 (Supporting Information) shows the final sizes of PS@C hybrid spheres, covering a range from 279 up to 1500 nm (± 6%) including those samples in which a second population of spheres is present.

In order to describe the size increase through glucose carbonization, rather than providing a diameter ratio it is convenient to define a volume ratio $\gamma = V_f/V_i$ because it directly measures the carbon produced. Furthermore, since the synthesis of carbon occurs on the surface of the spheres present in the autoclave, which depends on the amount of seeds and their size, it is convenient to normalize that figure to the total surface available S. We define: $\gamma^* = \gamma/S$. **Figure 2** shows the γ^* ratio as a function of glucose concentration for several PS sizes at two temperatures (160 °C, black symbols and 170 °C, gray symbols) after 8 h of reaction time. Only data from reactions that yielded no secondary populations are shown. Normalization to the total available area for each

PS seed (determined by sphere size and amount) ensures a clear correlation for the carbon growth over equal areas. Overall, a clear trend is observed indicating that the increase in particle volume indeed responds to the glucose concentration. For PS260 seeds, the absolute final to initial volume ratio γ ranges from 1.5 up to 12 times for glucose concentration ranging from 0.2 to 1.1 M at 170 °C. This glucose concentration range can also be used for slightly larger seeds (PS330) without the formation of new nuclei and yielding similar volume increases at 160 °C. However, such a range must be reduced when larger seeds are used if secondary nucleation is to be prevented. For larger seeds, the available surface area decreases as the size squared leading to an effective supersaturation. For these cases, the possible glucose concentration is limited to 0.83 M or a second population of CSs is produced.

The growth rate with glucose concentration at higher temperature (170 °C) is higher and the range of glucose concentration for single population production is narrower as compared to lower temperature. The former effect is because temperature favors the hydrothermal reaction and the latter because the homogeneous synthesis is boosted by the scarcity of available surface. Thus, for samples with the lowest specific surface available (i.e., PS549), only low temperature and low supersaturation conditions yield a monodisperse product. In all cases, a linear tendency can be inferred. According to the literature and to our own results under similar concentrations, 180 °C is the common temperature employed for homogeneous nucleation and growth following the La Mer model, in which monodisperse particles are obtained by the separation of nucleation and growth from a supersaturated solution.[36] As is well known, temperature should be decreased in a heterogeneous growth in order to avoid the formation of secondary nuclei. This is in good agreement with the above reported results, in which temperatures in the range between 160 and 170 °C yield PS@C spheres without a second popula-

tion under the conditions reported here (at the same glucose and PS seed concentrations). However, as evidenced in Figure 2, higher temperatures provide faster growth (above twice in volume and an order of magnitude in size) which may be advantageous. In order to optimize 180 °C as synthesis temperature different reaction reactions have been explored.

Figure 3 shows the maximum glucose concentration preventing secondary populations for various conditions. These concentrations are plotted for 170 (left bars), 175 (middle bars), and 180 °C (right bars) and two reaction times, 6 (back, dashed bar) and 8 h (front, solid bar). One can readily see that higher temperature or longer reaction time lead to secondary spheres populations. For the glucose concentrations and PS seed sizes studied here, control over the reaction time is key when higher temperatures are employed.

The interdependence between glucose concentration and time is evidenced in
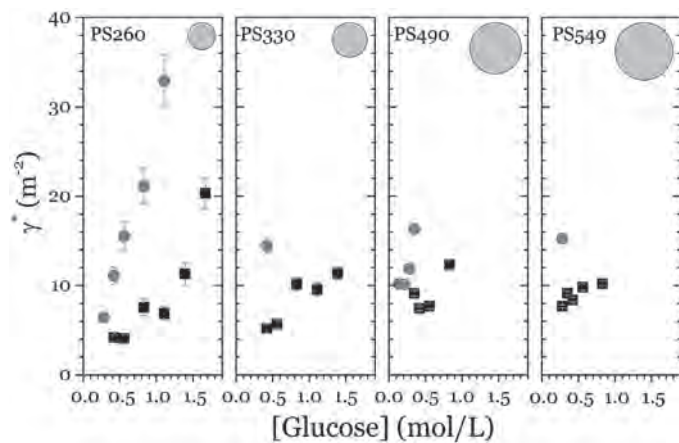
Figure 2. Final volume relative to the initial PS seed-size (γ^*) as a function of the glucose excluding reactions with second nucleation. The absolute volume ratios (γ) have been normalized to the total surface area for each seed size given in $m^2 \gamma^* = (V_f/V_i)/S$. Black symbols correspond to 160 °C and gray symbols to 170 °C reaction temperature. Seed sizes indicated graphically (gray circles) in each panel.
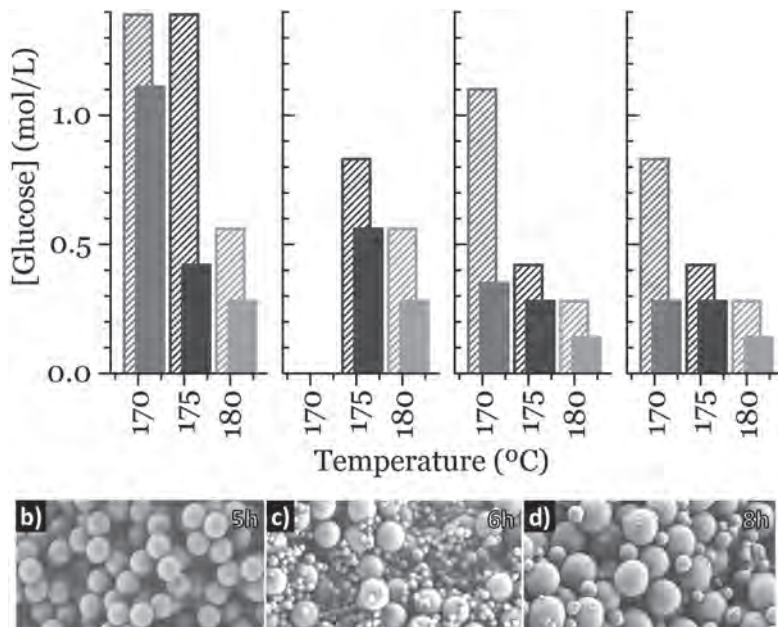
Figure 3. a) Maximum glucose concentration allowing heterogeneous growth of PS@C spheres as a function of temperature for several PS seeds (sizes indicated in each panel). Data from 8 (full bars) and 6 h (dashed bars) are shown. SEM images of PS_{490}@C hybrid spheres produced at 180 °C and 0.56 M of glucose concentration after b) 5, c) 6, and d) 8 h of reaction. Scale bar in all images: 1 μm.

the SEM images, where PS_{490}@C hybrid spheres are grown at a fixed glucose concentration of 0.56 M for 5 (Figure 3b), 6 (Figure 3c), and 8 h (Figure 3d), respectively. While 8 and 6 h of reaction yield PS_{490}@C hybrid spheres with clear secondary nucleation, reducing the reaction time to 5 h ends up in a very homogenous and monodisperse product. Data including reaction times for additional glucose concentrations are summarized in Table S1 (Supporting Information), which also includes information about the tunability of the shell thickness. Optimizing temperature, glucose concentration, time, and seed size, the shell carbon thickness in hybrid PS@C spheres (showing no second population) can be varied between 0.1 and 1.2 times the radius of the PS seed (see the Supporting Information).

We believe that the control over monodispersity avoiding secondary nucleation exerted by reaction time is related to the evolution of functional groups on the surface of the CSs as the reaction proceeds. As has been reported,[12,29] the evolution of the carbonization reaction implies an increase in the formation of double carbon bonds. We suggest that the increase in double carbon bonds as glucose carbonization proceeds (producing harder spheres) might promote the second population observed at high temperature. Although out of the scope of this work, the secondary spheres growing off the parent spheres observed in several SEM inspections (not shown), attest to an effect previously observed in other systems.[37]

As mentioned before, hollow CSs can be obtained by further calcination of PS@C hybrids spheres in an air

atmosphere. **Figure 4** shows transmission electron microscopy (TEM) images at different magnifications of the hollow spheres obtained from initial PS_{260}@C hybrid spheres. TEM images evidence the quality and monodispersity of the samples after the thermal procedure. A shrinkage of about 10% in diameter, 25% in volume can be detected (TEM of spheres prior to pyrolysis shown in Figure 4b Inset). Figure 4c shows the thermogravimetric analysis of PS_{260}@C hybrid spheres from RT to 600 °C. Here, a weight loss is apparent from 300 °C. The inflection point (highlighted by a deep minimum in the first derivative of the weight loss curve) indicates the largest rate of change at 437 °C. This mass loss can be assigned to the PS decomposition. At 600 °C 50% of the material still remains. At this temperature, the mass loss might be due to different carbonization process into carbon network.

The porosities of both the PS@hybrid system and hollow CS have been evaluated by N_2 adsorption measurements (see Figure S1, Supporting Information). These measurements show that CSs present type-I isotherms, indicative of the microporous structure and a marked N_2 adsorption below $P/P_0 \approx 0.04$. The PS@C hybrid spheres have a low porosity, the Brunauer–Emmett–Teller (BET) surface area being less than 10 m² g⁻¹ which roughly corresponds to the geometric area of the spheres. In contrast, hollow CSs increase their surface area to 540 m² g⁻¹ after pyrolysis at 500 °C or to 860 m² g⁻¹ at 800 °C with specific pore volumes of 0.2 and 0.32 cm³ g⁻¹, respectively. The surface area increase at those temperatures is due to elimination of volatile compounds by
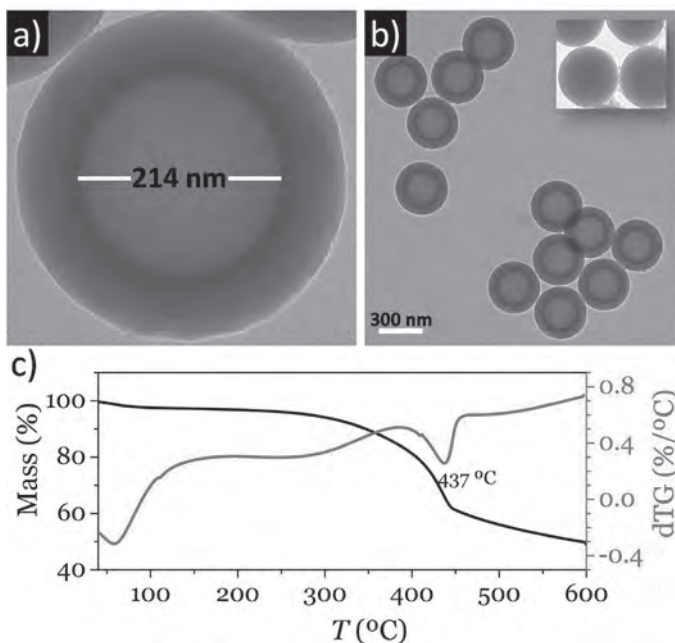
Figure 4. a,b) TEM images of hollow CSs obtained after calcination of PS_{260}@C hybrid spheres. Inset in (b) shows solid-core hybrid spheres prior to pyrolysis for comparison (same magnification). c) Thermogravimetric analysis (TGA) curve evidencing a weight loss of almost 50% around 400 °C, corresponding to the removal of PS cores.

carbonization leading to highly microporous carbon-based shell framework. Additionally, the homogenous porosity on carbon shell is confirmed by pore diameter distribution (see Figure S2, Supporting Information). Pyrolysis at 500 °C creates pores with sizes distributed around 1.2 nm with an incipient additional population centered around 1.6 nm for 800 °C which we believed is related with other degasification reactions.

FTIR spectra show that oxygen groups are present on the spheres surface (see Figure S3, Supporting Information). The –OH ($\nu = 3400$ cm^{-1}) and C=O ($\nu = 1704$ cm^{-1}) vibrations decrease when the pyrolysis temperature is increased, which suggests a hydrophobic surface after PS removal.

Summarizing, in this work a systematic study of factors affecting the synthesis of carbon spheres by heterogeneous nucleation and growth is reported. Fine control over temperature, time, glucose concentration, and size of the initial seed (polystyrene beads), allows the synthesis of excellent hybrid polystyrene-carbon spheres in terms of size distribution (bellow 5%), and shape with no-aggregation in a size range between 500 and 900 nm. The hybrid polystyrene-carbon spheres can be easily transformed by pyrolysis in hollow carbon spheres with preserved monodispersity. This approach provides a synthetic route not only because it yields highly monodisperse spheres, in contrast with traditional HTC glucose products, but also because it offers a control method to synthesize functional hollow carbon spheres with potential in energy applications.

Experimental Section

Chemicals: Polystyrene latex aqueous dispersions (10% vol) were purchased form Fisher or microParticles GmbH. PS sphere sizes employed were 260, 330, 490, and 549 nm, which are referred to as PS_{xxx}, where *xxx* denotes the corresponding sphere diameter in nm. For all seeds the standard deviation measured was less than 5%. Glucose (99.9%) was purchased from Aldrich and used without further purification.

Synthesis Methods: In a typical procedure, proper amounts of glucose were dissolved in deionized water to prepare glucose solutions with concentrations ranging from 0.1 to 1.7 mol L^{-1}. To these solutions, PS aqueous suspensions were added and further transferred into a 40 mL Teflon-lined stainless steel autoclave, maintained at 160–200 °C for 6–20 h. In order to avoid overpressure, the Teflon vessel was filled to 80% of its maximum capacity. After the HTC reaction, the autoclave was cooled down to room temperature. The dark solid obtained was thoroughly isolated by three cycles of centrifugation/washing/redispersion in deionized water, followed by similar cycles in ethanol, and dried overnight at 80 °C. The resulting hybrid CSs are labeled PS_{xxx}@C, where *xxx* refers to the PS seed size in nm given by the supplier. The diameter and standard deviation of the most representative experiments are listed in Table S1 (Supporting Information). Hollow CSs were obtained by pyrolysis under N$_2$ gas, under temperatures of 500 and 800 °C.

Characterization: The morphology and sizes of PS@C hybrid spheres and hollow CS were evaluated by an FEI NovaNano SEM 230 scanning electron microscope and/or a JEOL-2000 FXII transmission electron microscope, operating at 200 kV. The size distribution was obtained from the analysis of 100 spheres in each case by SEM. Although TEM is likely to provide more accurate size values than SEM, no significant differences have been observed between them. Thermogravimetric analysis (TGA) was performed by using a Thermal Analysis SDT Q600 TA Instruments under a nitrogen flowing atmosphere (100 mL min^{-1}) at a heating rate of 20 °C min^{-1}. Surface areas were evaluated using the BET method from nitrogen adsorption–desorption isotherms. The nitrogen adsorption measurements were performed in an Autosrb-1 from Quantachrom Instruments at 77 K in the relative pressure range 10^{-6} to 1 atm. Prior to measurement, the samples were degassed overnight at 120 °C. Pore size distributions were calculated by density functional theory (DFT) methods via the adsorption branch. Infrared spectra were collected in a Bruker IFS 66VS.

Supporting information

Supporting Information is available from the Wiley Online Library or from the author.

[1] X. Chen, K. Kierzek, K. Wenelska, K. Cendrowski, J. Gong, X. Wen, T. Tang, P. K. Chu, E. Mijowska, *Chem. - Asian J.* **2013**, *8*, 2627.

[2] J. F. Galisteo-López, M. Ibisate, R. Sapienza, L. S. Froufe-Pérez, Á. Blanco, C. López, *Adv. Mater.* **2011**, *23*, 30.

[3] A. D. Roberts, X. Li, H. Zhang, *Chem. Soc. Rev.* **2014**, *43*, 4341.

[4] J. Zhou, C. Tang, B. Cheng, J. Yu, M. Jaroniec, *ACS Appl. Mater. Interfaces* **2012**, *4*, 2174.

[5] M.-M. Titirici, M. Antonietti, N. Baccile, *Green Chem.* **2008**, *10*, 1204.

[6] H. Qian, F. Han, B. Zhang, Y. Guo, J. Yue, B. Peng, *Carbon* **2004**, *42*, 761.

[7] Y. Jin, C. Gao, W. Hsu, Y. Zhu, *Carbon* **2005**, *43*, 1944.

[8] W. M. Qiao, Y. Song, S. Y. Lim, S. H. Hong, S. H. Yoon, I. Mochida, T. Imaoka, *Carbon* **2006**, *44*, 187.

[9] T. Nakamura, Y. Yamada, K. Yano, *Microporous Mesoporous Mater.* **2009**, *117*, 478.

[10] Q. Wang, H. Li, L. Chen, X. Huang, *Carbon* **2001**, *39*, 2211.

[11] M.-M. Titirici, M. Antonietti, *Chem. Soc. Rev.* **2010**, *39*, 103.

[12] a) P. N. Bhagat, K. R. Patil, D. S. Bodas, K. M. Paknikar, *RSC Adv.* **2015**, *5*, 59491; b) J. Ryu, Y. W. Suh, D. J. Suh, D. J. Ahn, *Carbon* **2010**, *48*, 1990.

[13] J. Liu, N. P. Wickramaratne, S. Z. Qiao, M. Jaro-niec, *Nat. Mater.* **2015**, *14*, 763.

[14] R. Ghosh Chaudhuri, S. Paria, *Chem. Rev.* **2012**, *112*, 2373.

[15] X. Sun, Y. Li, *Angew. Chem., Int. Ed.* **2004**, *43*, 3827.

[16] M. Titirici, M. Antonietti, A. Thomas, *Chem. Mater.* **2006**, *18*, 3808.

[17] A. H. Lu, T. Sun, W. C. Li, Q. Sun, F. Han, D. H. Liu, Y. Guo, *Angew. Chem., Int. Ed.* **2011**, *50*, 11765.

[18] R. J. White, K. Tauer, M. Antonietti, M.-M. Titirici, *J. Am. Chem. Soc.* **2010**, *132*, 17360.

[19] X. Sun, J. Liu, Y. Li, *Chem. Eur. J.* **2006**, *12*, 2039.

[20] M. Titirici, A. Thomas, Y. Ao, *Adv. Funct. Mater.* **2007**, *17*, 1010.

[21] S.-K. Kim, E. Jung, M. D. Goodman, K. S. Schweizer, N. Tatsuda, K. Yano, P. V. Braun, *ACS Appl. Mater. Interfaces* **2015**, *7*, 9128.

[22] Y. Xia, R. Mokaya, *J. Mater. Chem.* **2005**, *15*, 3126.

[23] Y. Gong, Z. Wei, J. Wang, P. Zhang, H. Li, Y. Wang, *Sci. Rep.* **2014**, *4*, 6349.

[24] X. Chen, K. Kierzek, K. Wenelska, K. Cendrowski, J. Gong, X. Wen, T. Tang, P. K. Chu, E. Mijowska, *Chem. - Asian J.* **2013**, *8*, 2627.

[25] G. von Freymann, V. Kitaev, B. V. Lotsch, G. a. Ozin, *Chem. Soc. Rev.* **2013**, *42*, 2528.

[26] M. D. Goodman, K. A. Arpin, A. Mihi, N. Tatsuda, K. Yano, P. V. Braun, *Adv. Opt. Mater.* **2013**, *1*, 300.

[27] J. Zhao, W. Niu, L. Zhang, H. Cai, M. Han, Y. Yuan, S. Majeed, S. Anjum, G. Xu, *Macromolecules* **2013**, *46*, 140.

[28] M. Li, W. Li, S. Liu, *Carbohydr. Res.* **2011**, *346*, 999.

[29] M.-M. Titirici, R. J. White, N. Brun, V. L. Budarin, D. S. Su, F. del Monte, J. H. Clark, M. J. MacLachlan, *Chem. Soc. Rev.* **2015**, *44*, 250.

[30] a) *Nanoparticles* (Ed: C. de Mello Donegá), Springer, Berlin **2014**; b) C. J. Brinker, G. W. Scherer, *Sol-Gel Science*, Academic Press, Boston, USA **1990**.

[31] J. E. Im, H. N. Lee, J. Li, Y. R. Kim, *Bull. Korean Chem. Soc.* **2014**, *35*, 871.

[32] Y. Ouyang, H. Shi, R. Fu, D. Wu, *Sci. Rep.* **2013**, *3*, 1430.

[33] K. Wang, L. Huang, S. Razzaque, S. Jin, B. Tan, *Small* **2016**, *12*, 3134.

[34] C. Falco, N. Baccile, M.-M. Titirici, *Green Chem.* **2011**, *13*, 3273.

[35] M. Sevilla, A. B. Fuertes, *Chem. - Eur. J.* **2009**, *15*, 4195.

[36] a) V. LaMer, R. Dinegar, *J. Am. Chem. Soc.* **1950**, *72*, 4847; b) T. Sugimoto, *Adv. Colloid Interface Sci.* **1987**, *28*, 65.

[37] A. D. Randolph, M. A. Larson, *Theory of Particulate Processes*, Academic Press, San Diego, **1988**.

NANO ‖ MICRO

small

Supporting Information

Seeded Synthesis of Monodisperse Core–Shell and Hollow
Carbon Spheres

*Luz Karime Gil-Herrera, Álvaro Blanco, Beatriz H. Juárez,
and Cefe López**

Seeded Synthesis of Monodisperse Carbon Spheres

Luz Karime Gil-Herrera,[1] Álvaro Blanco,[1] Beatriz H. Juárez,[2,3] Cefe López[1]*

[1]Instituto de Ciencia de Materiales de Madrid (ICMM), Consejo Superior de Investigaciones Científicas (CSIC); Calle Sor Juana Inés de la Cruz 3, 28049 Madrid, Spain

[2]Departamento de Química-Física, Universidad Autónoma de Madrid, Av. Francisco Tomás y Valiente, 28049 Madrid, Spain

[3]IMDEA Nanoscience, Faraday 9, 28049, Cantoblanco, Madrid, Spain.

Corresponding Author

ICMM, email address c.lopez@csic.es

Table S1 data summarize PS@C hybrid sizes, size distribution, temperature and employed glucose concentration. Shading rows means samples with only one main population.

	Glucose (mol/L)	Time (h)	T (°C)	Particle Size (nm)	SDd (nm)	Monodispersity (%)	Shell thickness (nm)	Shell to diameter ratio
PS₂₆₀@C	1.11	4	190	800	40	5	279	2.3
	1.39			710	30	3	234	1.9
	1.48			930	40	4	344	2.8
	1.11	5	180	515	17	3	136	1.1
	1.11		190	930	60	6	344	2.8
	0.42	6	170	368	16	4	63	0.5
	0.56			367	14	4	62	0.5
	0.83			367	12	3	62	0.5
	1.11			370	11	3	64	0.5
	1.39			469	14	3	113	0.9
	1.67			400	20	5	79	0.6
	0.56		175	326	12	4	42	0.3
	0.83			351	19	5	54	0.4
	1.11			410	20	5	84	0.7
	1.39			530	20	4	144	1.2
	1.67			650	30	5	204	1.7
	0.28		180	322	14	4	40	0.3
	0.42			391	16	4	74	0.6
	0.56			409	17	4	83	0.7
	0.83			600	30	5	179	1.4
	0.42	8	160	281	10	4	19	0.1
	0.56			279	13	5	18	0.1
	0.83			340	20	6	49	0.4
	1.11			332	16	5	45	0.4
	1.39			390	20	5	74	0.6

	1.67			477	14	3	117	0.9
	0.19		170	325	10	3	41	0.3
	0.42			390	11	3	74	0.6
	0.56			436	19	4	97	0.8
	0.83			483	17	4	120	1.0
	1.11			560	18	3	159	1.3*
	1.39			620	20	3	189	1.5
	1.67			729	17	2	243	2.0
	0.28		175	398	13	3	78	0.6
	0.35			403	10	2	80	0.6
	0.42			450	20	4	104	0.8
	0.56			580	20	3	169	1.4
	0.83			670	20	3	214	1.7
	0.14		180	362	18	5	60	0.5
	0.21			383	15	4	70	0.6
	0.28			469	14	3	113	0.9
	0.35			472	17	4	115	0.9
	0.42			502	18	4	130	1.0
	0.56			647	19	3	202	1.6
	0.56[a]		190	840	40	5	299	2.4
	0.56[b]		200	1590	1800	113	674	5.5
PS$_{330}$@C	0.42	6	175	402	18	4	50	0.3
	0.83			477	11	2	88	0.6
	0.83		180	584	15	3	141	0.9
	0.42	8	160	354	13	4	26	0.2
	0.56			364	14	4	31	0.2
	0.83			442	16	4	70	0.5
	1.11			430	20	5	64	0.4
	1.39			459	12	3	79	0.5
	1.67			553	12	2	126	0.8
	0.42		170	497	11	2	98	0.6
	0.56			496	15	3	97	0.6
	0.83			620	20	3	159	1.1
	1.39			870	30	3	284	1.9
	0.56		175	710	20	3	204	1.4
	0.56		180	630	20	3	164	1.1
	0.56[a]		190	1050	40	4	374	2.5
	0.56[b]		200	1110	400	36	404	2.7
PS$_{490}$@C	0.28	4	180	513	10	2	22	0.1
	0.56			531	12	2	31	0.1
	0.83			576	15	3	53	0.2
	1.11			780	20	3	155	0.7
	0.42		190	730	20	3	130	0.6
	0.56			802	33	4	166	0.7
	0.42	5	180	653	17	3	92	0.4
	0.56			639	19	3	85	0.4
	0.83			710	20	3	120	0.5
	0.42		190	930	70	8	230	1.0
	1.48			1400	--		465	2.0
	0.42	6	170	538	13	2	34	0.1

Label								
	0.56			593	12	2	62	0.3
	0.83			610	20	3	70	0.3
	1.11			650	18	3	90	0.4
	1.39			934	30	3	232	1.0
	0.14		175	498	19	4	14	0.1
	0.21			542	16	3	36	0.2
	0.28			520	20	4	25	0.1
	0.35			604	14	2	67	0.3
	0.42			672	16	2	101	0.4
	0.56			670	30	4	100	0.4
	0.83			737	15	2	134	0.6
	0.14		180	599	13	2	65	0.3
	0.28			630	15	2	80	0.3
	0.35			630	13	2	80	0.3
	0.42			790	30	4	160	0.7
	0.56			930	20	2	230	1.0
	0.35	8	160	554	12	2	42	0.2
	0.42			518	14	3	24	0.1
	0.56			520	20	4	25	0.1
	0.83			610	20	3	70	0.3
	0.97			687	17	2	109	0.5
	1.11			720	19	3	125	0.5
	0.14		170	558	10	2	44	0.2
	0.21			557	17	3	44	0.2
	0.28			606	15	2	68	0.3
	0.35			673	15	2	102	0.4
	0.42			695	18	3	113	0.5
	0.56			810	20	2	170	0.7
	0.83			1030	40	4	280	1.2
	1.11			1000	40	4	265	1.1
	0.14		175	604	16	3	67	0.3
	0.21			671	18	3	101	0.4
	0.28			689	16	2	110	0.5
	0.35			660	30	5	95	0.4
	0.42			710	20	3	120	0.5
	0.56			850	40	5	190	0.8
	0.14		180	690	30	4	110	0.5
	0.21			675	18	3	103	0.4
	0.28			758	17	2	144	0.6
	0.35			880	40	4	205	0.9
	0.42			1150	40	4	340	1.4
	0.56			1340	60	4	435	1.9
PS$_{549}$@C	0.42	6	170	650	20	3	54	0.2
	0.56			688	16	2	73	0.3
	0.83			940	20	2	199	0.7
	0.42		175	680	20	3	69	0.3
	0.56			830	20	2	144	0.5
	0.83			810	30	4	134	0.5
	0.14		180	572	12	2	15	0.1
	0.28			667	19	3	62	0.2

0.35			870	30	3	164	0.6	
0.42			740	30	4	99	0.4	
0.56			896	19	2	177	0.7	
0.28			573	12	2	15	0.1	
0.35			607	16	3	32	0.1	
0.42		160	590	20	3	24	0.1	
0.56			620	30	5	39	0.1	
0.83			630	20	3	44	0.2	
0.28			720	20	3	89	0.3	
0.35		170	700	20	3	79	0.3	
0.42	8		710	20	3	84	0.3	
0.56			910	40	4	184	0.7	
0.28		175	700	20	3	79	0.3	
0.56			1130	70	6	294	1.1	
0.28			800	30	4	129	0.5	
0.35		180	760	30	4	109	0.4	
0.42			1040	40	4	249	0.9	
0.56			1380	80	6	419	1.5	

[a]Necklace-like spheres

[b]Non-spherical

Figure S1 Nitrogen adsorption curves for PS@C hybrid spheres and for hollow spheres pyrolyzed at 500 ºC and 800 ºC. Full symbols correspond to adsorption and open symbols to desorption.
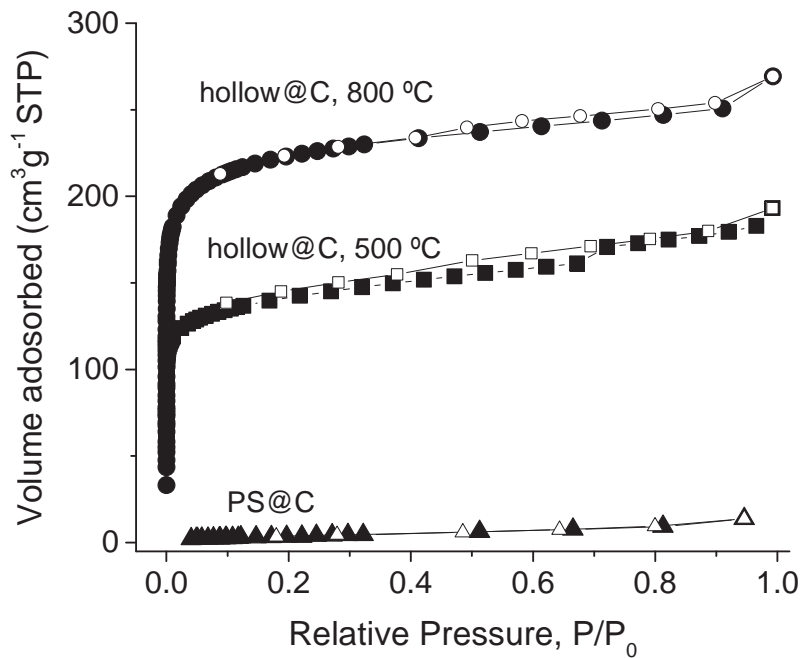
Figure S2 Pore diameter distribution as derived from Nitrogen adsorption isotherms for hollow spheres pyrolyzed at 500 ºC and 800 ºC.
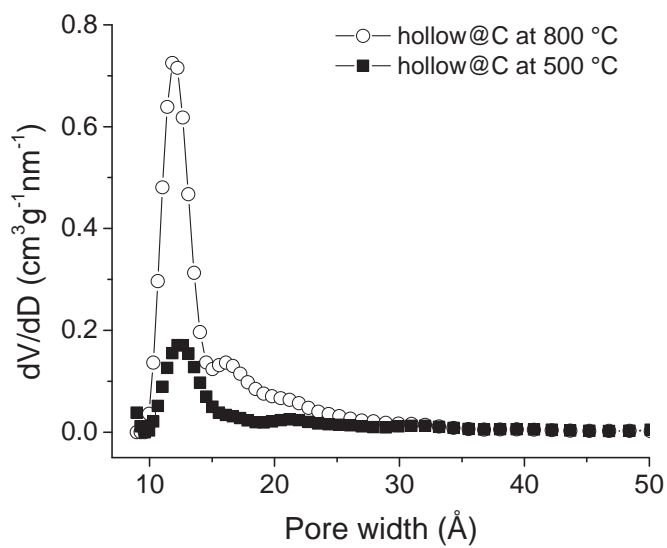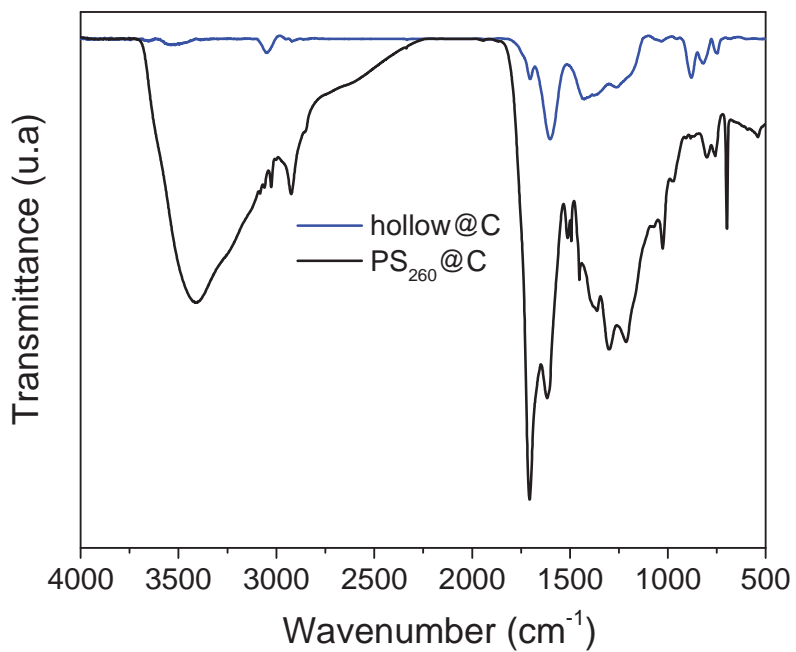
Figure S3 FTIR spectra from PS@C hybrid spheres and for hollow spheres pyrolyzed at . 500 ºC.

Ópalos Carbonosos

La fabricación de sistemas fotónicos carbonosos implica estrategias complejas que involucran varios pasos[21,56,57] limitando la obtención de ópalos de alta calidad. Por tal motivo, se plantea un procedimiento alternativo para el ordenamiento de las CSs en un arreglo fcc. Teniendo en cuenta su naturaleza coloidal, las CSs son autoensambladas mediante una modificación del método de deposición vertical (Figura 7a). Se introduce el sustrato de forma horizontal en el coloide para lograr una mayor área superficial en contacto, lo que favorece el equilibrio de los diferentes procesos involucrados. La estabilidad coloidal de las CS está determinada por el balance de las fuerzas electrostáticas superficiales, que a su vez dependen de la carga superficial (potencial zeta). Así pues, el movimiento de las partículas estará dirigido por el equilibrio de las cargas superficiales en medio acuoso y/o alcohol, según sea el caso. De las esferas sintetizadas por HTC se sabe que, debido a la presencia de grupos C(O) superficiales, poseen una superficie débilmente ácida lo que ocasiona una carga superficial negativa en un amplio rango de pHs que a su vez se traduce en un potencial zeta negativo alto.[58] En el presente caso, la forma coloidal más estable de las CS es en una solución de H_2O:EtOH (3:1) que presenta un potencial zeta de -60 mV, a pH ~6, que es un valor alto comparado con lo reportado en la literatura.[56] Por otro lado, tras la pirólisis, la superficie cambia significativamente al ser eliminados los C(O), lo que produce una disminución del potencial zeta y, en consecuencia, una

menor estabilidad coloidal.[59] Por tal motivo, la formación del ópalo se produce con las esferas en su forma híbrida y no en su configuración hueca.

La figura 7 muestra ópalos de carbono de diferentes tamaños. En la imagen óptica se observa la extensión del área recubierta, confirmando el éxito de la deposición horizontal. Las figuras 7b y 7c, muestran las diferentes capas y dominios del ordenamiento de las esferas, evidenciando, no solo el arreglo en el plano x-y, sino también en el eje z. Asimismo, en la micrografía SEM se evidencia que, pese a las fracturas y dislocaciones, la extensión del área ordenada alcanza valo-
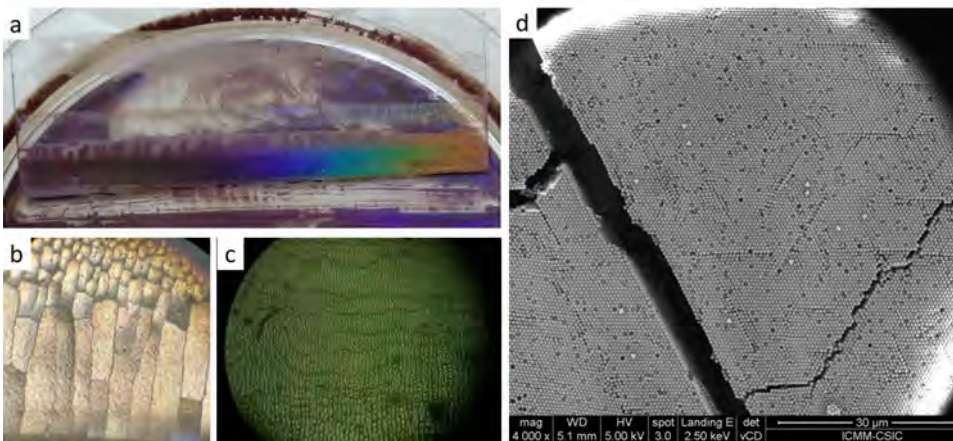

Figura 7. Ópalos de carbono producidos por autoensamblamiento de CS. a) imagen óptica tras el proceso de deposición de las CS que muestra colores estructurales según el ángulo de exposición. b-c) imágenes ópticas donde se observa los dominios y las capas de crecimiento de los ópalos. d) imagen SEM de un ópalo que muestra fracturas y dislocaciones.

res por arriba de los 60 μm^2.

En cuanto a la respuesta óptica, una característica relevante a tener en cuenta es la absorción en el rango visible del carbono. Aunque esta es una limitación en sistemas fotónicos, las partículas carbonosas han sido utilizadas para disminuir el esparcimiento de luz difusa a través de la estructura, lo que ocasiona un aumento en la intensidad de luz reflejada y así, un aumento en la pureza cromática de la coloración estructural.[57,60] En el presente caso, se ha confirmado tal efecto y los ópalos PS@C obtenidos presentaron una alta iridiscencia y colores brillantes a pesar de la absorción inherente del carbón, como se puede observar en la figura 7.

El ordenamiento de esferas PS@C con diferentes tamaños (tanto en la corteza carbonosa como en el tamaño final de partícula) da lugar a un amplio rango de longitudes de onda en los que se puede generar un pseudogap. Así, se ha logrado generar picos Bragg desde 0.6 μm hasta casi 2 μm, un rango bastante codiciado en aplicaciones tales como telecomunicaciones. Por otro lado, al aumentar el grosor de la corteza carbonosa (e.g. de 45 a 210 nm), el promedio del índice de contraste del sistema PS@C aumenta levemente, ocasionando un corrimiento del pico Bragg hacia longitudes de onda mayores (λ de 0.8 a 1.2 um). La evolución del pseudogap en función de la cantidad de carbono en la esfera es estudiado mediante MPB (paquete de cálculo de estructuras de bandas del MIT).[61,62] Mediante esta metodología es posible determinar la estructura de bandas de numerosos tipos de

cristales fotónicos,[6] para lo cual se puede encontrar un análisis deta-
llado del método de cálculo en la referencia [63]. De acuerdo al cálculo
de bandas para este sistema y lo observado experimentalmente, se
comprueba que todos los picos Bragg concuerdan tanto en posición
como en anchura con las predicciones teóricas. Debe tenerse en cuenta
que este tipo de cálculos no considera la componente imaginaria de la
función dieléctrica proveniente de la absorción del carbono y por tal
motivo, en un futuro debería ser planteado un estudio teórico más
profundo.

Como ya se ha mencionado, el tratamiento térmico del ópalo
PS@C conlleva la eliminación del PS y el ópalo hollow@C resultante
posee una configuración *closed-cell*, es decir, esferas de aire rodeadas
por una corteza carbonosa que, de acuerdo a la literatura, presentan
una alta resistencia mecánica.[64] Se evaluaron dos temperaturas: 365
°C, que es la temperatura a la cual típicamente se infiltra Si mediante
CVD,[23] y 480 °C, temperatura en la que se asegura que todo el PS ha
sido eliminado, y en que el desarrollo en la porosidad no compromete
la calidad de la estructura o cambie su tamaño significativamente.

El desarrollo de la porosidad jerarquizada ocurre a tres niveles
bien definidos: microporosidad en la corteza, mesoporosidad en los
intersticios entre esferas y macroporosidad en la cavidad interna de las
CS. La **microporosidad** en la corteza, es el resultado de la descomposi-
ción de C(O) en la superficie, dejando carbonos reactivos que se
reorganizarán para dar lugar a poros interconectados y a una superficie

menos hidrofílica. Tal disminución en el carácter hidrofílico tras la pirólisis podría ser de gran utilidad en la fabricación de sistemas ordenados con aplicaciones en adsorción selectiva de líquidos y/o gases. En definitiva, a mayor temperatura de pirólisis, más complejos C(O) se descomponen dejando un mayor desarrollo de la porosidad. La **mesoporosidad** propia del ópalo, en principio, no es afectada por el tratamiento térmico y su estructura fcc es conservada. Por último, la **macroporosidad,** heredada por el tamaño del PS, se desarrolla cuando la temperatura de descomposición del PS es alcanzada; así, a 365 °C, tal descomposición aún no ha finalizado y el PS sigue estando presente.

Es importante recalcar que el encogimiento que sufren las esferas huecas, principalmente en la corteza carbonosa, ocasiona una compactación en toda la estructura y produce fracturas; sin embargo, el pico Bragg permanece, señal de que el orden a través de la estructura es conservado. Consecuentemente, la respuesta fotónica del hollow@C depende del tratamiento térmico aplicado, por lo que es factible caracterizar el sistema mediante el desarrollo de la porosidad, tanto por tamaño de poro como por la cantidad. En términos generales, al haber una mayor cantidad de poros, el promedio de índices de contraste disminuye y por lo tanto se observa un corrimiento del pico Bragg a longitudes de onda menores. La caracterización óptica con el desarrollo de la porosidad, se lleva a cabo mediante la medición de la humedad: el vapor de agua entra en los poros de la estructura cam-

biando el índice de refracción promedio de la estructura y genera así un cambio en el pico Bragg.

La gran sensibilidad de la medida queda patente cuando los microporos del ópalo hollow@C son infiltrados a muy baja humedad, por debajo del 0.5%, suficiente para producir un cambio en la respuesta óptica. Este aspecto es muy relevante en aplicaciones de sensores o para determinar el área de algunos materiales, especialmente para aquellos con los que se cuenta con muy poca cantidad de muestra. Típicamente, las medidas de fisisorción requieren cantidades de muestra grandes para dar resultados fiables, lo cual limita su uso, especialmente en materiales que se encuentran recubriendo una superficie, e.g. un ópalo. Por lo tanto, un desarrollo más profundo de este tipo de técnicas mediante la evolución del pico Bragg en sistemas porosos sería una contribución importante en el campo de la ciencia de materiales.

FULL PAPER

Porous Carbons

**ADVANCED
FUNCTIONAL
MATERIALS**

www.afm-journal.de

Hierarchically Porous Carbon Photonic Structures

Luz Karime Gil-Herrera, Jose Angel Pariente, Francisco Gallego-Gómez, Felipe Gándara, Beatriz H. Juárez, Álvaro Blanco, and Cefe López*

Hierarchically porous carbon holds promise for many applications involving not only electrical, catalytic, power storage and related functionalities but, despite absorption in the visible and near-infrared, also optical and sensing uses are envisaged. In this paper, the self-assembly of heterogeneous core–shell and hollow carbon spheres based on polystyrene cores, their optical properties and their response to humidity are described. The remarkable high quality of the crystals permits to exploit their singular optical properties among which a very high sensitivity to adsorption of guest materials stands out. In this regard, an original characterization of the system response is performed by means of the photonic bandgap variation with the relative gas pressure. Controlled pyrolysis enables to create and tune the features of the porosity brought about by degassing and the restructuring of the carbon lattice. Functionality associated with diverse pore populations reveals sensitivity to diverse ranges of humidity owing to selective adsorption of water in different size pores.

1. Introduction

Porous carbon materials in general attract extensive research nowadays for their appealing properties, including high surface area, large pore volume, and unique pore size distribution.[1] They are becoming very versatile components in many different functional systems such as next-generation lithium batteries,[2] as electrodes for supercapacitors,[3] or hydrogen storage systems,[4] to name a few. In particular, carbon spheres have lately been proposed for use in soft lithography,[5,6] or nanostructured templates.[7] Compared to typically employed materials like polystyrene (PS), polymethylmethacrylate (PMMA), or silica,

carbon spheres provide strong resilience against extreme process conditions, high thermal stability, and excellent monodispersity and size control.[8–10] Besides, their surface functionalization enables a broad range of synthetic strategies making possible their combination with other materials for carbon-based structures exhibiting synergetic functionalities.[11] Most of the mentioned applications dispense with the arrangement of spheres in any particular order. However, a singularly interesting prospect is revealed by the possibility to assemble (porous) carbon spheres to form 3D structures. (3D-) ordered assemblies of colloidal particles offer a versatile opportunity to open new paths for the rational design of highly porous and well-defined tailored materials. In this way, a 3D-interconnected system with multiscale, hierarchical porosity is still a current challenge, specifically in fields where diffusion or transport is essential.[12,13]

In general, artificial opals are the most widespread and successfully developed 3D hard templates prepared in the last few years and the most straightforward and inexpensive approach to obtain 3D photonic crystals (PCs) by means of self-assembly of sub-micrometer colloidal particles.[14] They are suitable structures where light–matter interactions can be enhanced, suppressed, or modified at will with anticipated applications in different fields such as optoelectronics, energy, storage, sensors,[15] and, more recently, in biochemistry and biomedicine[16] or even as model systems.[17–19] Although the inherent high optical absorption of carbon in the visible range can be a drawback in photonics,[20] carbon particles are playing an important role in decreasing incoherent light scattering in photonic structures aimed at the enhancement of the structural colors.[21–23]

Historically, the fabrication of carbon PCs has been tackled mainly by the infiltration of different carbon precursors (such as polyfurfural alcohol,[24] phenol resin,[25] or polysaccharides[26]) in the interstices between beads in silica or polymeric opaline templates and their further removal. Direct carbon opals, on the other hand, have essentially been obtained by tedious double-templating strategies, where (mostly) silica inverse opals are used as templates. Infiltration and further carbonization of phenolic resin[27] or furfuryl alcohol[28] replicates the initial ordered structure. Other strategies to fabricate porous carbon colloidal crystals include the nanocasting method in which a sacrificial mesoporous silica opal is infiltrated with acetonitrile via chemical vapor deposition.[29] Recently, Goodman et al.[8]

L. K. Gil-Herrera, J. A. Pariente, Dr. F. Gallego-Gómez,
Dr. F. Gándara, Dr. Á. Blanco, Prof. C. López
Materials Science Factory
Instituto de Ciencia de Materiales de Madrid (ICMM)
Consejo Superior de Investigaciones Científicas (CSIC)
Calle Sor Juana Inés de la Cruz 3, 28049 Madrid, Spain
E-mail: c.lopez@csic.es
Dr. B. H. Juárez
Departamento de Química-Física Aplicada
Universidad Autónoma de Madrid
Av. Francisco Tomás y Valiente 7, 28049 Madrid, Spain
Dr. B. H. Juárez
Imdea Nanoscience
Faraday 9, 28049 Madrid, Spain

The ORCID identification number(s) for the author(s) of this article can be found under https://doi.org/10.1002/adfm.201703885.

**ADVANCED
SCIENCE NEWS**
www.advancedsciencenews.com

**ADVANCED
FUNCTIONAL
MATERIALS**
www.afm-journal.de

fabricated carbon opals by the assembly of monodisperse starburst carbon spheres.[30] Despite the efforts, the fabrication of high-quality 3D-ordered arrays in areas on the order of at least square centimeters by straightforward means is still a pursuit nowadays.

Here we present a novel, simple procedure for fabrication of ordered periodic porous structures from carbon-based spheres which, upon posterior pyrolysis, yields systems with both small (micro- and meso-) and large (macro-) pores and distinct optical properties associated with their topology and hierarchical porosity. Large-area, high-quality carbon-based opals were obtained by 3D self-assembly of monodisperse hybrid spheres composed of a PS core and a carbon shell (PS@C). These PS@C spheres were synthesized by a hydrothermal method, which provided control over both the core size and the shell thickness.[10] Such versatility of the spheres allowed broad tunability of the optical properties of the resulting PS@C opal. Additionally, by subjecting the opal to pyrolysis, the PS cores are eliminated from the spheres, leading to an opal formed by hierarchically porous hollow@C spheres (hollow@C opal).

Thus, since they comprise a photonic crystal, structural modifications of the spheres, alter the photonic performance in a highly sensitive manner. Importantly, the three different types of pores coexisting in the PS@C opals yield distinct contributions to the optical response, a fact that further serves as a novel means for both the study of microscopic structural characteristics and the tuning of the overall optical response of ordered structures. Interestingly, the impact on optical properties of, for example, gas adsorption or condensation phenomena is drastic in the hollow@C opals as a result of both induced micro- and macroporosity, showing promise as highly sensitive and precise sensors.

2. Results and Discussion

2.1. Opals from Hybrid Carbon Spheres

Highly monodisperse PS@C spheres were obtained by means of a template-assisted hydrothermal glucose polymerization on PS, used as seeds (**Figure 1**a,b). Seeds diameter, together with other experimental parameters (such as temperature, time, etc.), determine the final beads size (in the range from 300 nm to 1.5 µm). Details on this synthesis can be found elsewhere.[10] As depicted in Figure 1c, PS@C spheres were self-assembled in fcc close-packed arrays by a modified vertical deposition procedure (see the Experimental Section) on a glass substrate forming PS@C opals. This technique yields crystal structures with not only high quality but also very large areas (in the range of square centimeters) without deteriorating the final optical properties. Subsequent pyrolysis allows eliminating PS, producing hollow@C opals. This final thermal treatment also induced microporosity in the carbon shell (Figure 1d). As an example, **Figure 2**a shows optical image from an opal fabricated from 590 nm PS@C spheres (470 nm PS core and a 60 nm thick carbon shell). Three digital camera images of the sample taken in different orientations are displayed. This can be used to show, first, that, as mentioned above, large-scale samples are possible using our modified vertical deposition method. And second that, in spite of the inherent absorption of carbon, a
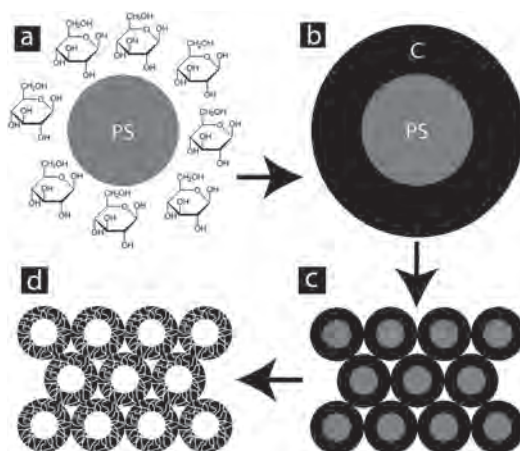

Figure 1. a) PS spheres, used as seeds, and glucose under hydrothermal conditions yield b) PS@C spheres that can be ordered on a substrate forming a c) PS@C artificial opal. d) Finally, pyrolysis can be used to selectively remove the PS cores to form a hollow@C opal.

highly bright (angular dependent) opalescence can be achieved throughout the sample. Actually, as mentioned above, this absorption reduces multiple scattering and enhances the relative reflectivity compared to the background produced by light diffusion.

The fcc crystalline structure of PS@C opals is evidenced in Figure 2b, where a scanning electron microscopy (SEM) image shows a well-ordered array of 770 nm spheres with the [111] planes oriented parallel to the substrate. Domains above $60 \times 60 \ \mu m^2$ were obtained separated by cracks arising from the drying process (not shown). Figure 2c corresponds to an SEM image of the cross section of a 770 nm PS@C opal. To this end, the sample was embedded in a resin and directly cut with a microtome. In this image, the inner core (corresponding to the PS seed) and the overgrown shell (corresponding to carbon) are clearly discernible. It is important to point out that the assembly of the PS@C opal was achieved without any additional process (such as sacrificial scaffold, carbonization, or other intermediate steps usually employed in similar systems,[8,29]) which clearly simplifies the procedure and improves the quality of the final structures.

2.2. Optical Properties of PS@C Opals

PS@C opals show well-defined and high-quality optical properties, as evidenced in **Figure 3**a, where reflectance and transmittance spectra taken at normal incidence are shown. The spectra correspond to a 42 layer thick sample composed of 650 nm PS@C spheres (230 nm PS inner core and 210 nm carbon shell). The first stop band (Bragg peak), where light is strongly attenuated, is centered at around 1600 nm (in reduced units $a/\lambda = 0.57$, where $a = \sqrt{2} \cdot D$, with D the sphere diameter and λ the wavelength). This optical response completely matches that of an artificial opal in the Γ-L reciprocal

**ADVANCED
SCIENCE NEWS**
www.advancedsciencenews.com
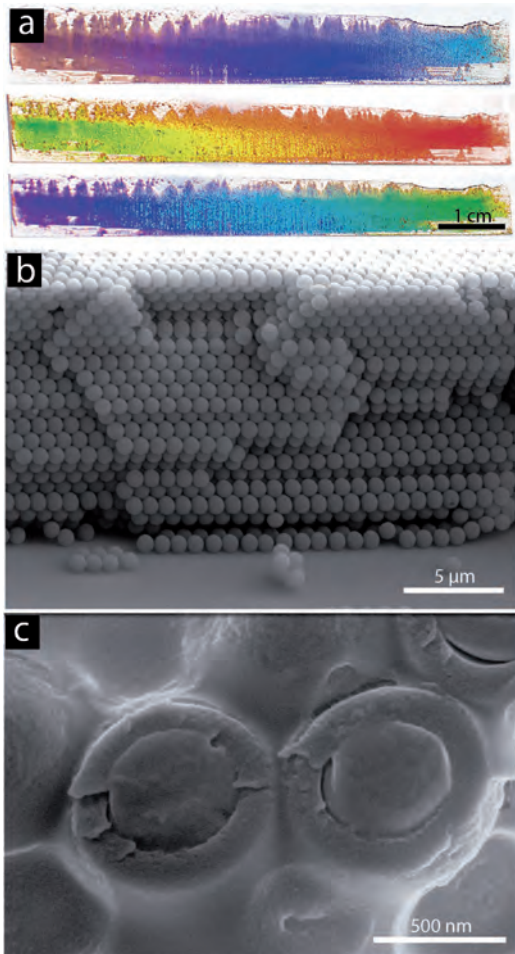
**ADVANCED
FUNCTIONAL
MATERIALS**
www.afm-journal.de

Figure 2. a) Optical photographs of a PS@C opal deposited on a glass substrate, where iridescence (at three different orientations) are clearly observed. b) SEM image of a PS@C opal fabricated from hybrid PS@C spheres. c) Detail of a PS@C opal cross section where the core and shell are clearly discernible. The spheres appear slightly deformed due to the resin, in which the opal was embedded to allow the cut.

Figure 3. a) Normal incidence reflectance and transmittance spectra of a 42 layer thick PS@C opal made of hybrid 645 nm PS@C spheres. b) Reflectance spectra of PS@C opals produced by self-assembly of monodisperse colloidal PS@C spheres covering a broad spectral range. Spectra are color labeled: *Blue* corresponds to samples obtained from PS seeds with D_{PS} = 230 nm with overgrown carbon shells of 45, 125, and 210 nm; *Red* corresponds to samples grown from D_{PS} = 470 nm with 20 and 60 nm shells; *Black* to samples coming from D_{PS} = 520 nm with carbon shells of 110 and 120 nm.

space direction.[31] The high quality of the arrangements can be inferred from the intense optical response recorded in the high-energy region ($a/\lambda \approx 1$), as it involves scattering through eigenmodes different from those associated to the [111]-oriented reciprocal vectors[32] and quickly worsens if lateral order is poor. For these sphere sizes, these high-energy bands lie in the visible range and are responsible for the bright colors observed with the naked eye (as in Figure 2a).

The final optical response of the PS@C opals can be finely tuned across the visible and near-infrared spectral regions by simply modifying the size of the PS@C spheres. Figure 3b shows normal incidence reflectance spectra (normalized)
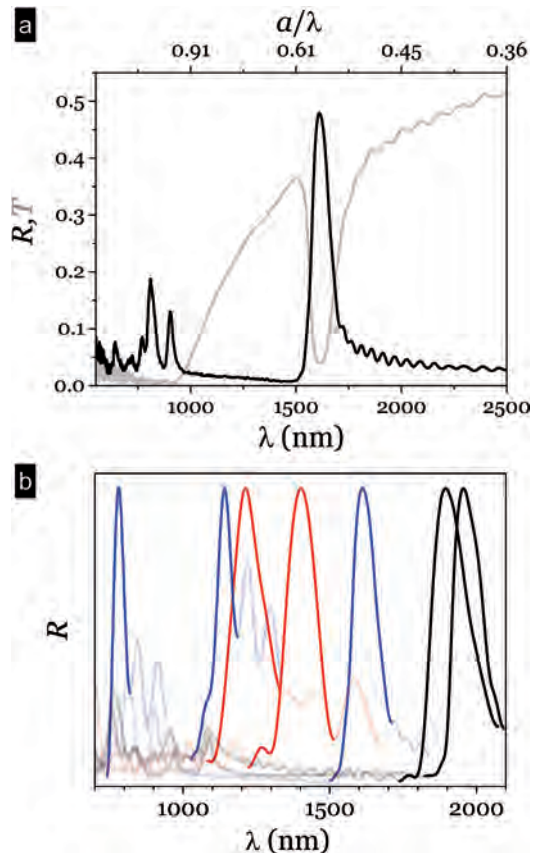
of several PS@C opals grown from different PS seeds (and overall size) showing Bragg peak locations ranging from 760 to 2000 nm.

It is worth mentioning here that the remarkable degree of tunability achieved in this spectral region is a valuable property when versatile templates are needed. In this direction, not only the seed size, D_{PS}, but also the carbon shell thickness, $d_C = (D−D_{PS})/2$ can be tuned to adjust the range of operation. To describe these heterogeneous sphere, a carbon volume fraction parameter, $\gamma = 1 − (D_{PS}/D)$,[3] can be defined which varies from 0 for fully PS sphere to 1 for purely carbon spheres. The shaded area in **Figure 4** shows the theoretical evolution of the pseudogap (center frequency and edges) with γ calculated using the MPB free package.[33] This calculation is straightforward
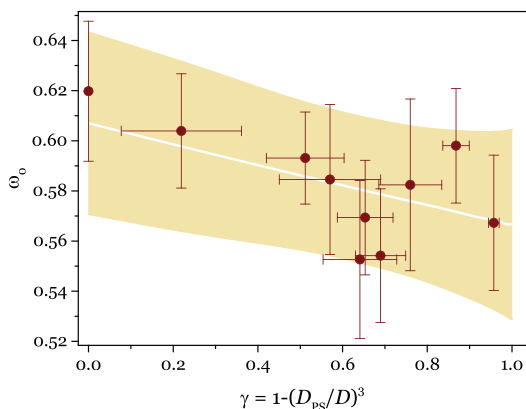
**ADVANCED
SCIENCE NEWS**
www.advancedsciencenews.com

**ADVANCED
FUNCTIONAL
MATERIALS**
www.afm-journal.de

Figure 4. Evolution of the pseudogap of a PS@C opal as a function of the carbon fraction γ. White line and shaded area represent the simulated Bragg peak and its corresponding width (gap edges). Full circles are the experimental measurements. Uncertainty in γ arises from both seed and final sphere sizes and from Bragg peak width.

Figure 5. a) N_2 sorption curves for $D_{SP} = 243$ nm, $d_C = 340$ nm untreated (black symbols) and pyrolyzed spheres at 365 °C (red symbols) and 480 °C (green symbols). Solid and empty symbols represent adsorption and desorption processes, respectively.

when both the geometry and all the refractive indices involved are known. In our case, the refractive index of carbon is the only unknown and had to be considered taking into account the range of values reported in the literature.[34] In order to fit our experimental results (red dots in Figure 4) we used a carbon refractive index value of 1.73 that gave the closest match for the sample with the largest carbon content. The rest of calculations had no free parameters and only the C-fraction, γ, which fully describes the structure, was varied. The agreement is remarkable considering the variety of compositions and sizes included.

2.3. Hierarchically Porous Structures: Hollow@C Opals

The PS@C spheres[10] constituting the crystalline structures studied here are merely subjected to a self-assembly process that has no effect on the material properties. The amount of carbon spheres in the self-assembled form is too small to allow the realization of N_2 physisorption measurements (typically an opal comprising less than 10 mg). The only difference between the original carbon spheres in powder and the opal is the organization (order/disorder) and, consequently, the macroscopic filing fraction. Therefore, we can safely assume that porosity would be the same independent of the spheres arrangement (opal conformation) as far as micro- and mesoporosity are concerned because the material is the same. Opals differ from powders in that the latter have a larger amount of interparticle voids ($\approx$45%) since the former are close-packed (maximum amount of volume occupied by spheres, $\approx$74%). The pores created by the interparticle voids in the opals can be easily estimated by simple geometric arguments and are not subjected to major change upon pyrolysis because the shape of the particles does not change. N_2 adsorption/desorption isotherms[35] (before and after thermal treatment) were obtained from the same PS@C spheres (in powder form) with which the opals used in the optical experiments were made.
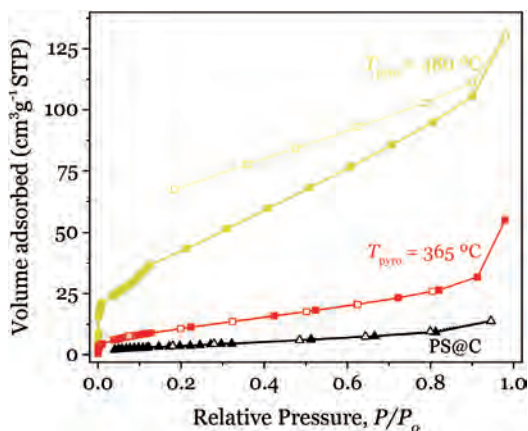
As can be seen in **Figure 5** the as-grown spheres show negligible adsorption. On the other hand, spheres treated at 365 and 480 °C exhibit N_2 sorption isotherm profiles indicative of hierarchically porous structure. The sample treated at 365 °C shows a small amount of N_2 adsorbed in the micropore region, corresponding to a surface area of 43 m^{2}g^{-1} according to the BET model, followed by a gradual increase in the uptake, attributed to adsorption in larger pores of the sample. Increase in the temperature of the thermal treatment results in an increase of the porosity. Thus, the material treated at 480 °C exhibits a larger micropore volume, with a BET surface area of 170 m^{2}g^{-1}. Furthermore, a step is also observed in the adsorption curve at $P/P_0 = 1.5 \times 10^{-3}$, indicative of the presence of micropores with different sizes. This is followed by a gradual increase in the amount of adsorbed nitrogen, with presence of hysteresis in the desorption curve, further confirming the presence of mesopores. These differences in the N_2 physisorption curves between the samples treated at different temperatures are in agreement with the optical response of the corresponding opals, as discussed below.

Ps@C opals were assembled with this material and therefore hollow@C opals can be easily fabricated by a simple pyrolytic postprocessing. Such treatment modifies the original structure and generates a hierarchical pore system without any activation process in three levels, as follows. First, macroporosity is created upon PS core removal during the pyrolysis, so that the resulting opal is solely formed by hollow, nm-thin carbon, spherical shells. Void and shell sizes depend on the specific geometry of the initial PS@C opal. Second, pyrolysis also creates an interconnected microporosity in the amorphous carbon shells, which is concomitant to a moderate shrinkage of the walls thickness ($\approx$15%). This micropore formation is the result of a twofold process that involves both the opening of pores and the restructuring of the carbon network after gasification reactions.[36] Microporosity depends on the pyrolysis procedure, so that both the number and size of pores increase with the

**ADVANCED
SCIENCE NEWS**

www.advancedsciencenews.com

**ADVANCED
FUNCTIONAL
MATERIALS**

www.afm-journal.de

pyrolysis temperature (T_{pyro}). Finally, the mesoporous network of the original opal (interparticle voids) is maintained after pyrolysis. All in all, the obtained hollow@C opal is a hierarchically porous structure exhibiting porosity in three length scales: (i) *micropores* of less than 2 nm created in the carbon shells, (ii) *mesopores* of some tens of nm, which are the interstices between the opal spheres (already present in the hybrid PS@C opals), and (iii) *macropores* of hundreds of nm (the diameter D_{PS} of the seed PS spheres) as the inner air cavity of the carbon shells.[37] Pyrolysis also causes the loss of the oxygen-containing functional groups of the carbon surface, leading to an increment of the aromatic surface character. This chemical modification can play a role in the particles interaction with its environment, like the adsorption of liquids and gases (e.g., water, whose presence must be considered in any opal[38]).

Interestingly, such pore hierarchy is straightforwardly tunable by the aid of choice of seed size and carbon shell thickness,

and the pyrolytic temperature, which underlines the potential of the present methodology. To illustrate this issue, **Figure 6** shows the optical properties of a PS@C opal whose Bragg peak lies at ≈790 nm and those obtained upon pyrolysis at two different temperatures, namely, T_{pyro} = 365 and 480 °C.[39] The large blue-shift of the Bragg peak upon pyrolysis is due to the decrease of the opal average refractive index upon PS elimination (observed at both T_{pyro} employed). While the hollow@C opal show a Bragg peak centered at 690 nm, pyrolysis at higher temperature further shifts the Bragg peak to 620 nm. The larger blue-shift observed at the higher T_{pyro} is consistent with a further developed microporosity. The persistence of the Bragg peak in the hollow@C opals proves that the ordered 3D structure is preserved after pyrolysis, although the decrease in the peak reflectance denotes partial structural degradation caused by cracking. The corresponding transmission electron microscopy (TEM) images (Figure 6b–d) evidence the solid core–shell
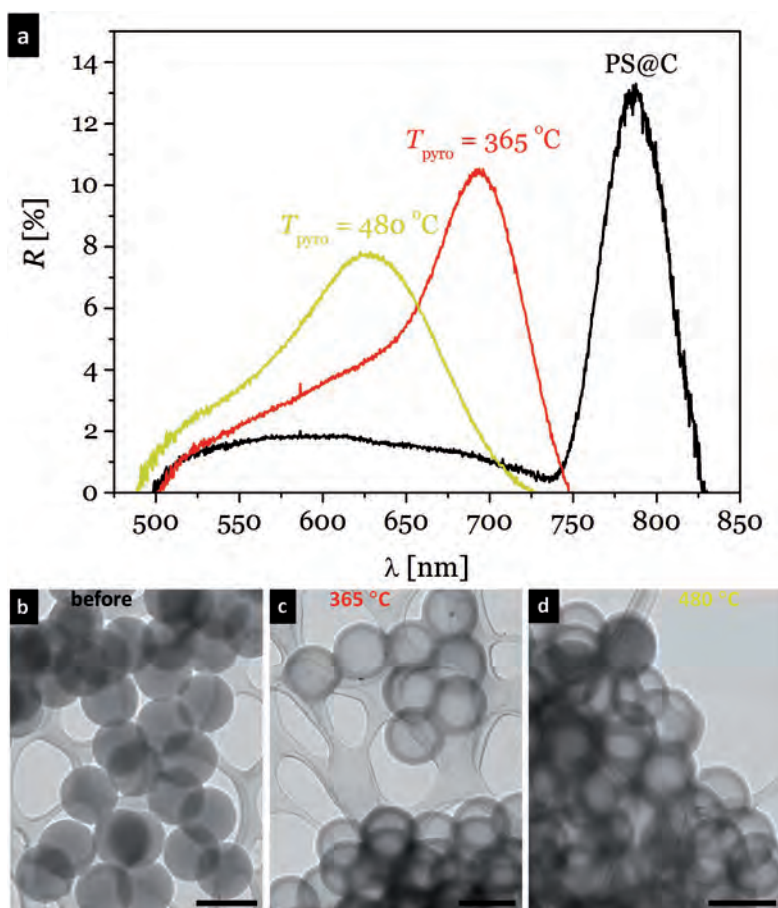

Figure 6. a) Reflectance spectra of a D_{SP} = 230 nm, d_C = 45 nm PS@C opal (black) and hollow@C opals obtained by pyrolysis at T_{pyro} = 365 °C (red) and 480 °C (green). TEM images of b) PS@C spheres and hollow@C spheres obtained by pyrolysis at c) 365 and d) 480 °C. Scale bars are 300 nm.

**ADVANCED
SCIENCE NEWS**
www.advancedsciencenews.com

**ADVANCED
FUNCTIONAL
MATERIALS**
www.afm-journal.de

morphology before pyrolysis and the hollow structure after the thermal treatment.

2.4. Porosity-Dependent Optical Response

Besides the evident change of the opal photonic bands upon pyrolysis, which is additionally tunable by the treatment temperature, we find that both induced micro- and macroporosity drastically affect the optical response of the hollow@C opal to, for example, gas condensation phenomena. Thus, since the opal spheres constitute a photonic arrangement, their structural variation modifies the photonic performance in a highly sensitive manner. Importantly, the three different types of pores coexisting in the hollow@C opal yield distinct optical responses something that can be revealed by adequate experiments, as shown in the following. This fact provides a novel means for inspection and characterization of microscopic structural

features, alternatively to conventional gas sorption isotherms and requiring minute sample amounts.

In order to exploit the control over porosity in the hollow@C opals, we demonstrate one functionality based on the capability to take up water. Their porosity-dependent performance is tested by studying the response to water adsorption in air under different experimental conditions. The abovementioned opals treated at 365 and 480 °C were employed, and compared with the initial PS@C opal. First, we measured the Bragg peak evolution as a function of water in air relative humidity (RH) over a broad range. **Figure 7**a–c shows Bragg peak centers, λ_{Bragg}, as a function of RH in the three paradigmatic cases: prior to pyrolysis and pyrolyzed at two temperatures. The Bragg peak of the original PS@C opal exhibits the largest variation ($\Delta\lambda_{Bragg} \approx 10$ nm), while it clearly diminished in the hollow@C opals ($\Delta\lambda_{Bragg} \approx 5$ and 3 nm, for $T_{pyro} = 365$ and 480 °C, respectively). In addition, the change in the peak reflectance exhibited a similar trend (see normalized ΔR in Figure 7d). In such humidity
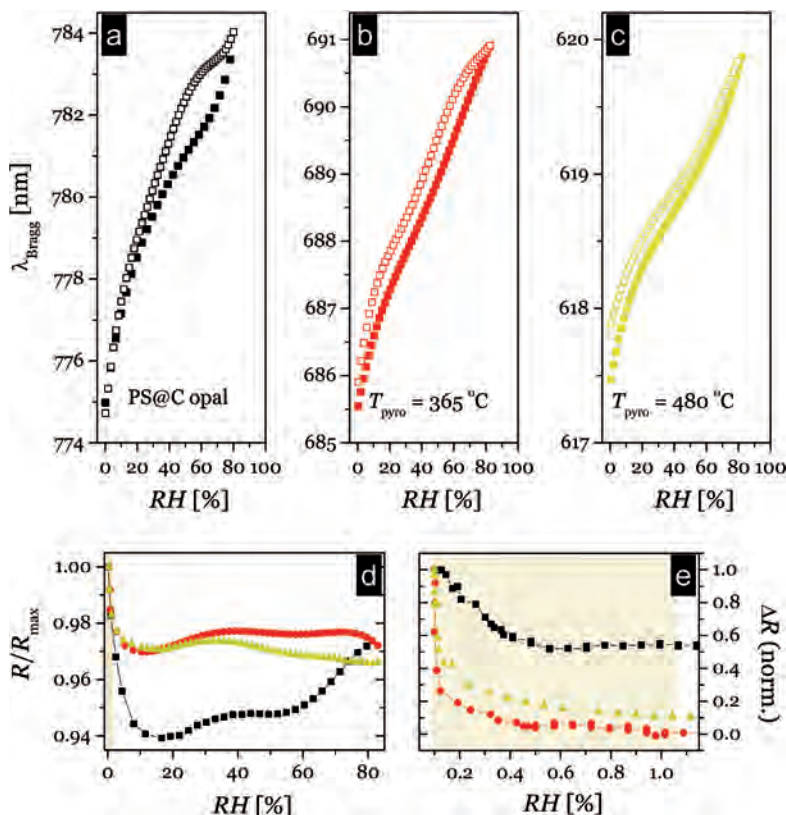

Figure 7. a) Humidity dependence of Bragg peak position on a 320 nm PS@C opal and the corresponding hollow@C opals obtained by pyrolysis at $T_{pyro} =$ b) 365 and c) 480 °C. Increasing (solid symbols) and decreasing humidity (open symbols) scans show varying degrees of hysteresis. d) Reflectance relative to the peak maximum upon increasing RH. e) Evolution of R normalized to its variation range in the full RH region. The region of very low HR is highlighted in (d) and (e).

**ADVANCED
SCIENCE NEWS**
www.advancedsciencenews.com

**ADVANCED
FUNCTIONAL
MATERIALS**
www.afm-journal.de

experiments, in which extreme values are not reached (1% < RH < 80%), the photonic response is mostly due to water adsorption (as molecular mono- and multilayers[40]) in the interstices between spheres, that is, in the mesopores.[41,42] Therefore, the observed behavior is attributable to the significant hydrophilicity of the carbon surface and its progressive hydrophobization upon pyrolysis. Some hysteresis between adsorption and desorption branches was found in all cases (shown in λ_{Bragg}, Figure 7a–c), which diminished following the decrease of the spheres hydrophilicity.

The influence of the microporosity was tested by measuring the response in the low RH region. Figure 7e shows a blow up of the 0.1–1.1% range in Figure 7d, normalized for clarity, to the total variation in each case. The response in this range of RH highlights the differences between as-grown and pyrolyzed structures. On the one hand, the PS@C opal exhibits a moderate response (≈40% reduction) that can be attributed to the incipient formation of water monolayers on the outer surfaces of the C shells. On the other hand, for the hollow@C opals, the reflectance almost completely collapses,[43] which is indicative of the filling of micropores smaller than 1–2 nm.[39] Such modification in the opal response is even clearer in the 365 °C pyrolyzed opal, in which R reaches its minimum at humidities as low as ≈0.5% RH, consistent with smaller pores than in the 480 °C pyrolyzed sample, and in agreement with previous results.[10] The microporosity formed in the hollow@C opals endows them with very high sensitivity in the low-humidity region, which could be useful for humidity sensing in highly dry environments.

Finally, the macropores created by the removal of the PS spheres come into play most obviously when humidity conditions approach saturation (*gas-bulk liquid* coexistence). Such conditions are reached by cooling the sample down close to the dew point, where water vapor massively condenses, even on open surfaces or in large cavities such as the spherical macropores of the hollow@C opals. The effect of such condensation in an opal is best noticed in the Bragg peak reflectance. In the PS@C opal, water can only condense in the mesopores between the spheres (the only pores available), leading to a collapse of the Bragg peak as the refractive index of bulk water approaches that of the PS@C spheres (**Figure 8**a). However, the opposite behavior was observed in the hollow@C opals, in which the Bragg peak reflectance increased near the dew point (Figure 8b). To account for such a dissimilar behavior, the interplay between the effect of filling the inner cavities of the spheres and the mesopores must be considered in the light of the changes in average and contrast of refractive indices that will require a full photonic band calculation. While dew only occupies the mesopores in the PS@C opal, in the hollow@C opal it also fills the macropores (the inner cavities of the spheres). In the former, dew merely leads to a reduction of index contrast (hence the reflectance drop), while, in the latter,
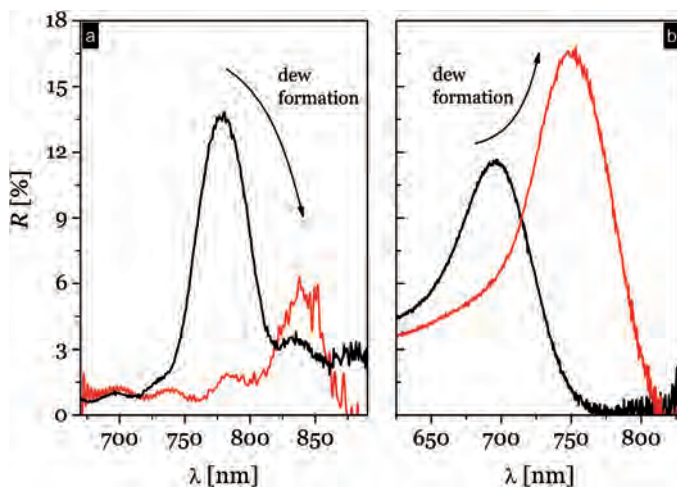

Figure 8. a) Dew point experiments performed on a 320 nm PS@C opal and b) the corresponding hollow@C opal obtained by pyrolysis at T_{pyro} = 480 °C. Black and red spectra were measured at 22.8 and 7 °C, respectively. Air humidity was 36% RH.

the average refractive index of the spheres is greatly increased, which allows for reflectance enhancement. Such behavior also demonstrates that the micropores of the carbon shell enable water diffusion into the cavity. In this way, the response of the opals exhibits a clear-cut distinct behavior upon adsorbate condensation depending on the absence or presence of macropores that widens the possible applications that they enable.

The remarkable sensitivity of the optical properties to the nature of the pore structure in this material system deserves a final observation. Carrying out specific surface area or porosity physisorption measurements typically requires amounts of sample difficult or impossible to obtain when dealing with thin film structures such as carbon (or other material) opals. Even when large-area samples are available just because they are very thin (tens of layers/micrometers) they yield a meager amount, few mg cm^{-2}, in actual samples, clearly insufficient for the experimental techniques to offer any reliable measurement. Nevertheless, this shortcoming only highlights the effectiveness and prowess of the optical techniques employed here that are capable to assess porosity where other techniques fail.

3. Conclusions

High-quality large-size PS@C opals and hollow@C opals have been fabricated through a simple and straightforward methodology based on the self-assembly of monodisperse PS@C spheres. The optical properties of these structures can be modified by the choice of the PS seeds size, the thickness of the C overgrown shell, and the pyrolysis temperature. Further to their obvious optical response these structures are proven sensitive to water condensation phenomena drastically affected by the pores hierarchical nature, whose control opens doors to highly sensitive and precise sensors. Functionality

associated with diverse pore populations revealed as sensitivity to diverse ranges of humidity provided by different size pores. Such sensitivity, reflected in the response of the photonic bandgap, allowed for an original way for inspection of the system structure which turns into an alternative to conventional gas isotherms.

4. Experimental Section

PS@C Preparation: Monodisperse PS@C spheres colloids (size distribution between 2 and 4%) were obtained by a hydrothermal method in which the decomposition of glucose yields an overgrown carbon shell on the surface of PS seeds as reported elsewhere.[10]

Opal Self-Assembly: PS@C opals were fabricated by a modified version of the vertical deposition method[44] and by natural sedimentation. In the latter case, the horizontal position of the substrate (instead of vertical) guarantees the formation of larger domains due to the reduction of the meniscus. For opal fabrication, chromic acid-cleaned substrates (glass or quartz) were placed at a 35° angle in a 50 mL plastic petri dish with 0.1 g colloidal suspension (0.3 wt% in ethanol). The pan was placed in an incubator at ≈45 °C with 20% humidity overnight.

Hollow@C opals were obtained by carbonization by heating of the PS@C opals at 365 or 480 °C during 1–2 h, with a heating rate of 10 °C min^{-1} for 1–2 h under vacuum.

Electron Microscopy Characterization: The morphology and sizes of PS@C and PS@C hybrid spheres and PS@C hybrid opals were evaluated by two SEM: FEI Verios 460L field-emission scanning electron microscope (FESEM) with ultrahigh resolution Schottky emitter and wide array of detectors, and by LEO 145 FESEM (Hitachi S-4700). The size distribution was obtained from the analysis of 100 spheres in each case from images obtained by SEM. For transmission electron microscopy, a JEOL-2000 FXII operating at 200 kV was used.

Spectroscopy: The normal incidence reflectance spectra were collected with a FTIR Bruker IFS 66/S spectrometer coupled to a microscope, which permits a good selection of the test area.

Optical Experiments: The opals photonic bandgap (Bragg peak) was characterized by measuring reflectance with an Ocean 2000 + fiber spectrometer using white light (halogen lamp Osram HLX 64623) at normal incidence.

Humidity experiments were performed by placing the samples in a home-made environmental chamber with controllable RH (monitored by a sensor Sensirion SHT75), which allowed in situ optical characterization through a transparent window. Dew experiments were performed under laboratory atmosphere (22.8 °C and 36% RH) by placing the sample on a thermoelectric Peltier element and cooling it down to dew point (≈7 °C).

Conflict of Interest

The authors declare no conflict of interest.

[1] S. Li, A. Pasc, V. Fierro, A. Celzard, *J. Mater. Chem. A* **2016**, *4*, 12686.
[2] H. Liu, X. Liu, W. Li, X. Guo, Y. Wang, G. Wang, D. Zhao, *Adv. Energy Mater.* **2017**, 1700283, https://doi.org /10.1002/aenm.201700283.
[3] D. Bhattacharjya, M. S. Kim, T. S. Bae, J. S. Yu, *J. Power Sources* **2013**, *244*, 799.
[4] B. Fang, M. Kim, J. H. Kim, J. Yu, *Langmuir* **2008**, *24*, 12068.
[5] D. J. Lipomi, R. V. Martinez, L. Cademartiri, G. M. Whitesides, in *Polymer Science: A Comprehensive Reference*, vol 7 (Eds.: K. Matyjaszewski, M. Möller), Elsevier B.V., **2012**, pp 211–231.
[6] O. J. Schueller, S. T. Brittain, G. M. Whitesides, *Sens. Actuators, A* **1999**, *72*, 125.
[7] Y. Li, G. Duan, G. Liu, W. Cai, *Chem. Soc. Rev.* **2013**, *42*, 3614.
[8] M. D. Goodman, K. A. Arpin, A. Mihi, N. Tatsuda, K. Yano, P. V. Braun, *Adv. Opt. Mater.* **2013**, *1*, 300.
[9] J. Zhao, W. Niu, L. Zhang, H. Cai, M. Han, Y. Yuan, S. Majeed, S. Anjum, G. Xu, *Macromolecules* **2013**, *46*, 140.
[10] L. K. Gil-Herrera, Á. Blanco, B. H. Juárez, C. López, *Small* **2016**, *12*, 4357.
[11] J. Liu, N. P. Wickramaratne, S. Z. Qiao, M. Jaroniec, *Nat. Mater.* **2015**, *14*, 763.
[12] G. Hasegawa, K. Kanamori, K. Nakanishi, T. Hanada, *Chem. Commun.* **2010**, *46*, 8037.
[13] Z. Wang, F. Li, N. S. Ergang, A. Stein, *Chem. Mater.* **2006**, *18*, 5543.
[14] J. F. Galisteo-López, M. Ibisate, R. Sapienza, L. S. Froufe-Pérez, Á. Blanco, C. López, *Adv. Mater.* **2011**, *23*, 30.
[15] J. Hu, X. U. Zou, A. Stein, P. Bühlmann, *Anal. Chem.* **2014**, *86*, 7111.
[16] H. Chen, R. Lou, Y. Chen, L. Chen, J. Lu, Q. Dong, *Drug Delivery* **2017**, *24*, 775.
[17] E. Armstrong, C. O'Dwyer, *J. Mater. Chem. C* **2015**, *3*, 6109.
[18] C. O'Dwyer, *Adv. Mater.* **2016**, *28*, 5681.
[19] F. Gallego-Gómez, V. Morales-Flórez, M. Morales, A. Blanco, C. López, *Adv. Colloid Interface Sci.* **2016**, *234*, 142.
[20] M. W. Perpall, K. Prasanna, U. Perera, J. DiMaio, J. Ballato, S. H. Foulger, D. W. Smith, *Langmuir* **2003**, *19*, 7153.
[21] O. L. Pursiainen, J. J. Baumberg, H. Winkler, B. Viel, P. Spahn, T. Ruhl, *Opt. Express* **2007**, *15*, 9553.
[22] H. Cong, B. Yu, S. Wang, L. Qi, J. Wang, Y. Ma, *Opt. Express* **2013**, *21*, 17831.
[23] C.-F. Lai, Y.-C. Wang, *Crystals* **2016**, *6*, 61.
[24] Y. Isshiki, M. Nakamura, S. Tabata, K. Dokko, M. Watanabe, *Polym. Adv. Technol.* **2011**, *22*, 1254.
[25] A. A. Zakhidov, R. H. Baughman, Z. Iqbal, C. Cui, I. Khayrullin, S. O. Dantas, J. Marti, V. G. Ralchenko, *Science* **1998**, *282*, 897.
[26] Z. Zhou, Q. Yan, F. Su, X. S. Zhao, *J. Mater. Chem.* **2005**, *15*, 2569.
[27] G. Guan, K. Kusakabe, H. Ozono, M. Taneda, M. Uehara, H. Maeda, *J. Mater. Sci.* **2007**, *42*, 10196.
[28] G. J. McIntosh, J. B. Metson, *J. Mater. Sci.* **2016**, *51*, 2573.
[29] Y. Yamada, M. Ishii, T. Nakamura, K. Yano, *Langmuir* **2010**, *26*, 10044.
[30] A partial oxidation of the starburst carbon spheres was required to increase the stability of the suspension by increasing their surface charge. Cracks formation and quality loss occurring during the oxidation step ended up in poor optical properties with low reflectance responses.

**ADVANCED
SCIENCE NEWS**

www.advancedsciencenews.com

**ADVANCED
FUNCTIONAL
MATERIALS**

www.afm-journal.de

[31] P. D. García Fernández, J. F. Galisteo-López, C. López, *Appl. Phys. Lett.* **2005**, *87*, 201109.

[32] C. López, *J. Opt. A: Pure Appl. Opt.* **2006**, *8*, R1.

[33] S. Johnson, J. Joannopoulos, *MIT Photonic-Bands*, http://ab-initio.mit.edu/wiki/index.php/MIT_Photonic_Bands, (Accessed: July 2017).

[34] J. Janzen, *J. Colloid Interface Sci.* **1979**, *69*, 436.

[35] Surface areas were evaluated using the Brunauer–Emmett–Teller (BET) method from nitrogen adsorption–desorption isotherms. The nitrogen adsorption measurements were performed in an Autosrb-1 from Quantachrom Instruments at 77 K in the relative pressure range 10^{-6} to 1 atm. Prior to measurement, the samples were degassed overnight at 120 °C.

[36] M. Inagaki, M. Toyoda, T. Tsumura, *RSC Adv.* **2014**, *4*, 41411.

[37] According to the IUPAC, mesopores are defined as 2–50 nm pores. The interstices in a close packed *fcc*, lattice of spheres of diameter *D* comprise octahedral and tetrahedral symmetry voids capable to inscribe spheres of diameters 0.414*D* and 0.225*D*, respectively. Depending on *D*, these diameters may surpass 50 nm. For the sake of clarity, however, we chose to refer to them as "mesopores" to

[38] F. Gallego-Gómez, A. Blanco, C. López, *Adv. Mater.* **2015**, *27*, 2686.

distinguish them from the few hundred nm sized spherical pores, originating from removed PS seeds, referred to as "macropores".

[39] While PS decomposition temperature is higher we have observed that in most cases pyrolysis at 365 °C all but completely removes the initial seeds.

[40] F. Rouquerol, J. Rouquerol, K. S. W. Sing, P. Llewellyn, G. Maurin, *Adsorption by Powders and Porous Solids: Principles, Methodology and Applications*, 2nd ed., Academic, London **2014**.

[41] F. Gallego-Gómez, A. Blanco, V. Canalejas-Tejero, C. López, *Small* **2011**, *7*, 1838.

[42] F. Gallego-Gómez, A. Blanco, C. López, *J. Phys. Chem. C* **2012**, *116*, 18222.

[43] Owing to limitations in our setup, measuring RH below 0.1% poses a technical problem and more accurate studies would call for a dedicated apparatus.

[44] P. Jiang, J. F. Bertone, K. S. Hwang, V. L. Colvin, *Chem. Mater.* **1999**, *11*, 2132.

1703885 (9 of 9)

Arquitecturas de Silicio

La estructura obtenida, hollow@C con porosidad jerarquizada, es infiltrada con Si vía CVD a 365 °C. La generación de Si, ocurre cuando el disilano (que ha sido condensado en los poros del ópalo mediante N_2 líquido) es descompuesto tras el aumento de la temperatura, generando H_2. Durante este proceso, es posible que la estructura carbonosa siga transformándose, es decir, que los pocos C(O) que queden tras la pirólisis evolucionen aumentando tanto la porosidad como el contenido de C. Por lo tanto, es este escenario en el que ocurre la formación de diferentes estructuras C-Si y Si. Sus diferencias radican, principalmente, en dos aspectos: las condiciones de infiltración y el post-procesamiento de inversión (RIE y/o calcinación). Es importante tener en cuenta que el sistema base, el hollow@C, es una estructura novedosa para este tipo de tratamientos, siendo precisamente en sus diferencias donde se encuentran sus virtudes.

Con el fin de tener un control sobre la estructura se exploraron varias posibilidades tanto en relación con las presiones de infiltrado en el Si-CVD, como con el orden de las etapas (RIE/calcinación). Sin embargo, al ser los materiales carbonosos un sistema de partida poco habitual, los resultados fueron novedosos y muchos de ellos el punto de partida para otros materiales.

Las infiltraciones se realizaron a bajas presiones en comparación con trabajos anteriores, y fueron de 110, 480 y 530 Torr, siendo esta

última la habitual para infiltraciones de Si. Cada presión de Si genera estructuras totalmente diferentes que dependen de la integración del silicio con las CS. De forma general, para presiones altas, 480 Torr, la deposición de silicio es demasiado rápida y como resultado se observa la formación de una capa gruesa en la superficie del ópalo que además de cerrar prematuramente el acceso del disilano al interior empeora sensiblemente la respuesta óptica del sistema. En condiciones controladas, la presencia de esta capa superficial genera modos ópticos de superficie.[65] Por el contrario, a presiones más bajas, la cantidad de Si depositado sobre las esferas y sobre la superficie del ópalo, es muy controlable, preservando y en muchos casos, mejorando hasta un 80 % la respuesta óptica.

Una vez realizadas las infiltraciones es posible eliminar controladamente, si fuese preciso, la capa superficial generada en el proceso mediante el ataque mediante iones reactivos, RIE. Particularmente, el material obtenido es una estructura hibrida de C-Si rodeada de Si. Así, ya sea con la eliminación del C y/o con la apertura de la estructura (RIE) se encontró que los dos tipos de Si existentes —el Si dentro de la corteza microporosa y el que crece fuera de la esfera— se ven afectados de diferente modo, generando toda una gama de arquitecturas C-Si o solo de Si.

La ventaja de usar una plantilla carbonosa radica en su facilidad para ser eliminada, así por medio de una calcinación se descompone el material carbonoso y se obtiene la estructura inversa de Si. Sin embar-

go, en dicha etapa de calcinación y para asegurar que los productos de descomposición carbonosos son expulsados correctamente es necesario la apertura del ópalo infiltrado. Así, los iones reactivos de SF_6/O_2 atacan al Si dejando al descubierto la estructura C-Si siendo esta posteriormente eliminada.

Las estructuras generadas en este proceso son diferentes dependiendo de si el ataque se hace antes o después de la calcinación. De este modo es posible generar 4 tipos de arquitecturas diferentes, dos para cada una de las siguientes rutas: *Ruta 1*: **(calcinación/RIE)** a presiones bajas, las paredes delgadas de silicio poroso facilitan la eliminación de la plantilla, dejando una estructura inversa de Si formada por Si poroso y Si más denso (arquitectura 1). Posteriormente, si esta estructura sufre un ataque RIE, se obtiene una arquitectura inversa con un silicio predominantemente poroso. El ataque RIE ocurre de afuera hacia adentro, lo que implica que primero sea atacado el silicio más denso, y entonces, posiblemente tal estructura sea de Si poroso (arquitectura 2). *Ruta 2:* **(RIE/calcinación)** Durante el RIE, el C (todavía no eliminado) reacciona con el F del SF_6 formando compuestos superficiales del tipo $C-F_x$ o C-O-F-Si (corroborado por XPS) (arquitectura 3). Estos compuestos de carbono, al ser calcinados, producen un colapso en la estructura, lo que significa un encogimiento de las partículas de la primera capa del ópalo (arquitectura 4).

Finalmente, cabe destacar que por este método no solo se generan estructuras muy variadas de Si poroso, sino que su respuesta

fotónica, tanto para la estructura compuesta como para la inversa, es de una alta calidad, dejando picos Bragg con intensidades altas (superiores al 80%). Es muy reseñable, además, que la calidad cristalina se conserva pese a los múltiples tratamientos.

Silicon-Based Photonic Architectures from Hierarchically Porous Carbon Opals

Luz Karime Gil-Herrera, Francisco Gallego-Gómez, Almudena Torres-Pardo, Jose M. González-Calbet, Francisco J. Palomares, Alvaro Blanco, Beatriz H. Juárez, and Cefe López*

Silicon-based materials are needed in cutting-edge technological fields, for which hierarchical porosity and photonic properties help improve performance. In this work, the versatility of several fabrication routes that combine silicon infiltration by chemical vapor deposition (CVD), reactive ion etching (RIE), and carbon calcination, which produce a palette of novel silicon-based material architectures, is demonstrated. Design strategies are discussed and the main features of the processing steps are addressed to provide a variety of new silicon-based materials with high morphological versatility and photonic quality. Three-dimensional hollow carbon opals (HCO) permit control of the porosity of subsequent architectures through the initial silicon infiltration, while open or closed surfaces are achieved primarily as a function of RIE conditions. The composition of derived structures depends on the sequence in which the processes are applied. As a result, pure Si and hybrid C–Si inverse structures can be produced with open or closed spheres in the top layer and with an optional passivation layer. Remarkably, by properly choosing the Si infiltration parameters and the calcination/RIE procedure, final structures are achieved with double-shell spheres.

L. K. Gil-Herrera, Dr. F. Gallego-Gómez, Dr. F. J. Palomares,
Dr. A. Blanco, Prof. C. López
Instituto de Ciencia de Materiales de Madrid (ICMM)
Consejo Superior de Investigaciones Científicas (CSIC)
28049 Madrid, Spain
E-mail: c.lopez@csic.es
Dr. A. Torres-Pardo, Prof. J. M. González-Calbet
Inorganic Chemistry Department
Chemical Sciences Faculty
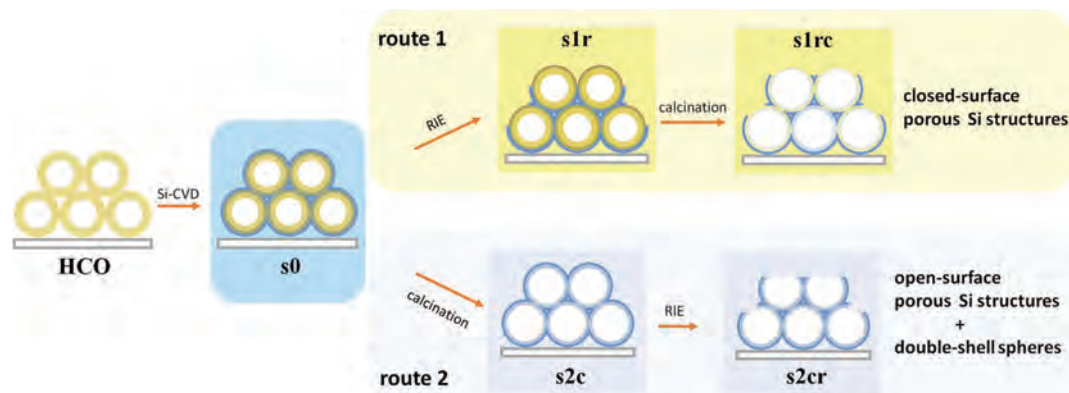Universidad Complutense de Madrid
28040 Madrid, Spain
Dr. A. Torres-Pardo, Prof. J. M. González-Calbet
ICTS National Center for Electronic Microscopy
Universidad Complutense
28040 Madrid, Spain
Dr. B. H. Juárez
Department of Applied Physical Chemistry and Condensed
Matter Physics Center (IFIMAC)
Universidad Autónoma de Madrid
28049 Madrid, Spain
Dr. B. H. Juárez
IMDEA Nanoscience
Universidad Autónoma de Madrid
28049 Madrid, Spain

The ORCID identification number(s) for the author(s) of this article
can be found under https://doi.org/10.1002/ppsc.201900396.

1. Introduction

Hierarchically porous 3D materials with porosity in the micro-, meso-, and macroranges are receiving increasing attention from a wide range of research fields such as energy conversion and storage areas,[1,2] catalysis,[3,4] biomedicine,[5,6] sensors,[7,8] and optics,[9,10] among others.[11,12] The self-assembly of colloidal spheres is a straightforward approach to produce porous 3D structures.[13–15] In particular, hollow colloidal particles provide macroporosity (from their emptied core), and mesoporosity (from the interstices between them). In addition, the shell may allow creation of microporosity and surface functionalization, opening synthetic and functional diversity for such architectures.[16,17] Hollow spheres have also been proposed in the last years in the photonic field for applications such as colloidal lithography,[18] whispering gallery mode resonators,[19] and coating materials for tuning surface reflectivity.[20] Research on colloidal spherical particles has mainly focused on silica, polystyrene or polymethylmethacrylate as building blocks, due to their straightforward fabrication, large availability, and good control of their physicochemical properties.[13] However, the increasing polydispersity of silica spherical particles larger than about 0.5 µm and the lack of thermal, mechanical stability or solvent compatibility of polymeric particles have boosted the exploration of colloidal systems based on different materials.[16,21] Additionally, the fabrication of new multifunctional, high-performance materials can allow a more versatile choice of the composition in order to circumvent the current limitations of the systems available to date. In particular, Si and C are elements with the highest potential concerning cutting-edge technology. On the one hand, Si offers transparency in the near-infrared/infrared regions and high refractive index for light confinement and manipulation in optical sensing and optoelectronic circuits at telecommunication wavelengths.[22,23] On the other hand, C provides high stability upon extreme processing conditions, and carbon spheres exhibit excellent monodispersity and size control.[24,25] It is therefore not only desirable but essential to develop synthetic strategies that integrate hollow particles based on these elements into materials with complex structures.

**ADVANCED
SCIENCE NEWS**
www.advancedsciencenews.com

Particle
& Particle Systems Characterization
www.particle-journal.com

Scheme 1. Schematic of fabrication process of C–Si and Si inverse opal structures based on a carbon photonic system. An HCO is Si-infiltrated to yield a hollow@C–Si composite **s0**. RIE and subsequent calcination processes yield structures s1r and s1rc (route 1). Alternatively, calcination and subsequent RIE processes produce structures s2c and s2cr, respectively (route 2). Yellow and blue colors represent C and Si, respectively. Brown color in s1r denotes CF_x compounds. In route 2, SiO_2 layers remain after RIE, due to anisotropic etching, forming double-shells (see text for details).

In this work, we demonstrate the fabrication of up to five types of hybrid C–Si and pure Si hierarchical structures starting from a 3D ordered template based on hollow carbon spheres, that is, a HCO.[24,26] Its selection as the starting material relies on its advantageous features to generate novel and improved architectures, conveniently combining properties in different areas of application.

i) Hierarchical porosity comprised of uniform, spherical macropores (the empty space inside the spheres), mesopores (the interstices between the spheres), and micropores (induced in the carbon shell by pyrolysis). Additionally, the HCO is a versatile system as it allows broad variation of fabrication parameters, such as the macropore size (from 500 to 900 nm), the shell thickness (from 20 to 210 nm), and the shell microporosity.[24]

ii) Photonic properties arising from the highly ordered fcc crystalline array formed by the spheres showing an intense Bragg peak (the lowest-energy photonic bandgap).[26] This property not only allows applicability in photonics (as a sensitive platform for sensing for instance) but also constitutes a powerful diagnostic tool to follow the changes undergone by the structure along the fabrication process.

iii) Mechanical and thermal properties brought about by the closed-cell skeleton structure of the HCO in which air cavities are isolated, greatly improving robustness and mechanical stability.[27] This characteristic, which contrasts with the interconnected air cavities in the traditionally reported inverse opals, is relevant to endow the template with excellent thermal and mechanical resilience that allows successive processing treatments[28] without compromising the order, quality and stability of the resulting superstructures.

Hybrid C–Si and pure Si hierarchical superstructures were fabricated from HCO by performing a proper combination of three different processing steps: silicon growth by CVD, calcination, and RIE. Our results show the extraordinary variety in the morphology and photonic properties of the resulting

structures by careful selection of the parameters defining each processing step. Indeed, the porosity of the final structure can be tuned through control of the Si CVD deposition inside the voids, while open or closed surfaces can be obtained by selecting the RIE conditions. Furthermore, and according the X-ray photoelectron spectroscopy (XPS) studies, the etching methodology may allow the concomitant fabrication of a passivating layer composed SiO_xF_y, and a fluoropolymer (CF_x), which can be very advantageous in sensing applications requiring selective reactivity.[29,30]

2. Fabrication Strategies

Our starting system, the HCO, can be considered as formed by air spheres surrounded by porous carbon shells (hollow@carbon spheres); since these shells are in contact, the HCO constitutes a closed-cell structure.[27,31] The proposed synthetic procedures involve up to three different steps, constituting two main routes (**Scheme 1**)—see the Supporting Information for the experimental details. In the initial step, common to both routes, Si is incorporated in and around the porous carbon shells by CVD, resulting in a hybrid opal formed by hollow spheres with a C–Si shell (as a result of the infiltration of Si in the C spheres) surrounded by a conformal pure Si layer (structure s0). Following route 1, s0 is subjected to an anisotropic RIE treatment, in order to controllably remove the conformal Si layer (structure s1r) and facilitate carbon removal, if desired, by subsequent calcination (structure s1rc). Because of the presence of C during RIE, a passivating CF_x-rich surface is produced on the s1r shells. This CF_x surface is resilient to and remains after the subsequent calcination, so that s1rc consist of a porous silicon structure with closed surfaces. Alternatively, route 2 is accomplished by swapping these treatments to obtain different structures. Following this route, s0 is calcined in order to directly remove the carbon template, leaving a silicon porous shell and the surrounding Si layer. Thus, the inverse Si opal attained (structure s2c) is made

**ADVANCED
SCIENCE NEWS**
www.advancedsciencenews.com

Particle
& Particle Systems Characterization
www.particle-journal.com

of "dual" walls: microporous—interior face of the shells—and dense—external conformal layer—will be further explained. A subsequent RIE treatment allows removal of the conformal layer and controllable opening of the microporous shell of the top layer, producing a porous silicon structure with open surfaces (structure s2cr). As a remarkable consequence of this route, and choosing adequately the Si infiltration parameters, final structures with double-shell spheres are achieved.

2.1. Silicon Infiltration

The incorporation of Si in the HCO template proceeded via Si-CVD, following a standard methodology.[32] The Si growth is essentially governed by two parameters, namely, the precursor gas (S_2H_6) pressure and the temperature of decomposition. The gas pressure is varied between 110 and 530 Torr (see Section S1 of the Supporting Information for further details). The temperature affects both the Si growth rate and the formation of undesired particles.[33] As we are interested in controlling the amount of Si grown in the opals, low growth rates are required,[34] so we selected a relatively low temperature of 365 °C. **Figure 1** shows the Si-infiltration of the HCO template to generate different s0 structures. The sphere arrangement is preserved, even after massive Si deposition, as confirmed by scanning electron microscopy (SEM) inspection (Figure 1a–d). The CVD working pressure allows easy control of the infiltration
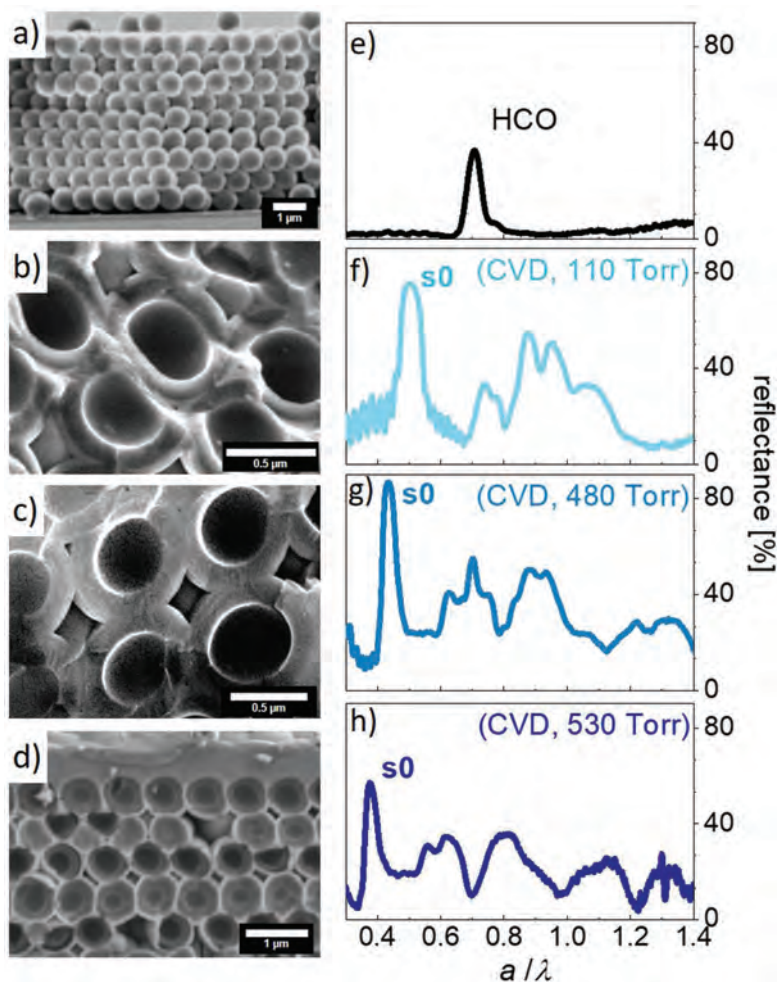

Figure 1. Si infiltration control by CVD. SEM images of a) the starting HCO, b–d) the resulting s0 structures after Si-infiltration at 110, 480, and 530 Torr. The images of s0 are cross-sections of the cleaved opal. e–h) Corresponding optical reflectance. The spectra are taken at normal incidence and expressed versus energy in reduced units (a/λ), where $a = \sqrt{2}D$ is the lattice constant (D is the sphere diameter) and λ is the light wavelength.

**ADVANCED
SCIENCE NEWS**
www.advancedsciencenews.com

Particle
& Particle Systems Characterization
www.particle-journal.com

degree. The photonic response is also tuned and serves the additional purpose of monitoring the degree of Si infiltration of s0 by following its spectral changes (Figure 1e–h). The normal reflectance of the starting HCO template showed a well-defined Bragg peak, demonstrating the initial ordered arrangement. For any infiltration pressure, the Bragg peak shifted toward longer wavelengths (lower energies), as the average refractive index in the photonic structure increases due to the incorporation of silicon—the higher the infiltration pressure, the larger the redshift. Remarkably, and allowed by the increased dielectric contrast in the opal, an outstanding Bragg peak reflectance of 80% and more is achieved after infiltration at low (110 Torr) and medium (480 Torr) pressures (Figure 1f–g). At the highest pressure employed (530 Torr), a Si overlayer is formed on top of the structure (Figure 1h), capable of introducing new optical modes due to surface resonances.[35] Even more, at such pressure, irregular silicon deposits may be found on top of s0, affecting the optical reflectance (e.g., reducing the Bragg peak intensity).

The progressive growth of Si in the multiporous HCO template is not trivial and can be described as follows. Disilane accessibility to the interior of the porous carbon shells is hampered by growth of the outer shell that tends to block the entrance to the pore network. Therefore, the CVD reaction in the C porous shell stalls by exhaustion of disilane. Silicon can continue to grow freely on the outside of the spheres to build a conformal, dense layer enveloping them. The result of this process is sketched in **Figure 2**a. Only for long exposures (>1 h, experiments not shown) or high pressures (>500 Torr), the porous HCO network saturates and a thick, flat silicon overlayer is formed on the top of the sample.

Detailed information about the Si CVD growth process within the C shell is revealed by high-angle annular dark-field (HAADF) imaging, scanning transmission electron microscopy. Figure 2b shows an HAADF image of a hollow@carbon system infiltrated with Si (at 110 Torr), in which several rings with different contrast can be observed. This contrast responds to both varying composition and varying density along with the thickness of each single material in different regions. The corresponding colored energy dispersive X-ray spectroscopy (EDS) mapping (Figure 2b) reveals the presence and location of Si, C, and O in the structure. Figure 2c shows a higher magnification HAADF image evidencing the different contrast areas along the marked line, from which the corresponding intensities of
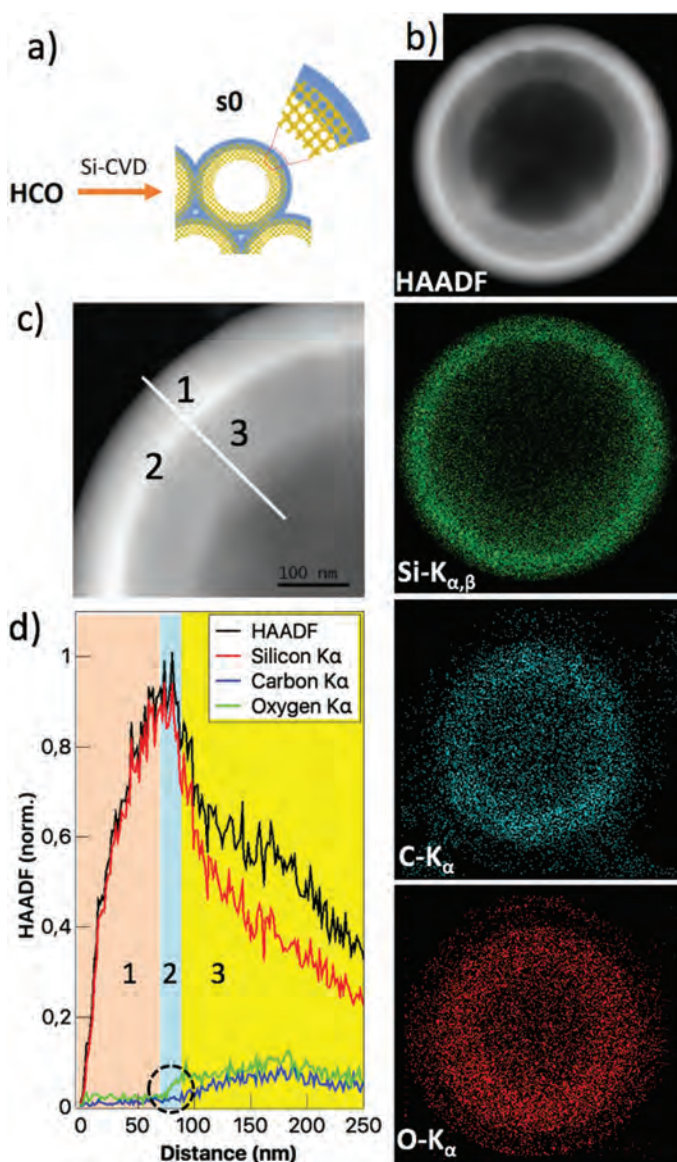

Figure 2. HAADF analysis of s0. a) Scheme of the Si infiltration process through the porous C shells. b) HAADF image and corresponding EDS maps of Si, C, and O. c) HAADF image at higher magnification. d) Intensity variation of the EDS signals along the marked line in (c).

the EDS signals are depicted in Figure 2d (the atomic ratios are listed in Table S1, Supporting Information). This analysis reveals an outermost layer of about 60 nm of the shell (zone 1, pink region in Figure 2d), formed mostly by Si. As the O-Kα map (in red) reveals, a minor amount of O is detectable at the outer shell surface, due to unavoidable oxidation. Beneath this

**ADVANCED
SCIENCE NEWS**
www.advancedsciencenews.com

Particle
& Particle Systems Characterization
www.particle-journal.com

Si-rich layer, a thin brighter interface of about 20 nm is detected in Figure 2c (zone 2, blue region in Figure 2d), where Si and O are the main components, before reaching the C sphere zone. This region, highlighted with a dotted circle in Figure 2d, plays a relevant role in the formation of double shell spheres, as will be further explained. The presence of this Si- and O-rich area prior to the presence of C must be related to the CVD Si growing process on the roughed C surface, rich in O-containing functional groups susceptible to oxidize Si upon deposition, and forming SiO_2. The presence of C is detected at around 80 nm deep from the outer Si surface, establishing the thickness of the grown Si layer. In this region (zone 3, yellow region in Figure 2d) C, O, and Si coexist at different relative ratios from the outer to the inner part of the center of the sphere, according to previously mentioned Si infiltration mechanism sketched in Figure 2a.

In the following, we discuss two routes to generate different silicon structures with a tunable open surface. In particular, we focus on those systems obtained from s0 after Si infiltration at low and medium pressures.

2.2. Route 1: Generation of Closed-Surface Porous Si Structures

As sketched in Scheme 1, route 1 subjects the described structure s0 to anisotropic RIE for controlled removal of exposed areas of the deposited Si, starting from the uppermost layers to achieve a hybrid HCO-Si opal with a tunable conformal layer on the spheres (structures s1r). Both the Si infiltration degree and the RIE exposure time are essential fabrication parameters (**Figure 3**; Figure S1, Supporting Information) to tune the final

structure. For example, RIE etching of a lightly infiltrated s0 sample (at 110 Torr) eliminates the conformal silicon layer after 60 s (structure s1r, Figure 3a), while, for longer exposure times, the surface of the spheres on the top layer are eventually etched open (240 s, structure s1r, Figure 3b). It must be noted that the Si overlayer present in heavily Si-infiltrated samples can be removed using longer RIE exposure times (Figure S2, Supporting Information). Depending on the morphology resulting after RIE, the subsequent calcination yields s1rc structures consisting of hollow@Si spheres with closed (Figure 3c) or open surface shells (Figure 3d). Interestingly, calcination leads to a systematic, significant collapse of the resulting hollow@Si spheres in the upper layer (see Figure 3c,d), while the bulk of the opal conserves the inverse structure (Figure S3, Supporting Information).

Again, apart from many nuances and fine detail that requires numerical modelling to account for, the photonic response lets us follow the structural modifications occurred through the route 1 processing (Figure 3e,f). By comparing with s0, the reflectance spectra of s1r demonstrate a reduction in the Bragg peak intensity—the more, the longer the RIE exposure—which is consistent with a decrease in the average refractive index as Si is gradually removed from the opal. Besides, the features at high energies are strongly reduced probably due to surface roughening. In the calcined s1rc structures, the Bragg peak exhibits, along with reduced intensity, a clear blueshift (higher energy) due to the massive carbon elimination and the consequent decrease of the average refractive index of the porous shell, and widens due to the increase of the dielectric contrast.

The rather unexpected morphology of the top layer spheres in s1r structures might be suspected to be due to material
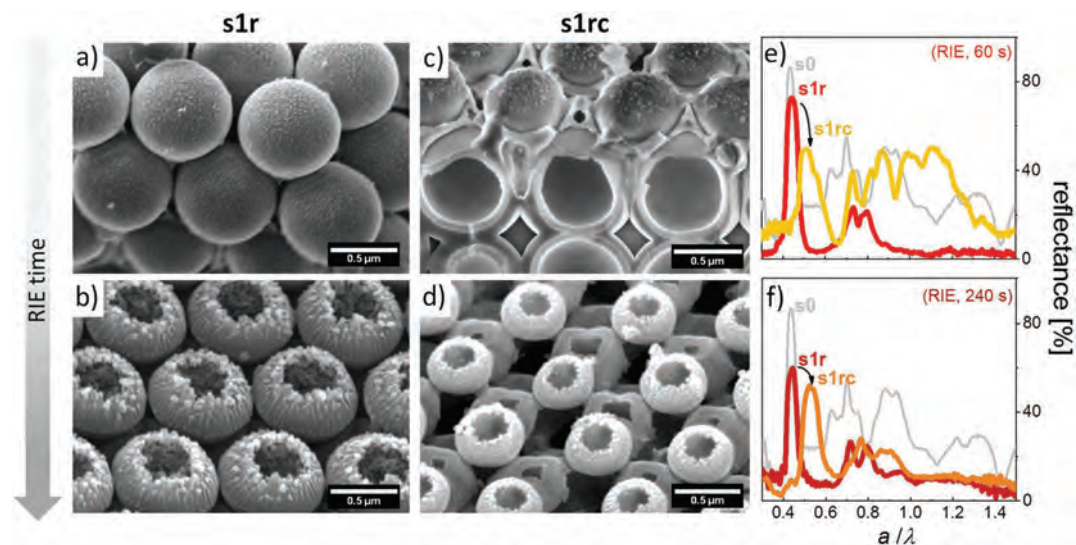

Figure 3. RIE etching and subsequent calcination (route 1) to produce s1r and s1rc structures with close or open surfaces. a,b) SEM images of s1r structures after RIE time of a) 60 and b) 240 s. The initial s0 structure was Si-infiltrated at 110 Torr. c,d) s1rc structures obtained after calcination of s1r structures previously infiltrated with Si at 480 Torr. SEM scale bars are 0.5 μm. e,f) Compared optical reflectance, at normal incidence, of the structures obtained throughout the route 1.
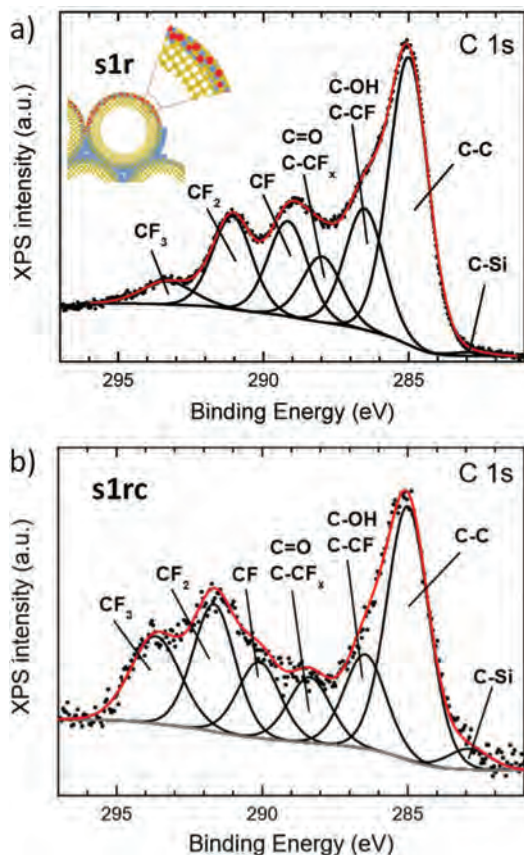
**ADVANCED
SCIENCE NEWS**
www.advancedsciencenews.com

Particle
& Particle Systems Characterization
www.particle-journal.com

Figure 4. XPS characterization (route 1). Deconvolution of C1s XPS spectra of a) s1r and b) s1rc. Si-infiltration of s0 at 110 Torr, RIE exposure time was 60 s. Inset in (a): sketch of the location of the species produced during RIE.

changes induced by the RIE process. In order to obtain a deeper insight, a careful XPS characterization was performed. **Figure 4** depicts the complex line shape of C1s spectrum obtained from structures s1r and s1rc, respectively. Peak assignment is based on binding energy values in comparison with those reported for a given chemical state.[36] Full dots represent experimental data in the spectrum while solid lines represent Shirley background and component peaks. The fitting curve (red line) resulted from the sum of the several contributions belonging to: C−C, C−H, C−OH carbonyl groups, O−C−O carbonyl, and C−CF$_x$, O−C=O carboxylic and C−F, CF$_2$, and CF$_3$ groups. Thus, since RIE involves the use of SF$_6$ and O$_2$ gasses, a new set of C−F chemical species are formed during the etching (sketch in Figure 4a); note, however, that the largest contribution is represented by the C−C species. In addition, the analysis of F1s spectrum reveals the existence of two components, a main one being ascribed to CF$_x$ groups in agreement to previous C1s results and a small contribution coming from Si−F chemical

environment. The binding energy values of these signals are in accordance with values reported.[36] On the other hand, the deconvolution of Si2p core level also confirms the majority presence of SiO$_x$F$_y$ compounds together with weak signals of SiO$_x$ and SiC. Both the intensity and binding energy shift of the main component with respect to the SiO$_x$ emission[36] indicate that the outermost passivation layer is mostly composed of SiO$_x$F$_y$ (Figure S4, Supporting Information).

It is then clear that the fluorinated precursor SF$_6$/O$_2$ reacts with both C and Si during RIE and builds a CF$_x$/SiO$_x$F$_y$ passivation layer. Interestingly, Figure 4b evidences that the CF$_x$ species are still present in the calcined s1rc structure and, additionally, that a new small contribution related to C–Si is formed. The persistence of CF$_x$ in s1rc is not surprising, since it is known that fluoropolymers are extremely inert and resistant. The relative contents of Si, C, O, and F (Table S2, Supporting Information) show that the main loss upon calcination is related to C and F (free F, not forming part of the CF$_x$ compounds that, although in a different proportion, are still present in the final structure). Thus, the observed sphere shrinkage, which is more obvious in the top layer, may be related to the decreased content of C and F in the final s1rc structure.

2.3. Route 2: Generation of Open-Surface Porous Si Structures

Alternatively to route 1, a route 2 can be chosen (see Scheme 1), in which the s0 structure is first calcined to remove C and obtain a purely Si inverse opal (structure s2c). SEM inspection of s2c (**Figure 5**a) already suggests the elimination of C shell upon calcination. In fact, the image shows small windows that connect adjacent spheres upon calcination, indicating an interconnected network of air spheres surrounded by silicon shells, that is, a well-known silicon inverse opal. Carbon removal is confirmed, on the one hand, by HRTEM, including HAADF images and EDS mapping of a s1c structure (Figure S5, Supporting Information), and, on the other hand, by XPS (less than 4% of C remaining). The structure may be further tailored by the RIE process to open the Si surfaces (s2cr structures). The final morphology of these open–shell Si structures depends on both the Si infiltration degree and the extent of the etching procedure (Figure 5b,c after 30 and 60 s RIE, respectively). In structures with a low Si infiltration, the RIE process eventually leads to a grating-like geometry, in which the structure, thinner regions wiped out by the effect of the etching, clearly exhibits well-exposed windows interconnecting the silicon shells interiors (Figure 5c). The opening of these windows (hence their diameter) is ultimately determined by the RIE exposure time.

Once again, a good photonic response allows tracing the structural modifications occurred through route 2 (Figure 5d–f). Compared to s0, the Bragg peak of s2c shows a blueshift (larger energies) and a reflectance decrease, in agreement with the decreased average refractive index in the structure upon carbon removal. After RIE, the position of the Bragg peak in s2cr remains unaffected, while the features in the high-energy range decrease (as observed in Figure 3) probably with the surface modifications.

**ADVANCED
SCIENCE NEWS**
www.advancedsciencenews.com

Particle
& Particle Systems Characterization
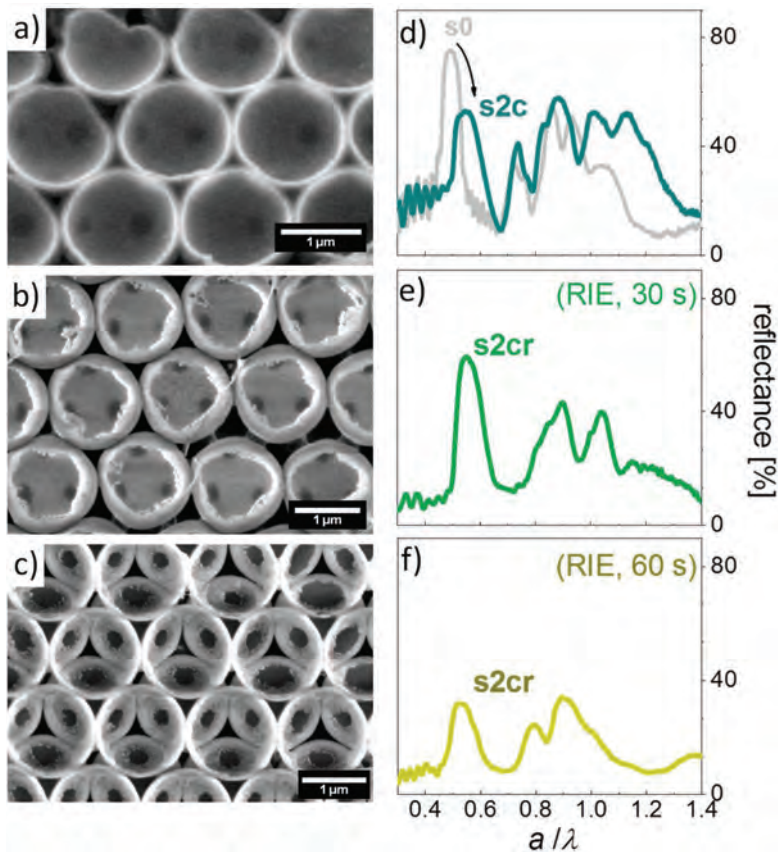www.particle-journal.com

Figure 5. Carbon calcination and subsequent RIE etching (route 2). SEM images of a) s2c and b,c) s2cr samples after RIE treatment during 30 and 60 s, respectively. SEM scale bars are 0.5 μm. d–f) Compared optical reflectance at normal incidence of the structures obtained throughout the route 2. The initial s0 structure was Si-infiltrated at 110 Torr.

Interestingly, the resulting s2cr structures may exhibit double Si shells (**Figure 6**a,b). This double shell is associated with the etching process across the structure containing different layer thicknesses, compositions, and density and the result of different etching rate of silicon and silica when using SF_6.[37] The suggested etching mechanism is depicted in Figure 6c, that summarizes the whole progress from s0 to s2r structures. In this process, anisotropic RIE etching from the top layer attacks through the thin native SiO_2 passivating layer, and gradually eliminates the dense Si shell from the top downward. This etching proceeds at a different rate than that across the 20 nm interface SiO_2 layer previously explained in Figure 2. This effect is well observed in Figure 6c,d, showing evidences of the removal of dense Si prior to the removal of the part near the center of the spheres (the SiO_2 interface). Notice, besides, that those rates may also vary during etching, since, as previously mentioned and according to XPS (Figure S4, Supporting Information), new SiO_xF_y and F–Si species can be dynamically formed.

3. Conclusions

In this work we present fabrication routes that, applied to Si infiltrated hierarchically porous C self-assembled colloidal crystals (hollow@C opal), lead to several silicon-based photonic architectures. These processes rely on the combination of Si CVD, RIE, and calcination steps. The sequence of processes performed and their governing parameters were decisive for the morphological and optical properties of the final structures. Therefore, the selection of the fabrication route and control of the applied parameters directly provide a rich palette of superstructures with easy tunability. Thus, the calcination and subsequent RIE of a previously Si infiltrated sample yields a solid silicon inverse structure that could be finely tailored through the whole thickness, with a double Si shell. The generation of original double-shell Si inverse opals was demonstrated by choosing specific fabrication conditions and process sequence, which involves a complex interplay between RIE and the structure, for which a mechanism
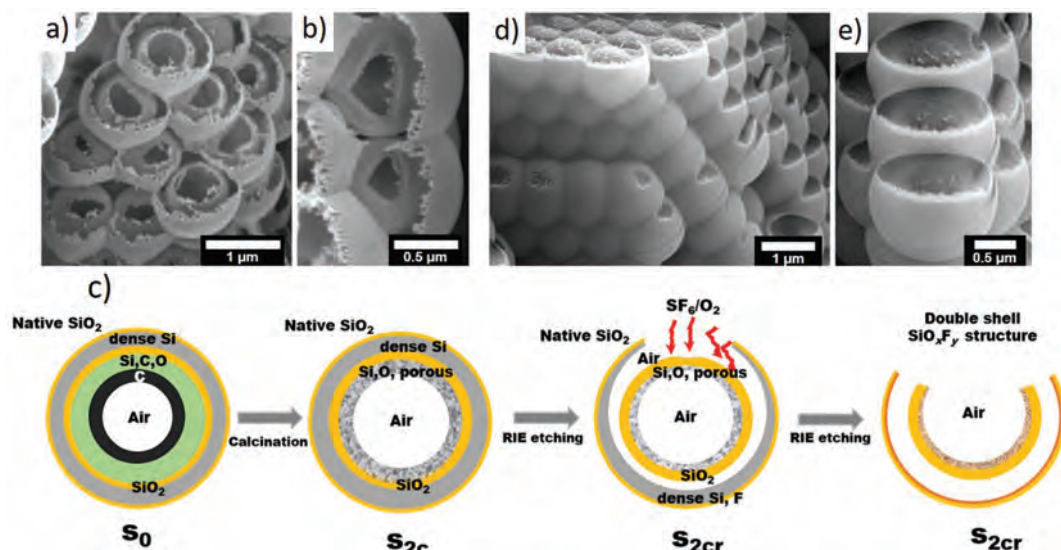
**ADVANCED
SCIENCE NEWS**
www.advancedsciencenews.com

Particle
& Particle Systems Characterization
www.particle-journal.com

Figure 6. Generation of double Si shells. a,b) SEM images at different magnifications of s2cr samples. c) Sketch of the proposed mechanism explaining the generation of double-shell Si spheres upon RIE etching. d,e) SEM images at different magnifications of s2cr samples evidencing the different etching rate of the RIE process across the structure.

is proposed. Alternatively, the application of RIE prior to the calcination led to inverse structures with a closed top layer of shrunk spheres, whose composition included fluoropolymers. Importantly, such shrinkage did not compromise the opal stability, keeping the order and its optical response in the bulk structure. This study highlights the wide range of possibilities offered by general self-assembly-templating techniques in materials science.

Supporting Information

Supporting Information is available from the Wiley Online Library or from the author.

Conflict of Interest

The authors declare no conflict of interest.

[1] Z. Li, K. Zhang, M.-Y. Li, C.-L. Liu, W.-S. Dong, *J. Porous Mater.* **2018**, *25*, 1047.
[2] S. Rehman, S. Guo, Y. Hou, *Adv. Mater.* **2016**, *28*, 3167.
[3] G. Collins, E. Armstrong, D. McNulty, S. O'Hanlon, H. Geaney, C. O'Dwyer, *Sci. Technol. Adv. Mater.* **2016**, *17*, 563.
[4] L. Yu, H. Bin Wu, X. W. D. Lou, *Acc. Chem. Res.* **2017**, *50*, 293.
[5] S. Jung, J. L. Kaar, M. P. Stoykovich, *Mol. Syst. Des. Eng.* **2016**, *1*, 225.
[6] Y. Si, M. Chen, L. Wu, *Chem. Soc. Rev.* **2016**, *45*, 690.
[7] J. Kuang, L. Liu, Y. Gao, D. Zhou, Z. Chen, B. Han, Z. Zhang, *Nanoscale* **2013**, *5*, 12171.
[8] F. Gallego-Gómez, M. Morales, M. A. Blanco, C. López, *Adv. Mater. Technol.* **2019**, *4*, 1800493.
[9] F. Gallego-Gómez, M. Ibisate, D. Golmayo, F. J. Palomares, M. Herrera, J. Hernández, S. I. Molina, A. Blanco, C. López, *Adv. Mater.* **2011**, *23*, 5219.
[10] K. Kitano, K. Suzuki, K. Ishizaki, S. Noda, *Phys. Rev. B* **2015**, *91*, 155308.
[11] X.-Y. Yang, L.-H. Chen, Y. Li, J. C. Rooke, C. Sanchez, B.-L. Su, *Chem. Soc. Rev.* **2017**, *46*, 481.
[12] X. Y. Yang, A. Léonard, A. Lemaire, G. Tian, B. L. Su, *Chem. Commun.* **2011**, *47*, 2763.
[13] J. F. Galisteo-López, M. Ibisate, R. Sapienza, L. S. Froufe-Pérez, Á. Blanco, C. López, *Adv. Mater.* **2011**, *23*, 30.

[14] G. von Freymann, V. Kitaev, B. V. Lotsch, G. A. Ozin, *Chem. Soc. Rev.* **2013**, *42*, 2528.

[15] C. I. Aguirre, E. Reguera, A. Stein, *Adv. Funct. Mater.* **2010**, *20*, 2565.

[16] S. Li, A. Pasc, V. Fierro, A. Celzard, *J. Mater. Chem. A* **2016**, *4*, 12686.

[17] C. Dai, A. Zhang, J. Li, K. Hou, M. Liu, C. Song, X. Guo, *Chem. Commun.* **2014**, *50*, 4846.

[18] K. Zhong, J. Li, S. Van Cleuvenbergen, K. Clays, *Nanoscale* **2016**, *8*, 15845.

[19] S. Yang, Y. Wang, H. D. Sun, *Adv. Opt. Mater.* **2015**, *3*, 1136.

[20] Z. Xing, S. W. Tay, Y. H. Ng, L. Hong, *ACS Appl. Mater. Interfaces* **2017**, *9*, 15103.

[21] Z. Xue, P. Wang, A. Peng, T. Wang, *Adv. Mater.* **2018**, *1801441*, 1801441.

[22] G. Roelkens, A. Abassi, P. Cardile, U. Dave, A. De Groote, Y. De Koninck, S. Dhoore, X. Fu, A. Gassenq, N. Hattasan, Q. S. Huang, S. Kumari, S. Keyvaninia, B. Kuyken, L. Y. Li, P. Mechet, M. Muneeb, D. Sanchez, H. F. Shao, T. Spuesens, A. Z. Subramanian, S. Uvin, M. Tassaert, K. Van Gasse, J. Verbist, R. J. Wang, Z. C. Wang, J. Zhang, J. Van Campenhout, X. Yin, J. Bauwelinck, G. Morthier, R. Baets, D. Van Thourhout, *Photonics* **2015**, *2*, 969.

[23] A. Rahim, T. Spuesens, R. Baets, W. Bogaerts, *Proc. IEEE* **2018**, *106*, 2313.

[24] L. K. Gil-Herrera, Á. Blanco, B. H. Juárez, C. López, *Small* **2016**, *12*, 4357.

[25] M. D. Goodman, K. A. Arpin, A. Mihi, N. Tatsuda, K. Yano, P. V. Braun, *Adv. Opt. Mater.* **2013**, *1*, 300.

[26] L. K. Gil-Herrera, J. A. Pariente, F. Gallego-Gómez, F. Gándara, B. H. Juárez, Á. Blanco, C. López, *Adv. Funct. Mater.* **2018**, *28*, 1703885.

[27] X. Chen, L. Wang, Y. Wen, Y. Zhang, J. Wang, Y. Song, L. Jiang, D. Zhu, *J. Mater. Chem.* **2008**, *18*, 2262.

[28] Y. Zhang, J. Wang, Y. Huang, Y. Song, L. Jiang, *J. Mater. Chem.* **2011**, *21*, 14113.

[29] G. T. Dobbs, B. Balu, C. Young, C. Kranz, D. W. Hess, B. Mizaikoff, *Anal. Chem.* **2007**, *79*, 9566.

[30] V. Singh, P. T. Lin, N. Patel, H. Lin, L. Li, Y. Zou, F. Deng, C. Ni, J. Hu, J. Giammarco, A. P. Soliani, B. Zdyrko, I. Luzinov, S. Novak, J. Novak, P. Wachtel, S. Danto, J. D. Musgraves, K. Richardson, L. C. Kimerling, A. M. Agarwal, *Sci. Technol. Adv. Mater.* **2014**, *15*, 014603.

[31] G. Guan, K. Kusakabe, H. Ozono, M. Taneda, M. Uehara, H. Maeda, *J. Mater. Sci.* **2007**, *42*, 10196.

[32] Á. Blanco, E. Chomski, S. Grabtchak, M. Ibisate, S. John, S. W. Leonard, C. Lopez, F. Meseguer, H. Miguez, J. P. Mondia, G. A. Ozin, O. Toader, H. M. van Driel, *Nature* **2000**, *405*, 437.

[33] R. Fenollosa, M. Garín, F. Meseguer, *Phys. Rev. B* **2016**, *93*, 235307.

[34] F. García-Santamaría, M. Ibisate, I. Rodríguez, F. Meseguer, C. López, *Adv. Mater.* **2003**, *15*, 788.

[35] F. García-Santamaría, E. C. Nelson, P. V. Braun, *Phys. Rev. B* **2007**, *76*, 0751321.

[36] J. Pereira, L. E. Pichon, R. Dussart, C. Cardinaud, C. Y. Duluard, E. H. Oubensaid, P. Lefaucheux, M. Boufnichel, P. Ranson, *Appl. Phys. Lett.* **2009**, *94*, 071501.

[37] R. d'Agostino, D. L. Flamm, *J. Appl. Phys.* **1981**, *52*, 162.

1900396 (9 of 9)

Particle

& Particle Systems Characterization

Supporting Information

Silicon-Based Photonic Architectures from Hierarchically Porous Carbon Opals

Luz Karime Gil-Herrera, Francisco Gallego-Gómez, Almudena Torres-Pardo, Jose M. González-Calbet, Francisco J. Palomares, Alvaro Blanco, Beatriz H. Juárez, and Cefe López*

Silicon-based photonic architectures from hierarchically porous carbon opals

Luz Karime Gil-Herrera,[a] Francisco Gallego-Gómez,[a] Almudena Torres-Pardo,[b,c] Jose M. González-Calbet,[b,c] Francisco J. Palomares,[a] Alvaro Blanco,[a] Beatriz H Juárez,[d,e] Cefe López[a]*

[a]Instituto de Ciencia de Materiales de Madrid (ICMM); Consejo Superior de Investigaciones Científicas (CSIC)

[b]Inorganic Chemistry department, Chemical Sciences Faculty, Universidad Complutense de Madrid, 28040, Madrid, Spain.

[c]ICTS National Center for Electronic Microscopy, Universidad Complutense, 28040, Madrid, Spain.

[d]Department of Applied Physical Chemistry and Condensed Matter Physics Center (IFIMAC), Universidad Autónoma de Madrid 28049 Madrid, Spain

[e]IMDEA Nanoscience, Universidad Autónoma de Madrid, 28049 Madrid, Spain

S1. Experimental Details:

Carbon spheres synthesis

Monodisperse colloidal hybrid carbon spheres (size distribution between 2 and 4%) were obtained by a hydrothermal method in which glucose was used as a carbon precursor and polystyrene (PS) as a seed; thereby, the decomposition of glucose yields an overgrown carbon shell on the surface of PS seeds as reported elsewhere.[1]

In a typical procedure, glucose was dissolved in deionized water to prepare glucose solutions with concentrations ranging from 0.1 to 1.7 mol L^{-1} and PS aqueous suspensions were added. These solutions were transferred into a 40 mL Teflon-lined stainless steel autoclave and subjected to 160-200 °C for 6-20 h. The Teflon vessel was filled to 80% of its maximum capacity. After the HTC reaction, the autoclave was cooled down to room temperature. The dark solid obtained was thoroughly isolated by three cycles of centrifugation/sonication in deionized water, followed by similar cycles in ethanol, and dried overnight at 80 °C.

Table S1 data summarize PS@C hybrid sizes, shell thickness size, temperature and employed glucose concentration.

Particle Size (nm)	PS size (nm)	Glucose concentration (M)	Time (h)	Temperature (°C)	Shell thickness (nm)
650 ± 30 (5 %)	225 ± 12 (5%)	1.9	10	160	210
750 ± 30 (3 %)	543 ± 14 (3%)	1.5	8	160	105
790 ± 20 (3 %)	543 ± 14 (3%)	0.35	6	180	125

HCO fabrication

The colloidal hybrid carbon spheres were self-assembled to produce an opal template. The carbon opals were fabricated by a modified version of the vertical deposition method. Chromic acid-cleaned substrates (glass or quartz) were placed at a 35° angle in a 50 mL plastic petri dish with 0.1 g colloidal suspension (0.3 wt% in ethanol). The pan was placed in an incubator at ≈45 °C with 20% relative humidity overnight.

The hollow@C opal (HCO) template was obtained by carbonization: the hybrid carbon opals were heated in vacuum at 480 °C during 1 h with a heating rate of 10 °C min^{-1}. In order to minimize the formation of cracks, the resulting hierarchically porous photonic structure was kept in vacuum, at room temperature, until the subsequent Si infiltration step.

A number of different HCO templates were employed along this work: inner sphere diameter from 220 to 540 nm, carbon shell thickness from 100 to 200 nm. Further details of the opal and hollow opal template fabrication are described in Reference 2.

Si chemical vapour deposition (CVD) infiltration

The HCO template was placed in a cell where disilane (Si_2H_6), used as a precursor gas, was condensed with liquid nitrogen so that no gas remained in the rest of the line. Disilane is explosive in the presence of oxygen and for this reason, the entire system is previously subjected to a high vacuum ($3x10^{-6}$ Torr). Once the precursor gas has condensed, the cell is isolated and placed in a furnace at 365 °C to produce amorphous silicon and hydrogen. As a precaution, and to rid the cell form disilane, before removing the sample from possible traces of gas it was evacuated again with liquid nitrogen to an auxiliary ampoule. The amount of Si infiltrated was controlled by adjusting the chamber pressure between 110 and 530 Torr; the higher the pressure, the more Si infiltrated. The infiltration time was set at 1 h. After the Si infiltration, the HCO-Si was very gently cleaned with acetone to remove any excess silica that might have been produced.

Special care was taken during disilane manipulation for safety reasons. The whole process was carried out in controlled environment. The CVD line is designed with check valves to prevent gas return and all safety measures to prevent accidental gas leaks.

Reactive ion etching (RIE) was performed using a flow of 50 sccm (gasses SF_6 and O_2) at a pressure of 75 mTorr, a power of 150 W and a variable exposition time between 30 and 600 s.

Calcination process

The carbon from the HCO-Si structure was selectively removed by calcination at 500 °C for 12 h in air with a heating rate of 10 °C min^{-1}.

S2. Characterization

Optical Characterization

Normal incidence reflectance spectra were collected with an FTIR Bruker IFS 66VS spectrometer coupled to a microscope, which permits accurate selection of the test area.

Scanning Electron Microscopy (SEM)

The samples morphology was evaluated by three SEM equipments:

- FEI NovaNano SEM 230 scanning electron microscope. No metallic coating.
- FEI Verios 460L field-emission scanning electron microscope (FESEM) with ultrahigh resolution Schottky emitter and wide array of detectors. No metallic coating.
- 145 FESEM (Hitachi S-4700). Standard metallic coating.

HAADF-STEM imaging and EDS mapping

High-angle annular dark-field imaging, scanning transmission electron microscopy (STEM-HAADF) and energy dispersive X-ray spectroscopy (EDS) characterization was performed on a JEOL JEM ARM200cF electron microscope (Cold Emission Gun) operating at 80 kV provided with a spherical aberration corrector in probe (current emission density $\sim 0.7 \times 10^{-12}$ A/cm^2 and probe size ~ 0.08 nm). STEM-HAADF images were acquired using inner and outer collection semiangles of 68 and 280 mrad, respectively, with a nominal camera length of 60 mm. Compositional mapping was achieved through EDS measurements using an Oxford INCA-350 detector.

X-Ray Photoelectron Spectroscopy

X-ray photoelectron spectroscopy (XPS) was used to characterize the surface chemistry of the samples. XPS spectra were acquired at normal emission in an ultra-high vacuum chamber with a base pressure of 10^{-10} mbar equipped with a hemispherical electron energy analyzer (SPECS Phoibos 150 spectrometer) and a 2D delay-line detector, using a Mg Al-Kα (1253.6 eV) x-ray source. All samples were measured in the same conditions. The overall surface composition was determined from individual element regions detected in the survey spectra recorded using an energy step of 0.05 eV and a pass-energy of 20 eV. Emission from F1s, O1s, C1s and Si2p core levels is detected, with different peak intensities depending on each preparation process. The integral peak areas for each element, after background subtraction and normalization using sensitivity factors provided by electron energy analyzer manufacturer, were used to calculate the atomic concentration of the samples. Data processing was performed using CasaXPS software (Casa Software Ltd., Cheshire, UK).

In addition, for detailed XPS lineshape analysis high-resolution F1s, O1s, C1s and Si2p core-level peaks were recorded by using an energy step of 0.025 eV and a pass-energy of 10 eV. XPS spectra fitting was done by the deconvolution of several mixed percentage of Gaussian-Lorentzian symmetric functions keeping the FWHM and the Gausian/Lorentzian ratio constant. The energy of the peaks and their relative heights were determined by a least-squares method to account for the emission ascribed to the different chemical environment of a given atom according to the binding energy values reported.[3]

S3. *Experimental Results: Additional Data*

Si-CVD infiltration

The relative atomic ratios obtained by HAADF (Figure 2 in the main text) are listed in Table S1, where the zones 1, 2 and 3 correspond to the marked line in Figure 2c in the main text.

	1	2	3
Length (nm)	60	20	100
Si % atomic	95.9	95.7	61.2
C % atomic		1.4	20.8
O % atomic	4.1	2.9	18.0

Table S2. Relative atomic ratios of Si, C and O in **s0**.

Route 1: Generation of closed-surface porous Si structures

In structures **s1r**, sustained RIE etching of a structure **s0** led to a progressive change of the sample morphology and of the corresponding photonic response (Figure S1). RIE gradually

opened the shells of the upper layer spheres, as observed in the SEM images: the hexagonal array was well preserved even after 240 s RIE exposure, while the arrangement worsened for longer exposition times. The RIE process induced a clear change in the opal color (optical image), which reflects the structure modification. The reflectance spectra showed a clear reduction of the high-energy photonic features ($a/\lambda > 0.6$), and a well-defined Bragg peak (at $a/\lambda \approx 0.4$) was observed up to 90 s RIE exposure while degradation occurred at longer times.
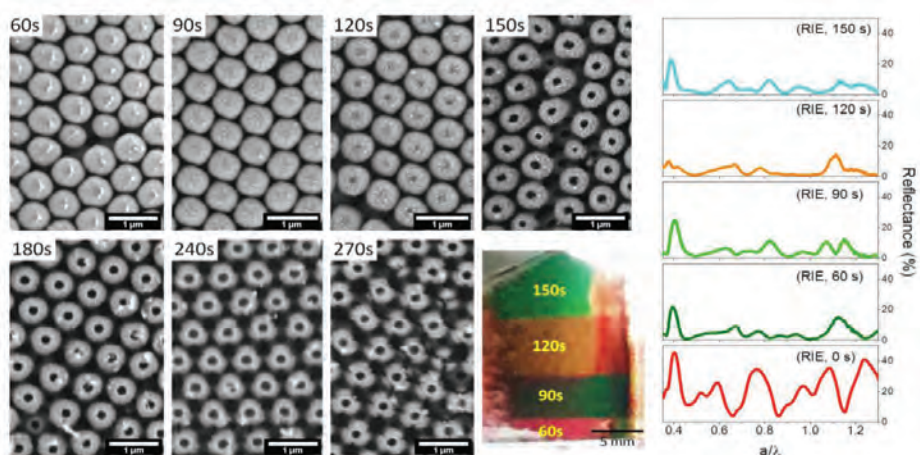

Figure S1. SEM and optical images (right) and optical reflectance spectra (left) of an **s0** sample (HCO template infiltrated at 490 Torr) after different RIE exposition times. SEM scale bars are 1 μm. Optical image scale bar 5 mm.

In the case of a heavily Si-infiltrated opal **s0**, RIE treatment allowed easy removal of the thick silicon layer formed during Si CVD, leading to manifest enhancement of the photonic response in the resulting **s1r** sample. As shown in Figure S2, the thick silicon cap (with thickness of roughly 400 nm) covering the opal top surface was progressively removed by RIE, accompanied by a significant improvement of the Bragg peak, with clear narrowing and intensity growth.
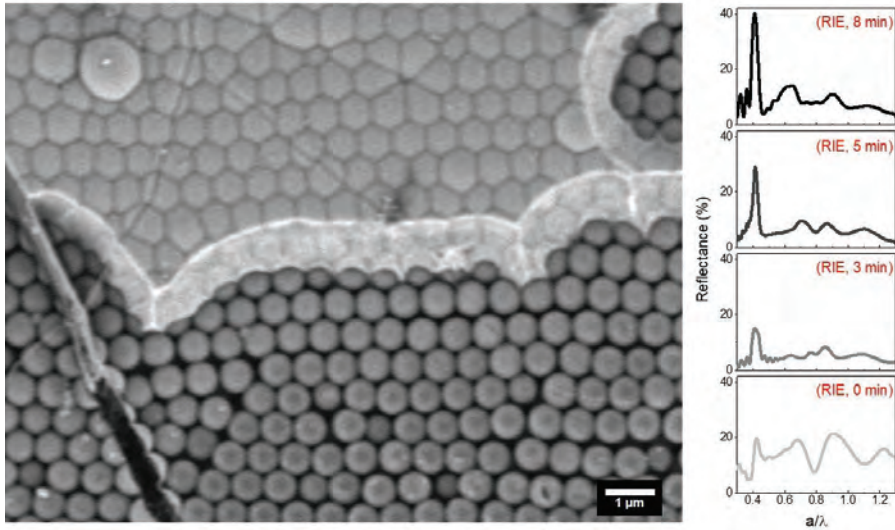
Figure S2. SEM image of an **s0** sample (HCO template infiltrated at 530 Torr) after 8 minutes of RIE exposure (left) and the corresponding optical reflectance spectra during the RIE process at different exposition times.

Silicon CVD conformally replicates the template underneath including unavoidable defects (vacancies, domain walls, dislocations, etc). Flower-like geometries, as the ones shown in Fig. S2, are just the result of one of those (vacancies) and can marginally affect the optical response of the sample. Besides, these exotic geometries are etched away after RIE.

In structures **s1rc**, calcination produced systematic shrinkage of the spheres in the upper opal layer with a closed shell, as explained in the main text. Figure S3 shows that, on the contrary, the bulk of the sample was not affected and the inverse opal structure was preserved.
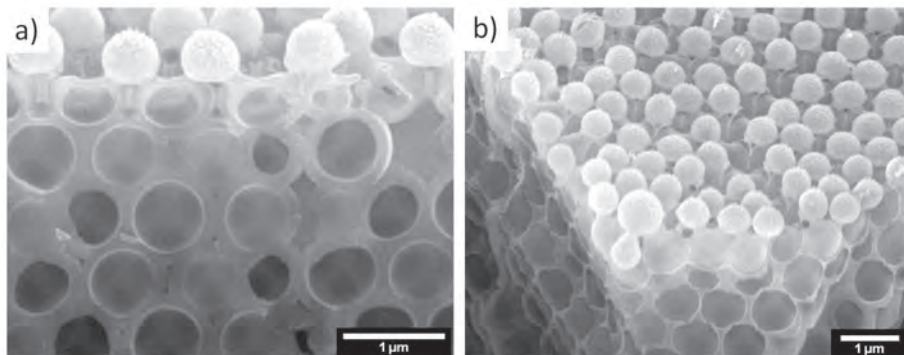

Figure S3. SEM images of an **s1rc** sample, cross-section (a) and top view (b). HCO template infiltrated at 110 Torr and RIE treated for 120 s.

The region of F1s and Si2p confirm the formation of SiO_xF_y and F-Si species, during the RIE treatment.
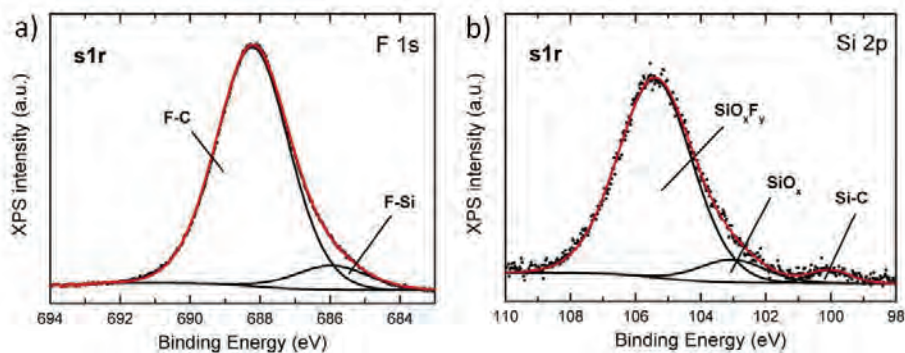
Figure S4. Deconvolution of F1s (a) and Si2p (b) XPS spectrum of **s1r** (RIE treatment of 120 s).

The relative atomic ratios obtained from the XPS analysis performed on **s1r** and **s1rc** (see spectra in Figure 4 –main text) are listed in Table S2.

STRUCTURE	C %	SI %	O %	F %
S1R	37	5	12	41
S1RC	7	29	60	0.5

Table S3. Relative atomic ratios of C, Si, O and F for **s1r** and for **s1rc**.

Route 2: Generation of open-surface porous Si structures

Figure S5 shows the HRTEM study on structures **s2c**, as analyzed by EDS mapping, demonstrating that inverse porous silicon structures were obtained after calcination. The presence of C was found to be negligible –as expected after calcination–. Three different regions were identified, all of them predominantly composed by Si. Oxygen was essentially located in the two outermost regions of the shell, while it strongly decreased in the inner part.
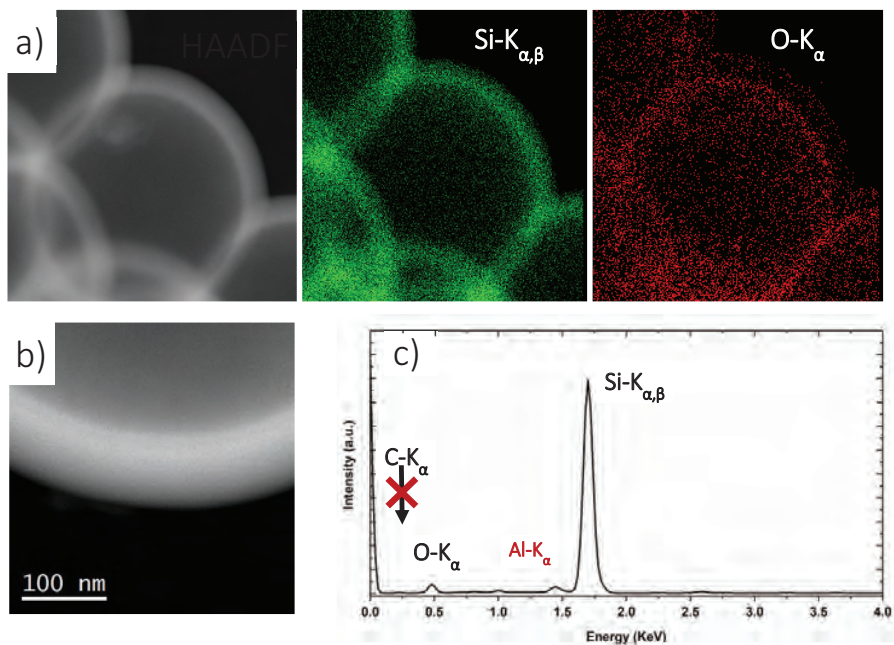
Figure S5. STEM and EDS characterization of structures **s2c.** (a) HAADF image (left) of a calcined **s₀** sphere, in which several rings with different contrast are observed. The colored EDS mapping reveals the presence of Si (green) and O (red). (b) A closer look in a higher magnification HAADF image reveals three discernible zones. c) No significant presence of C is found, as confirmed in the sum EDS spectrum acquired along the white line depicted in b. The hollow@carbon system (**s₀**) was infiltrated with Si at 110 Torr, while the calcination was performed as abovementioned in section S1.

[1] L. K. Gil-Herrera, Á. Blanco, B. H. Juárez, C. López, *Small* **2016**, *12*, 4357.

[2] L. K. Gil-Herrera, J. A. Pariente, F. Gallego-Gómez, F. Gándara, B. H. Juárez, Á. Blanco, C. López, *Adv. Funct. Mater.* **2018**, *28*, 1703885.

[3] J. Pereira, L. E. Pichon, R. Dussart, C. Cardinaud, C. Y. Duluard, E. H. Oubensaid, P. Lefaucheux, M. Boufnichel, P. Ranson, *Appl. Phys. Lett.* **2009**, *94*, 3.

4. Conclusiones y Perspectivas

La principal contribución de esta tesis fue demostrar la viabilidad y utilidad de los materiales carbonosos para la fabricación de estructuras ordenadas híbridas con aplicaciones en fotónica, específicamente en el rango visible e IR cercano.

La síntesis de esferas coloidales monodispersas carbonosas sin la adición de surfactantes o aditivos fue posible mediante la carbonización hidrotermal de la glucosa asistido por el PS. Esto permitió la construcción de un ópalo carbonoso con una respuesta óptica sintonizable en un amplio rango del espectro electromagnético. Tal esqueleto carbonoso dio lugar a variadas arquitecturas de silicio tanto hibridas como de silicio puro, las cuales fueron determinadas tanto por la presión del Si en el CVD como por el orden en los tratamientos aplicados. Dichos resultados son esquematizados en la figura 8.
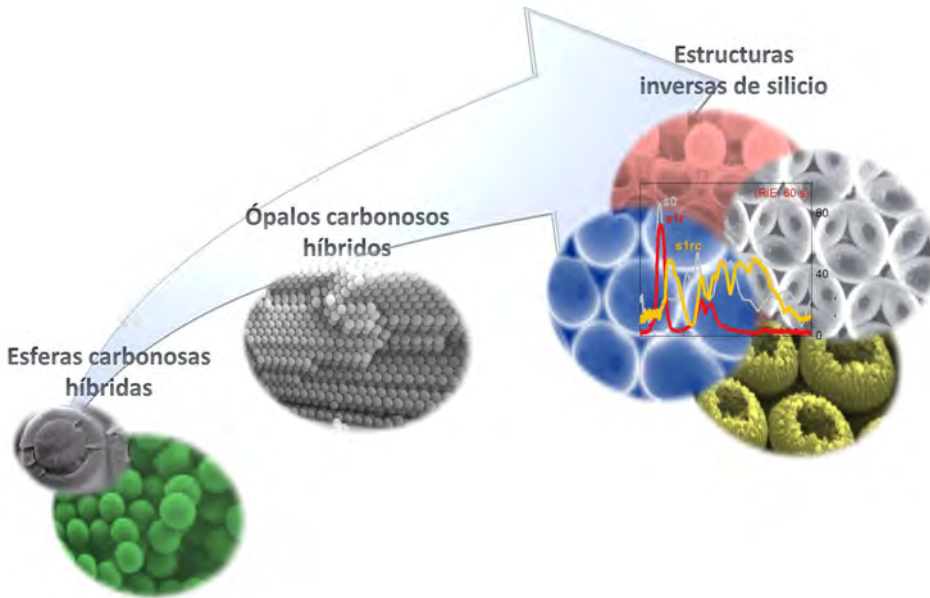
Figura 8. Esquema representativo de los resultados obtenidos.

Por otro lado, la fabricación de estructuras alternativas tales como estructuras con porosidad jerarquizada de carbono y/o silicio, así como también, estructuras basadas en silicio con una capa pasivante C-F, podrían ser interesantes como punto de partida de materiales en diferentes campos de la ciencia de materiales.

Igualmente, los resultados obtenidos en esta tesis abren nuevos caminos e inquietudes tanto en el entendimiento a nivel fundamental como aplicado. Así pues, sería necesario un estudio teórico acerca del comportamiento de la luz en estructuras tridimensionales, como las

carbonosas con porosidad jerarquizada o con estructuras hibridas complejas, tales como SiO_xC o F^-. Lo que es de gran utilidad a la hora de diseñar materiales con propiedades fotónicas en diferentes campos de investigación.

Por otro lado, las estructuras obtenidas podrían ser punto de partida para el desarrollo de materiales funcionales, en donde la sinergia de sus componentes potencie propiedades, tales como estructurales, morfológicas y/o ópticas.

Referencias

[1] Lee, D. W. (1991). Ultrastructural basis and function of iridescent blue colour of fruits inElaeocarpus. Nature, 349(6306), 260–262.

[2] Kinoshita, S., Yoshioka, S., & Kawagoe, K. (2002). Mechanisms of structural colour in the Morpho butterfly: Cooperation of regularity and irregularity in an iridescent scale. *Proceedings of the Royal Society B: Biological Sciences*, *269*(1499), 1417–1421.

[3] Vukusic, P., & Sambles, J. R. (2003). Photonic structures in biology. Nature, 424(6950), 852–855.

[4] Vignolini, S., Moyroud, E., Glover, B. J., & Steiner, U. (2013). Analyzing photonic structures in plants. *Journal of the Royal Society Interface*, *10*(87).

[5] Sanders, J. V. (1968). Diffraction of light by opals. *Acta Crystallographica Section A*, *24*(4), 427–434.

[6] Joannopoulos, J. D., Johnson, S. G., Winn, J. N., & Meade, R. D. (2011). *Photonic crystals: Molding the flow of light. Photonic Crystals: Molding the Flow of Light (Second Edition)*. Retrieved from http://ab-initio.mit.edu/book/

[7] Yablonovitch, E. (1987). Inhibited spontaneous emission in solid-state physics and electronics. *Physical Review Letters*, *58*(20), 2059–2062.

[8] Chen, H., Lou, R., Chen, Y., Chen, L., Lu, J., & Dong, Q. (2017). Photonic crystal materials and their application in biomedicine. *Drug Delivery*, *24*(1), 775–780.

[9] Kim, D. Y., Choi, S., Cho, H., & Sun, J.-Y. (2019). Electroactive Soft Photonic Devices for the Synesthetic Perception of Color and Sound. *Advanced Materials*, *31*(2), 1804080.

[10] Rajan, R., Babu, P. R., & Senthilnathan, K. (2018). The Dawn of Photonic Crystals: An Avenue for Optical Computing. In *Theoretical Foundations and Application of Photonic Crystals*. InTech.

[11] Cooperstein, I., Sachyani Keneth, E., Shukrun Farrell, E., Rosental, T., Wang, X., Kamyshny, A., & Magdassi, S. (2018). Hybrid Materials for Functional 3D Printing. *Advanced Materials Interfaces*, *5*(22).

[12] Miller, K. J., Haglund, R. F., & Weiss, S. M. (2018). Optical phase change materials in integrated silicon photonic devices: review. *Optical Materials Express*, *8*(8), 2415.

[13] John, S. (1987). Strong localization of photons in certain disordered dielectric superlattices. *Physical Review Letters*, *58*(23), 2486–2489.

[14] Blanco, Á. (2001). *Cristales fotónicos ópalo-semiconductor*. (tesis doctoral) Universidad Autónoma de Madrid.

[15] García-Santamaría, F., López, C., Meseguer, F., López-Tejeira, F., Sánchez-Dehesa, J., & Miyazaki, H. T. (2001). Opal-like photonic crystal with diamond lattice. Applied Physics Letters, 79(15), 2309–2311.

[16] Woodcock, L. V. (1997). Entropy difference between the face-centred cubic and hexagonal close- packed crystal structures. *Nature*, *385*(6612), 141–143.

[17] Tarhan, I., & Watson, G. (1996). Photonic band structure of fcc colloidal crystals. *Physical Review Letters*, *76*(2), 315–318.

[18] Stein, A., & Schroden, R. C. (2001). Colloidal crystal templating of three-dimensionally ordered macroporous solids: materials for photonics and beyond. Current Opinion in Solid State and Materials Science, 5(6), 553–564.

[19] Galisteo-López, J. F., Ibisate, M., Sapienza, R., Froufe-Pérez, L. S., Blanco Montes, Á., & López, C. (2011). Self-Assembled Photonic Structures. *Advanced Materials*, *23*(1), 30–69.

[20] Sözёr, H. S., Haus, J. W., & Inguva, R. (1992). Photonic bands: Convergence problems with the plane-wave method. *Physical Review B*, *45*(24), 13962–13972.

[21] Zakhidov, A. A., Baughman, R. H., Iqbal, Z., Cui, C., Khayrullin, I., Dantas, S. O., Ralchenko, V. G. (1998). Carbon structures with three-dimensional periodicity at optical wavelengths. *Science*, *282*(5390), 897–899.

[22] Norris, D. J., & Vlasov, Y. A. (2001). Chemical Approaches to Three-Dimensional Semiconductor Photonic Crystals. *Advanced Materials*, *13*(6), 371–376.

[23] Blanco, Á., Chomski, E., Grabtchak, S., Ibisate, M., John, S., Leonard, S. W., van Driel, H. M. (2000). Large-scale synthesis of a silicon photonic crystal with a complete three-dimensional bandgap near 1.5 micrometres. *Nature*, *405*(6785), 437–440.

[24] Lai, C.-F., & Wang, Y.-C. (2016). Colloidal Photonic Crystals Containing Silver Nanoparticles with Tunable Structural Colors. *Crystals*, *6*(5), 61.

[25] Goodman, M. D., Kim, S., Tatsuda, N., Yano, K., & Braun, P. V. (2015). Enhanced Secondary Battery Anodes Based on Si and Fe3O4

Nanoparticle Infilled Monodisperse Carbon Starburst Colloidal Crystals. *Particle and Particle Systems Characterization*, *32*(10), 928–933.

[26] Geng, C., Sun, H., Ma, L., Ling, C., Fu, M., He, D., & Wang, Y. (2019). 3D Hybrid Plasmonic Photonic Crystals by Colloidal Crystal Templating and Hydrogel Assisted Conformal Metal Etching. *Advanced Optical Materials*, 1900599.

[27] Titirici, M.-M., Thomas, A., & Antonietti, M. (2007). Replication and Coating of Silica Templates by Hydrothermal Carbonization. Advanced Functional Materials, 17(6), 1010–1018.

[28] White, R. J., Tauer, K., Antonietti, M., & Titirici, M.-M. M. (2010). Functional hollow carbon nanospheres by latex templating. Journal of the American Chemical Society, 132(49), 17360–17363.

[29] Nie, G., Lu, X., Lei, J., & Wang, C. (2015). Seed-assisted synthesis of hierarchical manganese dioxide/carbonaceous sphere composites with enhanced supercapacitor performance. Electrochimica Acta, 180, 1033–1040.

[30] Wang, C., Xu, T., & Wang, C. A. (2016). Microwave absorption properties of C/(C@CoFe) hierarchical core-shell spheres synthesized by using colloidal carbon spheres as templates. *Ceramics International*, *42*(7), 9178–9182.

[31] Kalijadis, A., DorCevidć, J., Trtić-Petrović, T., Vukčević, M., Popović, M., Maksimović, V, Laušević, Z. (2015). Preparation of boron-doped hydrothermal carbon from glucose for carbon paste electrode. *Carbon*, *95*, 42–50.

[32] Qi, X., Lian, Y., Yan, L., & Smith, R. L. (2014). One-step preparation of carbonaceous solid acid catalysts by hydrothermal

carbonization of glucose for cellulose hydrolysis. Catalysis Communications, 57, 50–54.

[33] Zhang, H., Hu, M., Lv, Q., Yang, L., & Lv, R. (2018). Monodisperse nitrogen-doped carbon spheres with superior rate capacities for lithium/sodium ion storage. *Electrochimica Acta*.

[34] Xu, F., Tang, Z., Huang, S., Chen, L., Liang, Y., Mai, W., Wu, D. (2015). Facile synthesis of ultrahigh-surface-area hollow carbon nanospheres for enhanced adsorption and energy storage. Nature Communications, 6, 1–10.

[35] Sevilla, M., & Fuertes, a. B. (2009). The production of carbon materials by hydrothermal carbonization of cellulose. Carbon, 47(9), 2281–2289.

[36] Falco, C., Baccile, N., & Titirici, M.-M. M. (2011). Morphological and structural differences between glucose, cellulose and lignocellulosic biomass derived hydrothermal carbons. *Green Chemistry*, *13*(11), 3273.

[37] Baccile, N., Laurent, G., Babonneau, F., Fayon, F., Titirici, M.-M. M., & Antonietti, M. (2009). Structural characterization of hydrothermal carbon spheres by advanced solid-state MAS 13C NMR investigations. Journal of Physical Chemistry C, 113, 9644–9654.

[38] Li, R., Wang, L., & Shahbazi, A. (2015). A Review of Hydrothermal Carbonization of Carbohydrates for Carbon Spheres Preparation. *Trends in Renewable Energy*, *1*(1), 43–56.

[39] Sun, X., & Li, Y. (2004). Colloidal Carbon Spheres and Their Core/Shell Structures with Noble-Metal Nanoparticles. Angew. Chem. Int. Ed., 43(5), 597–601.

[40] Li, S., Pasc, A., Fierro, V., & Celzard, A. (2016). Hollow carbon spheres, synthesis and applications – a review. J. Mater. Chem. A, 4(33), 12686–12713.

[41] Tian, H., Liang, J., & Liu, J. (2019). Nanoengineering Carbon Spheres as Nanoreactors for Sustainable Energy Applications. Advanced Materials, 1903886.

[42] Astratov, V. N., Bogomolov, V. N., Kaplyanskii, A. A., Prokofiev, A. V., Samoilovich, L. A., Samoilovich, S. M., & Vlasov, Y. A. (1995). Optical spectroscopy of opal matrices with CdS embedded in its pores: Quantum confinement and photonic band gap effects. *Il Nuovo Cimento D*, *17*(11–12), 1349–1354.

[43] Mayoral, R., Requena, J., Moya, J. S., López, C., Cintas, A., Míguez, H., Blanco, Á. (1997). 3D long-range ordering in an SiO2 submicrometer-sphere sintered superstructure. *Advanced Materials*, *9*(3), 257–260.

[44] Holgado, M., García-Santamaría, F., Blanco, A., Ibisate, M., Cintas, A., Míguez, H., López, C. (1999). Electrophoretic deposition to control artificial opal growth. *Langmuir*, *15*(14), 4701–4704.

[45] García-Santamaría, F., Miyazaki, H. T., Urquía, A., Ibisate, M., Belmonte, M., Shinya, N., López, C. (2002). Nanorobotic manipulation of microspheres for on-chip diamond architectures. Advanced Materials, 14(16), 1144–1147.

[46] Pursiainen, O. L. J., Baumberg, J. J., Winkler, H., Viel, B., Spahn, P., & Ruhl, T. (2008). Shear-induced organization in flexible polymer opals. Advanced Materials, 20(8), 1484–1487.

[47] Jiang, P., Bertone, J. F., Hwang, K. S., & Colvin, V. L. (1999). Single-crystal colloidal multilayers of controlled thickness. *Chemistry of Materials*, *11*(8), 2132–2140.

[48] Norris, D. J., Arlinghaus, E. G., Meng, L., Heiny, R., & Scriven, L. E. (2004). Opaline photonic crystals: How does self-assembly work? *Advanced Materials*, *16*(16).

[49] Blanco, Á., & López, C. (2006). Silicon Onion-Layer Nanostructures Arranged in Three Dimensions. *Advanced Materials*, *18*(12), 1593–1597.

[50] Míguez, H., Tetreault, N., Yang, S. M., Kitaev, V., & Ozin, G. a. (2003). A New Synthetic Approach to Silicon Colloidal Photonic Crystals with a Novel Topology and an. *Advanced Materials*, *15*(7–8), 597–600.

[51] Pereira, J., Pichon, L. E., Dussart, R., Cardinaud, C., Duluard, C. Y., Oubensaid, E. H., Ranson, P. (2009). In situ x-ray photoelectron spectroscopy analysis of SiOxF y passivation layer obtained in a SF6/O2 cryoetching process. *Applied Physics Letters*, *94*(7), 3–5.

[52] Bhagat, P. N., Patil, K. R., Bodas, D., & Paknikar, K. M. (2015). Hydrothermal synthesis and characterization of carbon nanospheres: a mechanistic insight. *RSC Adv.*, *5*(73), 59491–59494.

[53] Ryu, J., Suh, Y. W., Suh, D. J., & Ahn, D. J. (2010). Hydrothermal preparation of carbon microspheres from mono-saccharides and phenolic compounds. *Carbon*, *48*(7), 1990–1998.

[54] Titirici, M., Antonietti, M., & Baccile, N. (2008). Hydrothermal carbon from biomass: a comparison of the local structure from poly- to

monosaccharides and pentoses/hexoses. *Green Chemistry*, *10*(11), 1204.

[55] Li, S., Pasc, A., Fierro, V., & Celzard, A. (2016). Hollow carbon spheres, synthesis and applications – a review. *J. Mater. Chem. A*, *4*(33), 12686–12713.

[56] Goodman, M. D., Arpin, K. A., Mihi, A., Tatsuda, N., Yano, K., & Braun, P. V. (2013). Enabling New Classes of Templated Materials through Mesoporous Carbon Colloidal Crystals. Advanced Optical Materials, 1(4), 300–304.

[57] Yamada, Y., Ishii, M., Nakamura, T., & Yano, K. (2010). Artificial Black Opal Fabricated from Nanoporous Carbon Spheres. Langmuir, 26(12), 10044–10049.

[58] Lee, K. U., Kim, M. J. M., Park, K. J., Kim, M. J. M., & Kim, J. J. (2015). Mobility of black pigments for electrophoretic display depending on the characteristics of carbon sphere. *Dyes and Pigments*, *121*, 276–281.

[59] Baccile, N., Weber, J., Falco, C., & Titirici, M. (2013). Characterization of Hydrothermal Carbonization Materials. In Sustainable Carbon Materials from Hydrothermal Processes (pp. 151–211). Oxford, UK: John Wiley & Sons, Ltd.

[60] Perpall, M. W., Prasanna, K., Perera, U., DiMaio, J., Ballato, J., Foulger, S. H., & Smith, D. W. (2003). Novel network polymer for templated carbon photonic crystal structures. Langmuir, 19(18), 7153–7156.

[61] MIT Photonic-Bands, Software disponible en: http://ab-initio.mit.edu/mpb/. Desarrollado por: Ab Initio Physics Group, Massachussets Institute of Technology, dirigido por J.D. Joannopoulos.

[62] El programa de cálculo mpb se basa en una expansión del campo electromagnético en una base de ondas planas de tal modo que éste posea la periodicidad de la constante dieléctrica en el cristal fotónico.

[63] Meade, R. D., Rappe, A. M., Brommer, K. D., Joannopoulos, J. D., & Alerhand, O. L. (1993). Accurate theoretical analysis of photonic band-gap materials. *Physical Review B*, *48*(11), 8434–8437.

[64] Chen, X., Wang, L., Wen, Y., Zhang, Y., Wang, J., Song, Y., Zhu, D. (2008). Fabrication of closed-cell polyimide inverse opal photonic crystals with excellent mechanical properties and thermal stability. *Journal of Materials Chemistry*, *18*(19), 2262.

[65] García-Santamaría, F., Nelson, E. C., & Braun, P. V. (2007). Optical surface resonance may render photonic crystals ineffective. *Physical Review B*, *76*(7), 1–6.
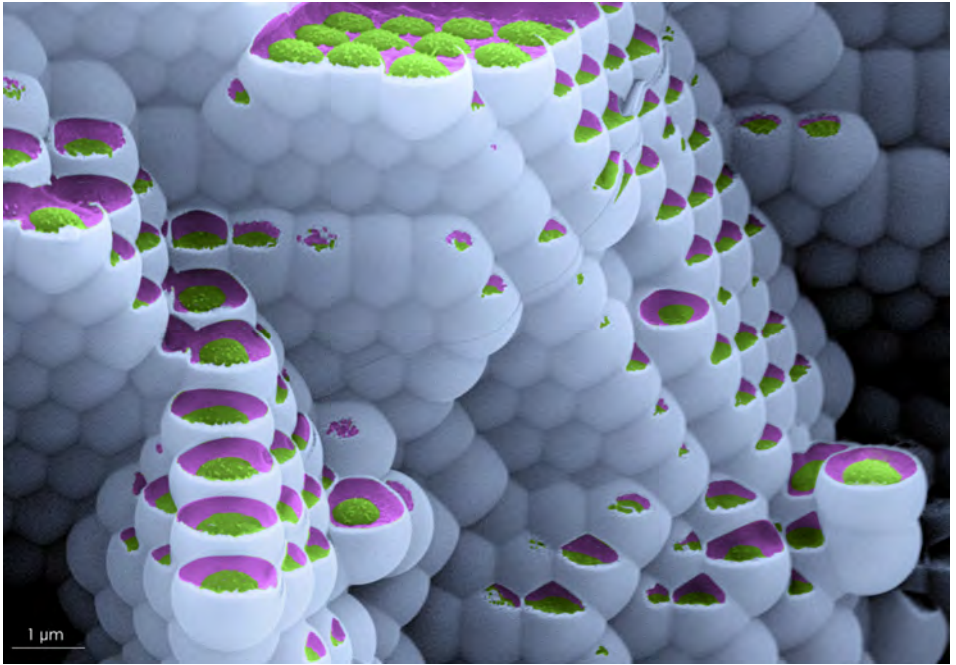
Ciudad Futurista

Fotciencia14 (2017)